Optical Characterization and Lasing Study of Nanowires

by

Zhicheng Liu

A Dissertation Presented in Partial Fulfillment
of the Requirements for the Degree
Doctor of Philosophy

Approved May 2015 by the
Graduate Supervisory Committee:

Cun-Zheng Ning, Chair
Joseph Palais
Hongbin Yu
Yu Yao

ARIZONA STATE UNIVERSITY

August 2015

ABSTRACT

Nanowires are one-dimensional (1D) structures with diameter on the nanometer scales with a high length-to-diameter aspect ratio. Nanowires of various materials including semiconductors, dielectrics and metals have been intensively researched in the past two decades for applications to electrical and optical devices. Typically, nanowires are synthesized using the vapor-liquid-solid (VLS) approach, which allows defect-free 1D growth despite the lattice mismatch between nanowires and substrates. Lattice mismatch issue is a serious problem in high-quality thin film growth of many semiconductors and non-semiconductors. Therefore, nanowires provide promising platforms for the applications requiring high crystal quality materials.

With the 1D geometry, nanowires are natural optical waveguides for light guiding and propagation. By introducing feedback mechanisms to nanowire waveguides, such as the cleaved end facets, the nanowires can work as ultra-small size lasers. Since the first demonstration of the room-temperature ultraviolet nanowire lasers in 2001, the nanowire lasers covering from ultraviolet to mid infrared wavelength ranges have been intensively studied. This dissertation focuses on the optical characterization and laser fabrication of two nanowire materials: erbium chloride silicate nanowires and composition-graded CdSSe semiconductor alloy nanowires.

Chapter 1 – 5 of this dissertation presents a comprehensive characterization of a newly developed erbium compound material, erbium chloride silicate (ECS) in a nanowire form. Extensive experiments demonstrated the high crystal quality and excellent optical properties of ECS nanowires. Optical gain higher than 30 dB/cm at 1.53 μm wavelength is demonstrated on single ECS nanowires, which is higher than the gain of any reported

erbium materials. An ultra-high Q photonic crystal micro-cavity is designed on a single ECS nanowire towards the ultra-compact lasers at communication wavelengths. Such ECS nanowire lasers show the potential applications of on-chip photonics integration.

Chapter 6 – 7 presents the design and demonstration of dynamical color-controllable lasers on a single CdSSe alloy nanowire. Through the defect-free VLS growth, engineering of the alloy composition in a single nanowire is achieved. The alloy composition of CdS_xSe_{1-x} uniformly varies along the nanowire axis from x=1 to x=0, giving the opportunity of multi-color lasing in a monolithic structure. By looping the wide-bandgap end of the alloy nanowire through nanoscale manipulation, the simultaneous two-color lasing at green and red colors are demonstrated. The 107 nm wavelength separation of the two lasing colors is much larger than the gain bandwidth of typical semiconductors. Since the two-color lasing shares the output port, the color of the total lasing output can be controlled dynamically between the two fundamental colors by changing the relative output power of two lasing colors. Such multi-color lasing and continuous color tuning in a wide spectral range would eventually enable color-by-design lasers to be used for lighting, display and many other applications.

ACKNOWLEDGEMENTS

TABLE OF CONTENTS

LIST OF TABLES

LIST OF FIGURES

LIST OF ACRONYMS

1D	One-dimensional
CIE	International Commission on Illumination
CUC	Cooperative Upconversion Coefficient
CVD	Chemical Vapor Deposition
CW	Continuous Wave
DFB	Distributed Feedback
ECS	Erbium Chloride Silicate
EDFA	Erbium-dope Fiber Amplifier
EDFL	Erbium-doped Fiber Laser
EDS	Energy Dispersive Spectroscopy
EL	Electroluminescent
ESA	Excited State Absorption
ETA	Energy Transfer Absorption
FDTD	Finite-difference Time-domain
FIB	Focused Ion Beam
GSA	Ground State Absorption
HR-TEM	High-resolution Transmission Electron Microscopy
JCPDS	Joint Committee on Powder Diffraction Standards
LED	Light Emitting Diodes
PhC	Photonic Crystal
PIC	Photonic Integrated Circuit
PL	Photoluminescence
PMT	Photomultiplier Tube

RGB	Red Green Blue
SEM	Scanning Electron Microscopy
SOI	Silicon-on-insulator
TEM	Transmission Electron Microscopy
VLS	Vapor-liquid-solid
WDM	Wavelength-division Multiplexing
XRD	X-ray Diffraction
YbCS	Triytterbium Chloroorthosilicate

CHAPTER 1

ERBIUM CHLORIDE SILICATE NANOWIRES

1.1 Introduction

Photonic integrated circuits (PICs) are becoming important due to the demand for high-speed, high-efficiency and low-cost optical networks. The exponential growth similar to "Moore's law" in microelectronics has been observed in PICs. Silicon is the most desired platform for PICs because of the low cost and mature processing techniques. The dense wavelength division multiplexed transmitters and receivers have been demonstrated on the large-scale silicon-based PICs, but the lack of on-chip and silicon-compatible optical amplifiers and lasers is the remaining obstacle.

Since the first demonstration of the erbium-doped fiber amplifier in 1987, erbium-doped materials have played many important roles in optical communications owing to the broadband amplification around the wavelength of 1.55 μm. However, the required fiber amplifiers are over a meter, due to limited erbium concentration levels of approximately 10^{20} cm^{-3}. Such long fibers are unsuited for PIC applications. In the past decade, crystalline erbium compounds with erbium concentration 100-times higher than the erbium-doped materials have been researched to achieve higher gain. However, realizing such high gain in the thin-film or bulk forms of erbium compounds has been fundamentally difficult due to the low crystal quality and short emission lifetime.

Chapter 1 to Chapter 5 focuses on the characterization of the crystalline and optical properties of a newly developed erbium compound material, erbium chloride silicate (ECS) in nanowire form, synthesized on silicon substrate via chemical vapor deposition approach.

Thorough experiments illustrate high quality single-crystal and long emission lifetime of the ECS nanowires. For assessing the optical gain in ECS nanowires, approaches to measuring the signal enhancement and absorption coefficient are developed. Optical gain higher than 30 dB/cm is demonstrated on a single ECS nanowire, the highest of any erbium materials ever reported. Such high-gain ECS nanowires are expected to have potential applications in silicon-compatible photonic integration as light sources or amplifiers.

Finally, the simulation and fabrication towards the ECS nanowire laser are discussed. The high-Q micro-cavities including DFB grating and 1D photonic crystal are designed on a single ECS nanowire. The refractive index of the ECS nanowire is first obtained by transmission spectroscopy on the fabricated photonic crystal structure. Simulation of the 1D photonic crystal micro-cavity shows the prospect of the ultra-compact lasers based on ECS nanowires.

1.2 Erbium Materials

Erbium (Er) materials, which can be in crystalline or non-crystalline forms containing the rare earth element Er, have played important roles in optic communication systems for the gain at the communication wavelengths around 1.5 – 1.6 μm. The most well-known application of Er materials is the erbium-dope fiber amplifier (EDFA) which was first demonstrated in 1987 [1]. Due to its many important properties such as broadband gain [2, 3], high speed response [4], low noise[4, 5], immunity to crosstalk [6], and compatibility to the fiber communication systems, EDFAs have been applied to a broad range of applications including optical amplifiers [1, 2], lasers [7, 8], sensors [9], quantum information [10], etc.

Similar to the evolution of the electrical integrated circuits, there is a trend to integrate the telecommunication systems on single chip for reducing the material costs, improving the power efficiency and shrinking down the device sizes [11]. Such integrated photonics require the on-chip amplifiers and lasers at the telecommunication wavelengths [11, 12]. However, the meters-long Er-doped fibers are not compatible with the on-chip integration. Therefore, a wide range of Er-materials were developed for the integration platform, as listed below, including the Er-doped glasses, Er-doped crystalline dielectrics, Er-doped semiconductors and Er-compound materials.

1. Erbium-doped glasses

    Er-doped glasses are the most commonly used Er-materials due to the easy fabrication, broad-band gain, high stability and compatibility to various substrates [12, 13]. The host materials are amorphous glasses including silicate [2, 13], phosphate [14, 15], soda-lime glasses [16], fluoride glasses[14], etc. The erbium-doped glasses can be fabricated by ion implantation [16], RF-sputtering [15, 17] and sol-gel method [18]. The Er concentration in Er-doped glasses is typically 1-10×10^{20} cm^{-3} (0.1-1 atomic percentage) with optical gain of 1-4 dB/cm [15, 19, 20].

2. Erbium-doped crystalline dielectrics

    The Er-atoms can be doped in the crystalline or polycrystalline dielectric hosts including $LiNbO_3$ [21, 22], KY_3F_{10} [23], $(Gd,Lu)_2O_3$ [24], Y_2O_3 [24] and YAG[25]. Er-doped crystalline dielectrics are thermal-stable with high peak emission cross-sections [12], which are good for laser applications. However, due to the crystalline environment of the Er ions, the gain bandwidth is narrow, limiting the applications

in broadband amplifiers and tunable lasers [12, 24]. The synthesis methods includes Czochralski pulling [23], Er-diffusion [21] and pulsed laser deposition [24].

3. Erbium-doped semiconductors

The Er-doped semiconductors including Er-doped GaN [26], ZnO [27], InP [28], CdS [28] and Si [29] are developed for the optoelectronic devices. Especially the Er-dope silicon allows the integration with silicon photonics. The light emitting diodes based on Er-doped silicon have been demonstrated [30]. The major issue of the Er-dope semiconductors is the limitation of the doping density [12].

4. Erbium compounds

Er compounds have come into focus in the last decade for the high-gain amplifiers and ultra-compact lasers and amplifiers in telecommunication. The Er compounds are the single-crystalline or polycrystalline compounds with Er-concentration higher than 10^{22} cm^{-3}, including erbium oxide (Er_2O_3) [31, 32], erbium silicates (Er_2SiO_5, $Er_2Si_2O_7$) [33, 34] and erbium yttrium/ytterbium silicate alloy (EYS, EYbS) [35-37]. Due to the high Er-concentration, the potential gain of the Er compounds can be as high as 30 dB/cm [31], much higher than the demonstrated gain in Er-doped materials. The Er-compounds are typically prepare through RF magnetron sputtering [32, 33]. Since the lattice match of the Er_2O_3 and silicon, the molecule beam epitaxial growth of the Er_2O_3 thin film on Si(100) was reported [38].

1.3 Erbium Chloride Silicate Nanowires

Due to the development for the integrated photonic circuits, the demand on high-gain Er materials for miniature amplifiers and lasers at telecommunication wavelengths are

raised. The optical gain of the Er-doped materials is theoretically limited in the single digit dB per centimeter due to the limitation of the Er-concentration in the order of 10^{20} cm^{-3} (<1 atomic %) [15, 19, 20]. Although the doping density can be higher, the concentration quenching effect caused by the erbium clustering will significantly reduce the lifetime as well as the Er population at the excited state, thus making the gain impossible. The crystalline Er compounds are the potentially high-gain materials attributed to the Er concentration over 10^{22} cm^{-3}. The uniform distribution of the Er ions in the crystalline compounds reduces the possibility of the Er clusters, which is the main cause of the quenching effect. Thus, the gain performance of the Er compounds should be better than the Er-doped materials. However, the crystalline quality of the Er-compound thin-film is relatively low due to the RF sputtering synthesis. The defects and other imperfections of the crystal structure enhance the possibility of the concentration quenching [12]. Therefore, the net optical gain has not been demonstrated in the Er compounds with Er-concentration over 10^{22} cm^{-3}.

In 2011, a new form of Er-compound material, erbium chloride silicate (ECS) nanowire was synthesized using chemical vapor deposition (CVD) method by Ning's group in Arizona State University [39, 40]. The ECS nanowire is single-crystalline Er material with Er-concentration of 1.62×10^{22} cm^{-3}. Similar to the high Er-concentration Er compounds, the potentially high gain in ECS nanowire can be expected. Compared to the sputtered Er compounds, the ECS nanowires have much higher crystal quality attributed to the CVD growth, significantly restraining the concentration quenching effect. Therefore, the ultra-high optical gain in ECS nanowire is promising.

In Chapter 1 – 5 of this dissertation, the comprehensive crystalline and optical characterizations of the ECS nanowires are researched. Via X-ray diffraction analysis, energy dispersion spectroscopy and transmission electron microscopy, the chemical formula, atomic structure and Er ion distribution of ECS nanowires are studied. The high-quality single crystal is demonstrated. The detail optical spectroscopy of the ECS nanowires shows the strong emission at 1.53 μm with lifetime over 0.5 ms, which is close to the lifetime in the low Er-concentration materials, demonstrating the less concentration quenching effect in ECS nanowires. Owing to the high erbium density and high crystal quality, over 30 dB/cm net gain is demonstrated in single ECS nanowire, which is the highest of the ever demonstrated gain in Er materials. Such high gain in ECS nanowire enables great potential of the applications in the ultra-compact devices for the integrated photonic circuits. In the last chapter, the design and fabrication towards the ECS nanowire laser is presented. The ECS nanowires are believed to be the promising laser sources for the silicon compatible photonics.

1.4 Energy Levels of Erbium Ions

When the erbium atoms are incorporated in dielectric materials, one electron of the 4f shell and two electrons at the 6s shell are removed from the Er atom, forming Er^{3+} ions. The electron configuration of Er^{3+} ions is $[Xe]4f^{11}5s^{2}5p^{6}6s^{0}$, where [Xe] is the electron configuration of xenon. The energy levels of 4f shell in the Er^{3+} ions are plotted in Figure 1.1. The energy levels of Er^{3+} ions are irrelevant to the host materials that the Er^{3+} ions are incorporated in. The energy levels are labels in the form of $^{2S+1}L_{J}$, where S, L and J are the spin quantum number, orbit quantum number and total angular momentum quantum

number respectively. L=0, 1, 2, 3, 4... correspond to the letters S, P, D, F, G.... Unlike the semiconductors such as GaAs, ZnO, which have the broadband emission and absorption band, the emitting and absorbing transitions in Er^{3+} ions can only occur between the energy levels in the 4f shell, which corresponds to different discrete wavelengths. The most important 4f→4f transition is between the ground state $^4I_{15/2}$ and the first excited state $^4I_{13/2}$, giving the emission at 1.53 μm which is the wavelength important for optical communication. The first excited state $^4I_{13/2}$ is a metastable level with a lifetime much longer than the other higher energy levels, enabling the population inversion between the ground state $^4I_{15/2}$ and the first excited state $^4I_{13/2}$. Thus, optical gain at 1.53 μm can in principle be achieved in Er materials.
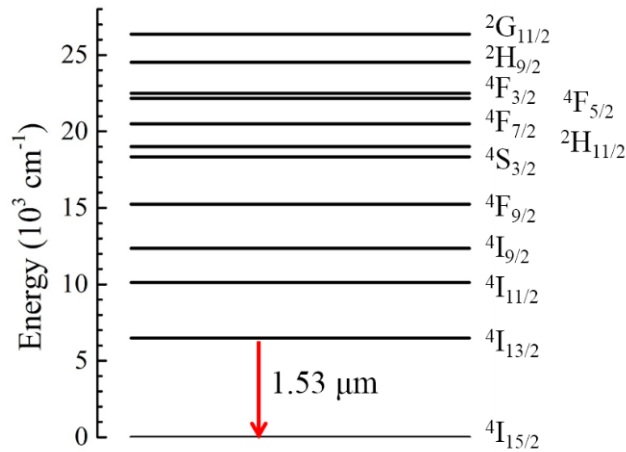
Figure 1.1 Energy level diagram of the Er^{3+} ions. The radiative transistion from $^4I_{13/2}$ to $^4I_{15/2}$ gives the emission at 1.53 μm.

To understand the transition dynamics and the gain model, a simplified 2-level model including the ground state $^4I_{15/2}$ and the metastable state $^4I_{13/2}$ is analyzed, as shown

in Figure 1.2. For gain applications, the Er materials are optically pumped at a wavelength matching with the transition between the ground state $^4I_{15/2}$ and an excited state, for the amplification of the probe signal at 1.53 μm. Because the lifetime of the higher excited states is very short, any Er ion at the higher states will immediately decay to the metastable state. The pumping rate is assumed to be $R_p = \phi_p \sigma_p$, where ϕ_p is the pumping flux and σ_p is the absorption cross section at the pumping wavelength. The concentration of Er ions at ground state and metastable state are N_1 and N_2 respectively. The total Er concentration is $N = N_1 + N_2$. There are several transitions between these two levels: radiative spontaneous transition (decay rate W_{21}^R) and nonradiative spontaneous transition (decay rate W_{21}^{NR}), stimulated absorption (decay rate A_{12}) and stimulated emission (decay rate A_{21}). The spontaneous emission lifetime of the metastable state can be written as $\tau = (W_{21}^{NR} + W_{21}^R)^{-1}$. In most cases, the radiative decay is dominant ($W_{21}^R \gg W_{21}^{NR}$) [41]. The stimulated absorption and emission rate are $A_{12} = \phi_s \sigma_{abs}$ and $A_{21} = \phi_s \sigma_{em}$ respectively, where ϕ_s is the photon flux of the amplified signal, σ_{abs} and σ_{em} are absorption and emission cross section between the ground state and metastable state respectively. Now the rate equations of this 2-level model can be written as

$$\frac{dN_1}{dt} = -R_p N_1 + \frac{N_2}{\tau} + A_{21} N_2 - A_{12} N_1 \qquad (1.1)$$

$$\frac{dN_2}{dt} = R_p N_1 - \frac{N_2}{\tau} - A_{21} N_2 + A_{12} N_1 \qquad (1.2)$$

In the equilibrium condition, the time differential terms are zero. The population at two states can be derived as

$$N_1 = \frac{\frac{1}{\tau} + \phi_s \sigma_{em}}{\phi_p \sigma_p + \frac{1}{\tau} + \phi_s(\sigma_{abs} + \sigma_{em})} N \tag{1.3}$$

$$N_2 = \frac{\phi_p \sigma_p + \phi_s \sigma_{abs}}{\phi_p \sigma_p + \frac{1}{\tau} + \phi_s(\sigma_{abs} + \sigma_{em})} N \tag{1.4}$$

The optical gain is the amplification of the probe signal, which is

$$g(z) = \frac{1}{\phi_s(z)} \cdot \frac{d\phi_s(z)}{dz} = \sigma_{em} N_2 - \sigma_{abs} N_1 \tag{1.5}$$

Without the pumping, the population at excited state N_2 is zero. The gain is negative which means the Er material is absorptive to the probe signal at 1.53 μm. While increasing the pumping, the population N_2 increases and the population N_1 drops. Population inversion occurs when $N_2/N_1 > \sigma_{abs}/\sigma_{em}$ and this is where optical gain is achieved. At this condition, the signal at 1.53 μm can be amplified by the Er material, enabling various applications such as optical amplifiers and lasers.
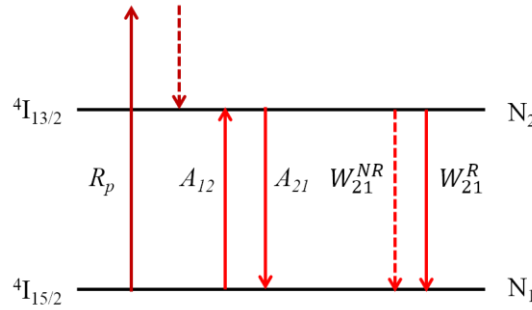
Figure 1.2 Energy level diagram and the transitions in 2-level model system. R_p is the pumping rate. A_{12} and A_{21} are the stimulated absorption and emission rates respectively. W_{21}^R and W_{21}^{NR} are the radiative and non-radiative spontaneous transition rates respectively.

1.5 Upconversion in Erbium Materials

The 2-level model is the ideal analysis of the excitation and signal amplification in Er materials. In reality, because the lifetimes of the higher excited levels are not zero, more energy levels should be involved into the system. The non-zero population of the higher excited states can exhibit emission at wavelengths shorter than 1.53 μm. For example, under 980 nm pumping, the dynamics of Er ions should be studied by a 3-level model including $^4I_{15/2}$, $^4I_{13/2}$, $^4I_{11/2}$ states, giving emissions at 980 nm and 1.53 μm.

As described by the atomic energy system, the Er ions can be excited from the excited states to higher states, resulting in emission at even shorter wavelengths than pumping light. This kind of transition is called upconversion. There are two mechanisms of the upconversion in Er materials: excited state absorption and cooperative upconversion.

1.5.1 Excited State Absorption

According to the discussion in Chapter 1.4, the pumping light can be absorbed by the Er ions when the wavelength matches the transition energy between the 4f levels. If the ions are excited from the ground state, the absorption is called as ground state absorption (GSA), as shown in the left part in Figure 1.3. The absorption wavelengths from the ground state to the first and higher excited states for Er ions are 1480 nm, 980 nm, 800 nm, 667 nm, 532 nm respectively. Absorption can also occur at excited states if there is a population of carriers at the excited states, which is called excited state absorption (ESA). The ions at the first excited states $^4I_{13/2}$ can be excited to $^4I_{9/2}$, $^2H_{11/2}$, $^2F_{5/2}$ and $^2H_{9/2}$ by the pumping with wavelengths at 1480 nm, 800 nm, 655 nm, 532 nm respectively, as shown in the right part in Figure 1.3. The absorption rate of ESA is $\phi_p \sigma_{ESA} N_2$, where ϕ_p is the pumping flux,

10

σ_{ESA} is the absorption cross section of ESA, and N_2 is the population at the excited state where absorption started. It is reported that in the Er-doped silicate glasses, the absorption cross section of ESA is 0.5 – 0.95 times of the absorption cross section of GSA [42].
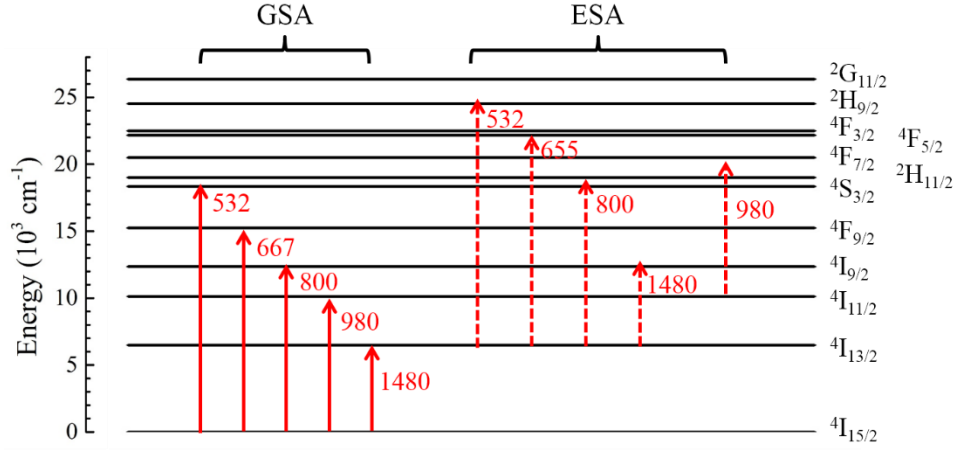
Figure 1.3 Energy level diagram showing the ground state absorption (GSA) and excited state absorption (ESA).

In order to achieve the amplification in the Er materials, we expect more population to be pumped to the metastable state $^4I_{13/2}$, enabling the population inversion. However, as shown in Figure 1.3, the ESA at 1480 nm, 800 nm and 655 nm can excites the Er ions from the $^4I_{13/2}$ to higher states, which will significantly reduce the population at $^4I_{13/2}$. Therefore, ESA negatively effects pumping at those pumping wavelengths. However, the 980 nm pumping is special, because there is no transition from $^4I_{13/2}$ matching with the 980 nm pumping. The ESA of 980 nm excitation only occurs between the states $^4I_{11/2}$ and $^4F_{7/2}$. Because of the short lifetime at $^4I_{11/2}$ state, the population at $^4I_{11/2}$ is typically negligible comparing to the population at $^4I_{13/2}$. Therefore, the ESA of 980 nm pumping will not significantly deteriorate the population inversion. This is the reason that the Er lasers and

11

amplifiers prefer to use 980 nm lasers as pumping sources. In the following experiments about the demonstration of the net gain in Chapter 4.2 – 4.4, we also use a 980 nm laser as the pumping source.

1.5.2 Cooperative Upconversion

Excited state absorption is the interaction between the pumping photon and one Er ion. The upconversion can also occur between the Er ions. As the Er concentration increases, the reduced average distance between the Er ions raises the possibility of the energy transferring from one Er ion to another Er ion. There are several kinds of energy transfer between Er ions, including resonant energy transfer, sensitized fluorescence, cross-relaxation, phonon-assisted non-radiative transfer and cooperative frequency upconversion [41, 43, 44]. The most important energy transfer is the cooperative upconversion which is also called energy transfer absorption (ETA). The energy transfer diagram of cooperative upconversion is shown in Figure 1.4. Both donor and acceptor Er ions are at the first excited state $^4I_{13/2}$ at the beginning. Through the cooperative upconversion, the donor ion transfers its energy to the acceptor ion, then decays to the ground state. The acceptor ion is then excited to the higher state $^4I_{9/2}$. Since cooperative upconversion involves two ions, the transition rate has a quadratic dependence on the population at the metastable state, written as $W_{CUC}N_2^2$. W_{CUC} is the cooperative upconversion efficiency (CUC). Cooperative upconversion can be neglected in the low Er concentration materials. However, the upconversion becomes significant when the Er concentration is higher than 10^{20} cm^{-3}, significantly reducing the lifetime of the Er ions. This effect contributes significantly as

12

the concentration quenching. The detailed analysis of the cooperative upconversion and concentration quenching will be discussed in Chapter 3.5 and 4.4.
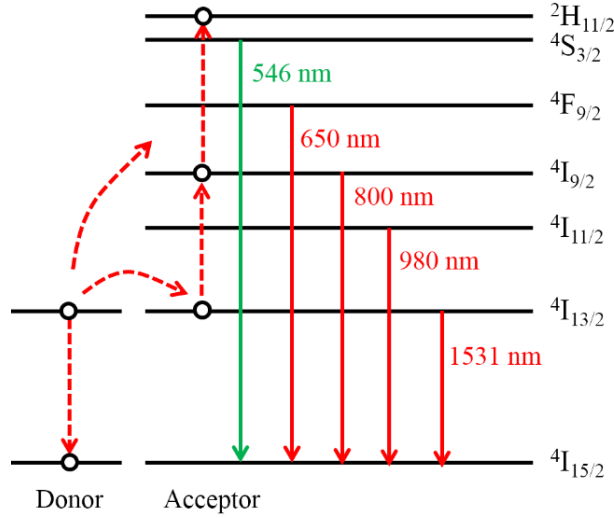
Figure 1.4 Energy diagram showing the first-order and second-order cooperative upconversion and the corresponding emissions.

Secondary cooperative upconversion can also occur between the donor ion at metastable state $^4I_{13/2}$ and the acceptor ion already excited to $^4I_{9/2}$ state through the initial cooperative upconversion. The relaxation of the excited ions gives the emission at 546 nm (green color) and the following wavelengths, as shown in Figure 1.4. Because the $^2H_{11/2}$ state is a relatively stable state, the population inversion can be achieved at this state by a strong upconversion. Green upconversion lasers with pumping at near infrared wavelengths were demonstrated in several erbium materials [45, 46].

CHAPTER 2

CRYSTALLINE CHARACTERIZATION OF ECS NANOWIRES

Nanowires refer to the one-dimensional (1D) nanostructure with a nanometer-scale diameter and high length-to-diameter aspect ratio. Nanowires based on various materials have been reported, including metals (Ag [47], Au [48]…), semiconductors (ZnO [49], GaN [50], CdS [51], Si [52]…) and dielectric materials (SiO_2 [53], polymers [54]…). Nanowires have a wide range of applications in optical and electronic devices, chemistry, biology and many other fields, including field-effect transistors [55], lasers [56, 57], photo-detectors [58], bio- and chemical- sensors [59, 60], solar cells [61] etc.

The common synthesis technique of nanowires is the chemical vapor deposition (CVD) approach which is based on the vapor-liquid-solid (VLS) mechanism [62]. The CVD growth is assisted by metal nanoparticles as the catalyst. The reacted source materials from the carrier gas (vapor) are absorbed by the melt metal nanoparticles, forming the catalyst alloy (liquid). The crystal nucleation (solid) occurs when the catalyst is supersaturated. 1D crystal grown begins at the interface of the catalyst and the substrate to achieve the minimum free energy of the system. Because the material participates in three phases: vapor, liquid and solid, it is called VLS mechanism. The nanowires grown through VLS mechanism are typically single crystal with low defect density due to the 1D growth behavior. Therefore, the CVD approach provides the opportunity to synthesize high-quality and single-crystal Er compound nanowires which potentially have high optical gain.

In this chapter, the growth of the ECS nanowires and a thorough analysis of the crystalline structure are studied. The detail growth procedures are presented in Chapter 2.1.

14

The chemical component and the crystal structure is determined by X-ray diffraction (XRD) in Chapter 2.2. The high-resolution transmission electron microscopy (TEM) analysis in Chapter 2.3 demonstrate that the ECS nanowires are high-quality single crystal. The growth direction of the ECS nanowire is determined. In Chapter 2.4, the growth and characterization of core/shell ECS nanowires with single-crystal silicon in core region and ECS in shell region are illustrated. Such core/shell nanowires are believed to have potentials in the electrically driven devices.

2.1 Growth of ECS Nanowires

The CVD approach of the ECS nanowire growth is illustrated in Figure 2.1(a). The growth is in a closed quartz tube mounted in a tube furnace. 30 mg silicon powder (Alfa Aesar, 99.99%) and 120 mg anhydrous erbium chloride ($ErCl_3$) micro beads (Alfa Aesar, 99.99%) are placed at the middle position of the furnace and the downstream edge of the furnace respectively. The silicon substrate coated with 12 nm Au film as the catalyst is vertically mounted on a quartz holder and placed next to the $ErCl_3$ source. The quartz tube is first evacuated for 20 minutes and then purged with 5 sccm Argon gas (5% H_2) as the carrier gas. The pressure in the tube chamber is controlled at 5 torr. The furnace temperature is then increased to 1150 °C with speed of 40 °C/minute. Due to the temperature gradient at the edge of the furnace, the temperature at the substrate is slightly lower than the temperature at the center of the furnace, which is 1050 °C. The furnace temperature is kept at 1150 °C for 3 hour growth, and then naturally cooled down to the room temperature.

Figure 2.1 Diagram of the chemical vapor deposition growth.

The as-grown nanowire sample is white color, as shown in Figure 2.2(a). The scanning electron microscopy (SEM) image of the as-grown nanowire (Figure 2.2(b)) shows high density nanowires with random orientation. According to the energy dispersive spectroscopy (EDS) analysis in Figure 2.2(c), the nanowire contains the elements of erbium, silicon, chlorine and oxygen. The erbium, chlorine and silicon are from the sources of silicon powder and erbium chloride. However, the source of the oxygen is not clear. It is supposed that the oxygen are from the oxidation layer on the silicon substrate and the sublimation from the quartz tube.

16
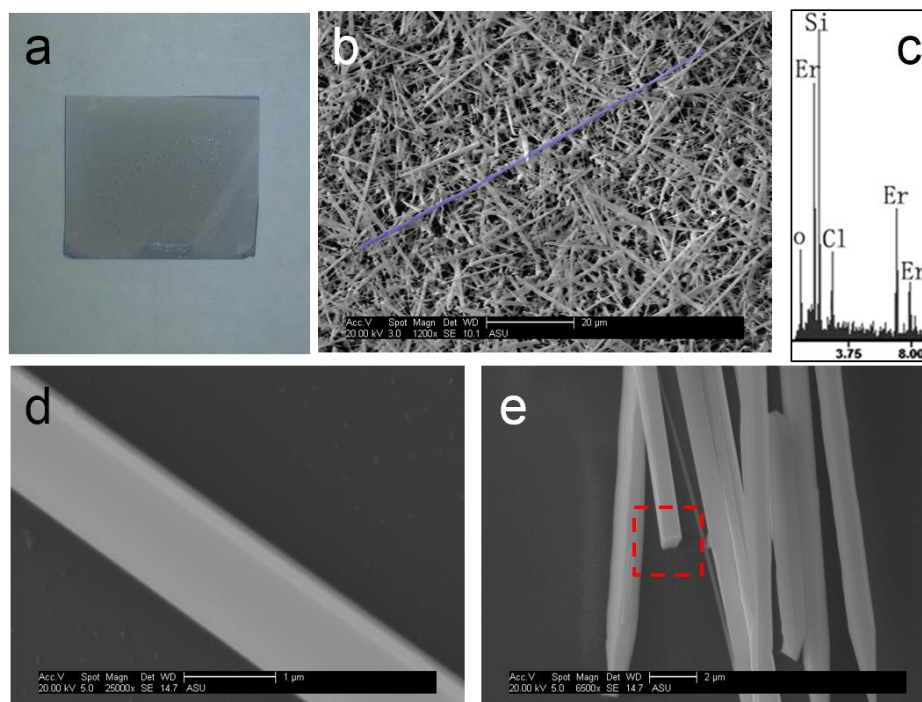
Figure 2.2 (a) Camera image of the as-grown ECS sample. (b) SEM image of the as-grown ECS sample. A 90 μm-long nanowire is labeled with blue color. The scale bar is 20 μm (c) EDS of the as-grown ECS sample. (d) A dispersed ECS nanowire with the diameter of 1 μm. (e) SEM image of the dispersed nanowires. The red box indicates the cross section of the ECS nanowire is rectangular shape.

The length of the nanowires can be controlled by the growth time. However, the length will not significantly increase when the growth time is over 2.5 hrs. It is possible to that the long nanowire falls down and breaks when it becomes long, limiting the maximum growth length. The maximum length of the nanowires is around 100 μm. In Figure 2.2(b), one nanowire with 90 μm in length is marked by the blue color.

The diameter of the nanowire is determined by the size of the Au catalyst. Since the Au particles were formed from the sputtered Au film during the heating process, the size of the Au nanoparticles can be mostly controlled by the thickness of the Au film while some size distribution exists. From the SEM image of the as-grown nanowires, more than 50% of the nanowires have the diameter between 700 nm and 1 μm, while the thin nanowires with diameter around 100 nm also exist. Since we focus on the applications of the nanowires as the optical waveguides, the large-diameter nanowires are preferred because they can support the propagation mode at 1.53 μm. Figure 2.2(d) presents a nanowire with diameter of 1 μm.

Figure 2.2(d) illustrates that the cross section of the nanowire is rectangular shape, not the hexagonal or circular shape like the typical nanowires [47-51]. For single-crystal nanowires, the cross-section shape is related to the crystalline structure. Chapter 2.2 and 2.3 will show that these nanowires are orthorhombic crystal and the crystal plane

17

perpendicular to the growth direction is close to a square shape. This is the reason why the cross section of the nanowire is rectangular.

2.2 X-ray Diffraction and Crystalline Structure Analysis

X-ray diffraction (XRD) is a powerful technique to identify the chemical component and crystal structure of an unknown crystalline material. Each crystal structure with different crystal symmetry, elements, and atom positions will give a specific XRD pattern. Thus, the chemical formula of the nanowires can be determined by matching the observed pattern with the XRD database. Figure 2.3 shows the XRD pattern on the as-grown nanowires. Because the nanowires are grown in random orientations, the XRD measurement was performed in powder diffraction mode. The XRD pattern of the nanowires perfectly matches with the JCPDS (Joint Committee on Powder Diffraction Standards) card 00-042-0365 published by International Centre for Diffraction Data (ICDD) [63], shown as the red crosses in Figure 2.3. Thus, the material of the nanowire is determined as erbium chloride silicate, abbreviated as ECS, with chemical formula: $Er_3(SiO_4)_2Cl$. The clearly separated XRD lines with very narrow linewidth demonstrate the high crystal quality of the ECS nanowires.
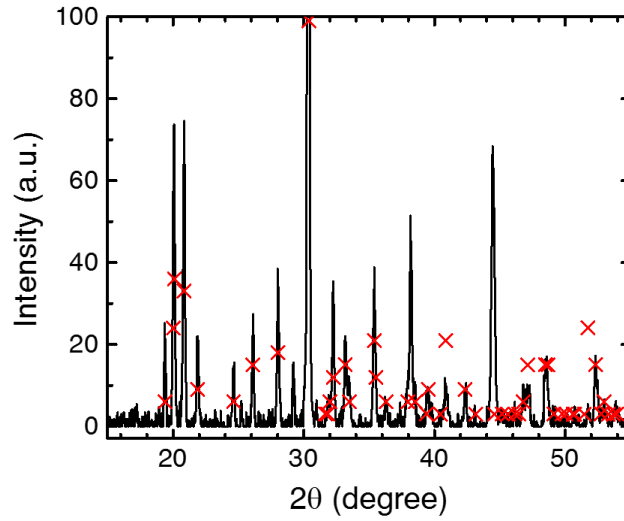
Figure 2.3 XRD of the ECS nanowires (black curve) and the XRD data from the JCPDS card 00-042-0365 (red crosses).

According to the JCPDS card, the ECS crystal is an orthorhombic crystal system, with different lattice constant in all three directions. The crystallographic parameters of ECS crystal are listed in Table 2.1. The Er concentration in ECS is 1.62×10^{22} cm^{-3}, at least two orders of magnitude higher than the typical Er-doped materials [15, 16, 64-67]. Such high Er-concentration is similar to other Er-compounds such as erbium silicate (2.03×10^{22} cm^{-3}) and erbium oxide (2.72×10^{22} cm^{-3}) [38, 68].

Table 2.1 List of the crystalline parameters.

Chemical formula	Er3 (SiO4)2Cl
Crystal system	Orthorhombic
Space group	Pnma, 62
a (Å)	6.8218
b (Å)	17.6519
c (Å)	6.1601
Alpha (°)	90
Beta (°)	90
Gamma (°)	90
Volume (10^{-3} nm^3)	741.79
Z	4
Er concentration	1.62×10^{22} cm^{-3}

Table 2.2 lists the positions of all atoms in a unit cell of an ECS crystal. The relative atom positions are obtained from $Yb_3(SiO_4)_2Cl$ (Triytterbium Chloroorthosilicate, YbCS), a rare-earth chloride silicate with the same crystal structure as ECS [2-2-1][69]. The lattice constants of ECS and YbCS have less than 1% difference, and the XRD of the two materials are very similar. As a result we can assume the relative atom positions of ECS and YbCS are the same. The exact atom positions of ECS crystal are calculated by the relative atom positions and the lattice constants, as shown in Table 2.2(b). According the atom positions and symmetry of the ECS crystal, the plot of the ECS crystal in a unit cell (Figure 2.4) is created by Mercury, a free software developed by Cambridge Crystallographic Data Centre [70]. The Si, Er, O and Cl atoms are plotted as the white, purple, red and green balls, respectively, and the bonds between the atoms are shown as the sticks. The view of this plot is in xy-plane with lattice constant a and b. In this view, the "heavy atoms" such as Er, Si, Cl are stacked in 6 layers vertical to the b (or y) direction.

These atom layers can be called as (060) planes, where the direction perpendicular to these planes is in the [060] direction. The average distance between the (060) planes is 0.29 nm.

Table 2.2 (a) List of the relative atom positions of ECS crystal. (b) List of the absolute atom positions of the ECS crystal.

(a)

	Set	x	y	z
Er	8	0.0130(1)	0.0903(1)	0.1276(2)
Er	4	0.2902(1)	0.25	0.8849(2)
Si	8	0.0232(7)	0.0996(3)	0.6213(12)
Cl	4	0.0367(10)	0.25	0.2357(11)
O	8	0.0089(17)	0.0319(6)	0.7935(18)
O	8	0.1915(17)	0.0966(7)	0.4470(19)
O	8	0.3284(17)	0.1187(7)	0.0282(20)
O	8	0.0356(18)	0.1750(6)	0.7717(20)

(b)

	Set	x (Å)	y (Å)	z (Å)
Er	8	0.0887(52)	1.5941(43)	0.7861(52)
Er	4	1.9797(55)	4.4129(75)	5.4511(96)
Si	8	0.1587(43)	1.7586(59)	3.8273(44)
Cl	4	0.2504(28)	4.4129(75)	1.4520(03)
O	8	0.0608(3)	0.5641(55)	4.8881(5)
O	8	1.3064(91)	1.7064(09)	2.7536(82)
O	8	2.2403(95)	2.0965(16)	0.1738(38)
O	8	0.2429(79)	3.0901(42)	4.7538(72)
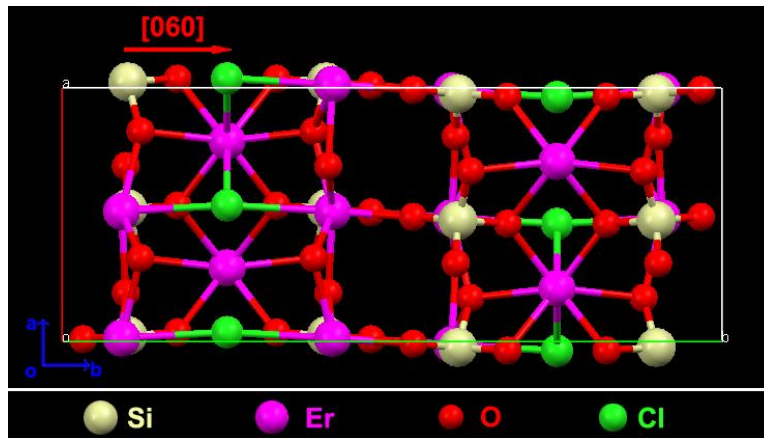
Figure 2.4 Crystal structure of a unit cell of ECS crystal. The white, magenta, red and green balls indicate the silicon, erbium, oxygen and chlorine atoms. The view of the crystal in the xy- (or ab-) plane.

2.3 Transmission Electron Microscopy Analysis

In Chapter 2.2, the crystalline structure of ECS is studied by the XRD analysis. However, the details of the crystalline characteristics of nanowires such as the growth direction of the crystal and quality of the single crystal cannot be observed directly from the XRD measurements. The crystalline characteristics of a single nanowire can be studied by the high-resolution transmission electron microscopy (HR-TEM) approach. For sample preparation, the ECS nanowires were picked up by a tapered optical fiber and transferred on the copper grids with carbon mesh for holding the nanowires. Because the penetrated electron beam cannot penetrate through a thick nanowire, the diameter of the transferred nanowires were less than 100 nm. The TEM image is shown in Figure 2.5. Clear stacking structure along the growth direction of this nanowire can be observed in Figure 2.5(b), indicating the nanowire is a high-quality single crystal. The average distance between the atom layers along the growth direction is 0.87 nm, which matches with the plane-to-plane distance between the atom layers in the [020] direction. The Fourier transform (inset of Figure 2.5(b)) of the TEM image also supports the [020] growth direction. [020] is the same orientation as [060] discussed in Chapter 2.2 but with 3-fold distance between the atom layers. According to the crystal structure analysis in Chapter 2.2, the average distance between the (060) atom layers is 0.29 nm. Therefore, the distance between (020) layers is 0.87 nm. Because this nanowire is a little bit thick, the TEM image is not clear enough to distinguish all 6 atom layers in the [060] direction as shown in Figure 2.4. So a more distinguishable TEM imaging is shown in Figure 2.6. The average distance between the atom layers is 0.29 nm, which is perfectly matched with the layer distance in [060] direction. So there is no doubt that the growth of ECS nanowire is along the y direction (with lattice

constant *b*). Therefore, the cross section plane perpendicular to the growth direction is the

x-z plane with rectangular grids. This can explain why the cross section of the ECS

nanowires is rectangular, as shown in Figure 2.2(c). Since the difference between the lattice

constants *a* and *c* is only 10%, the cross section of the ECS nanowire is close to square

shape.
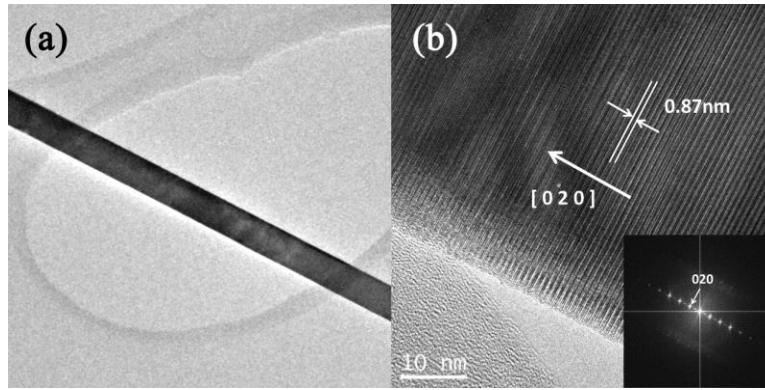
Figure 2.5 (a) Low resolution TEM image of an ECS nanowire on copper grid. (b) HR-TEM image showing the [020] growth direction. Inset: Fourier transform of the HR-TEM image.
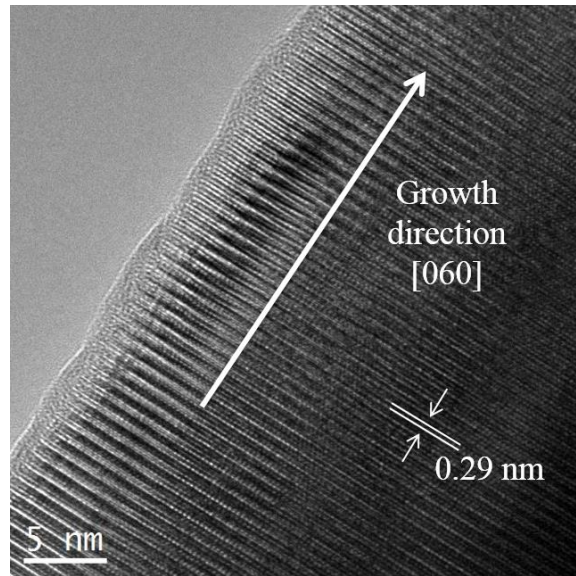
Figure 2.6 TEM image of another ECS nanowire showing the [060] growth direction

23

2.4 Growth of the Core/shell Structure ECS Nanowires

By lowering the substrate temperature to 600 °C, the ECS nanowires can be grown in core/shell structure, with single-crystal silicon at the core region and ECS at the shell region. The TEM and EDS analysis of a single core/shell nanowire dispersed on a copper grid is shown in Figure 2.7. From the low magnification TEM image in Figure 2.7(a), a clear contrast between the core region and the shell region can be observed. The EDS spectrum of the core region (Figure 2.7(b)) shows a much stronger Si signal than the spectrum of the shell region (Figure 2.7(c)), indicating more silicon element in core region. The Cu signals on both spectra are from the copper grid. The EDS mapping of the O, Er, Si, Cl elements are shown in Figure 2.7(d-g). The signal intensities of O, Er and Cl elements is much stronger in shell region than in core region, while the Si signal almost concentrates in the core region, indicating the possibility of the silicon core and ECS shell.

The high-resolution TEM image of the core/shell boundary is shown in Figure 2.7(h). It is clear that the crystal at the two sides of the boundary is quite different. In the shell region the atoms stacks along the growth direction with the average atom plane distance of 0.29 nm, matching with the [060] direction of ECS. The atomic pattern of the core region is more complicated because the atoms from both core and shell are imaged in TEM. The [111] direction of silicon with atom layer distance of 0.31 nm can be distinguished at the core region. The Fourier transform analysis of the high-resolution TEM image shows a strong signal at silicon [111] direction with a complicated ECS pattern in the background (Figure 2.7(i)). Because the ECS shell covers all the direction of the silicon core, the ECS signal cannot be avoided in this transmission electron microscopy. Therefore, the TEM and its Fourier transform at core region show the complicated pattern including both ECS and

24

Si signals. In contrast, the Fourier transfer of shell region only shows the strong ECS pattern without any silicon signal (inset of Figure 2.7(i)). The crystal direction of the shell region is [060].
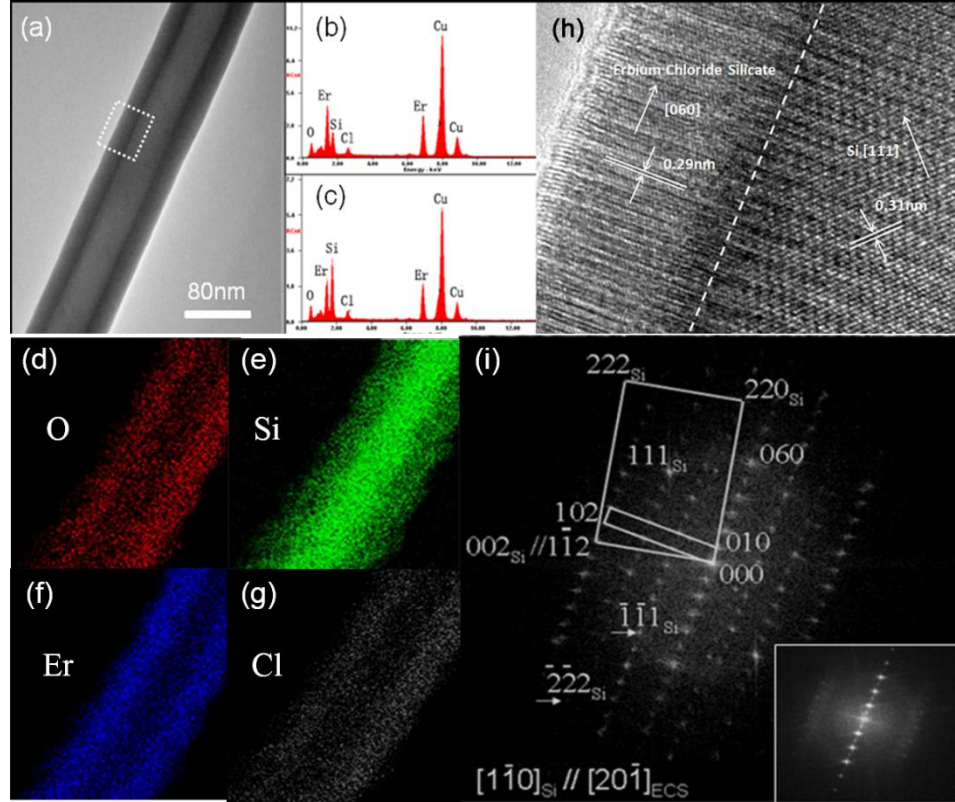
Figure 2.7 TEM and EDS analysis of a core/shell nanowire. (a) TEM image in low resolution. (b,c) The EDS analysis of the shell and core region respectively. (d-g) EDS mapping of O, Si, Er and Cl elements respectively. (h) High-resolution TEM image at the white-box region in (a). Dashed line labels the boundary of the core and shell. Left section is ECS shell. Right section is silicon core. (i) The Fourier transform of the core region in (h). The crystal planes of the ECS crystal and silicon crystal (with subscript "Si") are labeled. Inset: the Fourier transform of the shell region in (h).

The XRD analysis is performed on the core/shell ECS nanowires as shown in Figure 2.8. Both ECS and silicon patterns can be observed. However, comparing to the solid ECS nanowires grown at high temperature, the XRD peaks of the core/shell

nanowires are broader and with a broad background, indicating lower crystal quality in the core/shell nanowires. This is also supported by the poor optical performance of the core/shell ECS nanowires including weaker photoluminescence intensity and shorter photoluminescence lifetime shown in Chapter 3. As a result, the following optical characterization and laser design will be focused on the solid ECS nanowires grown at high temperature.
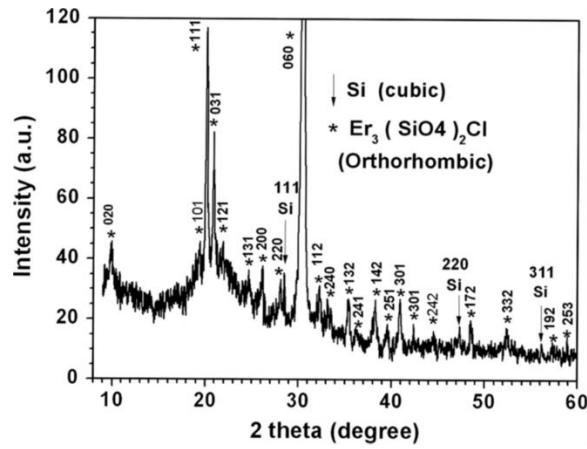
Figure 2.8 XRD of the core/shell nanowires.

However, core/shell ECS nanowires with silicon core have potential with electrically driven devices. It is demonstrated that the electron injection and electroluminescent (EL) is possible in a thin erbium silicate layer [71]. Since the carrier injection in the coaxial nanowire is more efficient than the injection through a solid nanowire [72], we believe the core/shell ECS nanowires have more opportunities in the applications related with EL sources.

CHAPTER 3

OPTICAL SPECTROSCOPY OF ECS NANOWIRES

The optical spectroscopy plays important roles in analyzing the energy structure, transition rates, lifetimes and other optical properties of the materials. In this chapter the optical spectroscopy of the ECS nanowires including the photoluminescence (PL) spectroscopy, power- and temperature-dependent PL, and time-resolved spectroscopy are studied.

Chapter 3.1 presents the PL emission of the ECS nanowires at all emission bands. The energy states of Er^{3+} ions and the detailed sub-level splitting in the fundamental and first excited states are studied. In Chapter 3.2 and 3.3, the power- and temperature-dependent PL are reported. The four-level rate equations are established to understand the PL intensity variation with the pumping power and temperature. In Chapter 3.4, the linewidth of the PL emission at 1.53 μm is studied, demonstrating the high crystal quality of the ECS nanowires. The time-resolved PL spectroscopy and the lifetime analysis is presented in Chapter 3.5.

3.1 Photoluminescence Spectroscopy of ECS Nanowires

Photoluminescence (PL) is the florescence from a material pumped by light (typically lasers). The energy and band structure of the material can be analyzed through the spectroscopy of the florescence. In Chapter 1.4, the energy states of the 4f shell in Er^{3+} ions is discussed, as illustrated in Figure 1.1. With the optical pumping, the Er ions are first excited to from the ground state to higher states, then decay to the lower states in radiative and nonradiative processes. The radiative decay generates the PL emission with the

27

wavelength matching with the transition energy between those two states. The photoluminescence spectrum of the as-grown ECS nanowires are shown in Figure 3.1. The nanowires were pumped by 800 nm Ti:Sapphire laser (Spectra-Physics, Tsunami). The emission spectrum was measured by visible/near-IR spectroscopy system (Jobin Yvon, Triax 320). Figure 3.1 illustrates the photoluminescence spectra of the as-grown ECS nanowires in the range of 450 nm – 1600 nm. The spectra are normalized in each band. The emission bands at 525-546 nm, 650 nm, 800 nm, 980 nm and 1531 nm match well with the transitions from the excited state $^2H_{11/2}/^4S_{3/2}$, $^4F_{9/2}$, $^4I_{9/2}$, $^4I_{11/2}$ and $^4I_{13/2}$ to the ground state $^4I_{15/2}$, as illustrated in the energy-level diagram in Figure 3.2. The 800 nm laser was used as the pumping source since it matches with the $^4I_{15/2}$ to $^4I_{9/2}$ transition, which is known as ground state absorption (GSA). The relaxation from $^4I_{9/2}$ to the lower states gives the PL emission around 800 nm, 980 nm and 1531 nm. Because the pumping wavelength matches with the transition from $^4I_{13/2}$ to $^2H_{11/2}$, the Er ions at the excited state $^4I_{13/2}$ can be further pumped to $^2H_{11/2}$, which is known as excited state absorption (ESA). The relaxation from $^2H_{11/2}$ gives the emission at 546 nm and 650 nm, shorter than the wavelength of the pumping laser. Those emissions are called upconversion. The detail discussion of the ESA and upconversion effect can be found in Chapter 1.5 & 4.5.
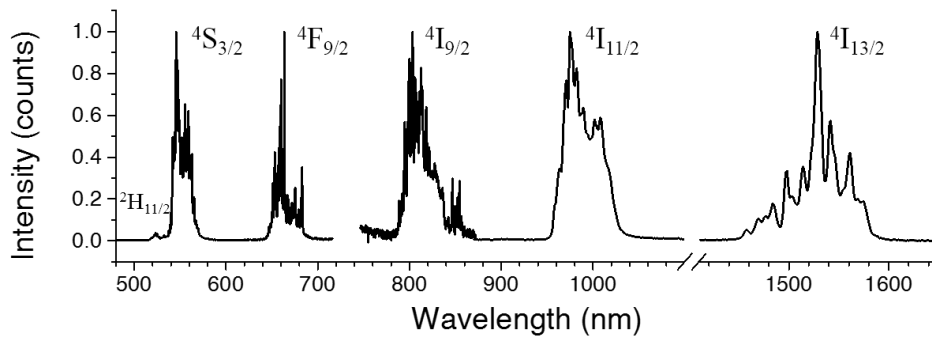
Figure 3.1 PL spectra under 800 nm pumping. The spectra are normalized at each emission band.
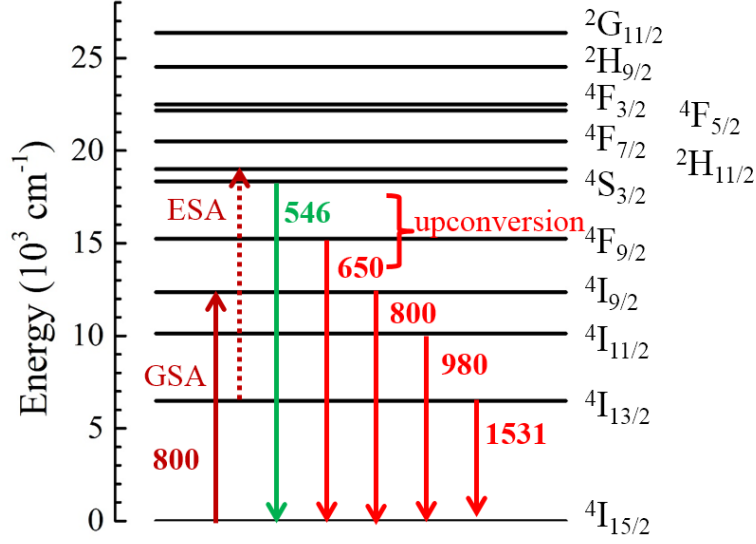
Figure 3.2 Absorption and emission transitions with 800nm laser pumping. The numbers at each emission transition represent the emission wavelengths, with the unit in nm.

Due to the crystalline E-field surrounding the Er ions, each energy state degenerates into several sub-levels. This energy splitting is known as Stark effect or Stark splitting. The maximum number of the split sub-levels of the $^{2S+1}L_J$ state is $g = J + 1/2$ [41]. The group of those sub-levels is called Stark manifold. Since there is no forbidden rule between any two sub-levels in different states, between two Stark manifolds with g_1 and g_2 sub-levels there would be at most $g_1 \times g_2$ emission lines. Thus, the PL in Figure 3.1 shows the broad emission bands containing multiple emission peaks.

Because the Stark splitting strongly depends on the electric field surrounding the Er ions, any defect, imperfection, and thermal vibration of the surrounding crystal can result in the variation of Stark splitting, which is known as the inhomogeneous broadening of the emission linewidth. In the amorphous erbium materials such as the Er-doped glasses, the

29

emission lines are not distinguishable or only distinguishable at very low temperature due to the inhomogeneous broadening [41, 73, 74]. In contrast, in single-crystal ECS nanowires where the Er ions are surrounded with the same E-field environment, clear splitting feature can be observed from the PL spectrum in all transition bands (Figure 3.1) even at room temperature. The narrow emission linewidth is a good demonstration that ECS nanowires are high-quality single crystals.

Figure 3.3 shows the high resolution spectroscopy of a single ECS nanowire at 1.531 μm emission band ($^4I_{13/2}\rightarrow{}^4I_{15/2}$). In order to study splitting of the Stark manifold, this PL spectroscopy was performed at 77K to reduce the linewidth broadening induced by thermal effect. Clearly separated 23 emission peaks can be observed with the highest peak at 1531 nm. As the discussion above, the maximum numbers of sub-levels in $^4I_{13/2}$ and $^4I_{15/2}$ states are 7 and 8 respectively. Thus, there are at most 56 possible transitions in the 1.531 μm emission band. It is reported that in the Er materials with cubic crystalline symmetry, the numbers of sub-levels in $^4I_{13/2}$ and $^4I_{15/2}$ states are 7 and 8 respectively [23, 75]. In the amorphous Er materials, 4-7 and 5-8 sub-levels were observed in $^4I_{13/2}$ and $^4I_{15/2}$ states respectively [73, 76]. In ECS nanowires, 6 sub-levels in $^4I_{15/2}$ and 7 sub-levels in $^4I_{12/2}$ are determined from the high resolution PL spectrum in Figure 3.3. Because the population follows with Boltzmann's Law, the highest peak at 1531 nm corresponds to the transition between the two lowest sub-levels in $^4I_{13/2}$ and $^4I_{15/2}$. The energy of the other sub-levels were calculated accordingly, which are illustrated in Figure 3.4. Theoretically there should be totally $6 \times 7 = 42$ transitions between the two Stark manifolds. However, due to the overlap of the emission wavelengths in some transitions, only 23 emission peaks were observed in the high-resolution PL spectrum. All the transitions are labeled on the spectrum

in Figure 3.3. The blue and red numbers correspond to the levels in upper ($^4I_{13/2}$) and lower ($^4I_{15/2}$) Stark manifolds respectively. Since the crystalline structure of ECS is orthorhombic with $a \neq b \neq c$, a symmetry lower than cubic structure, the numbers of the Stark sub-levels should be equal to the maximum allowed numbers which are 7 and 8 for $^4I_{13/2}$ and $^4I_{15/2}$ manifolds respectively [41, 75]. Possibly due to the small population distribution at sub-levels with high energy and the low response of the spectrometer above 1580 nm, the transitions involved the two highest sub-levels in $^4I_{15/2}$ cannot be observed.
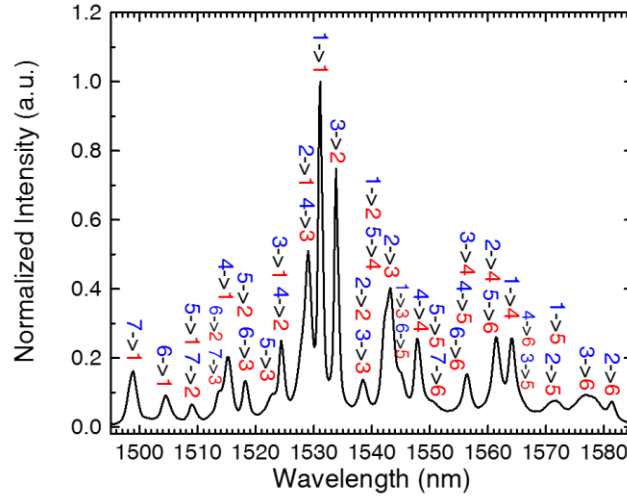
Figure 3.3 High resolution PL spectrum at 1.53um emission band. The numbers of the sub-levels in each transition are labeled at each emission peak.
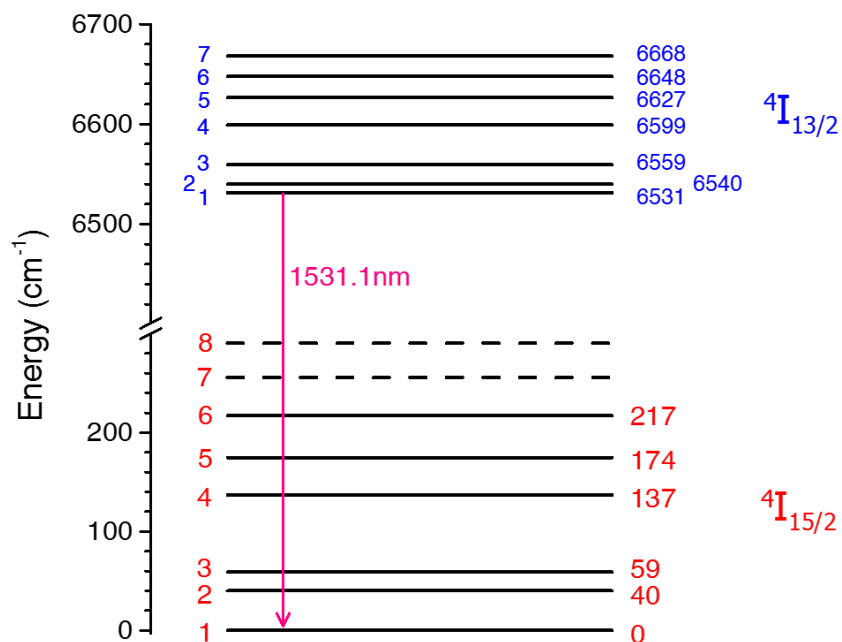
Figure 3.4 Energy diagram of the sub-levels in $^4I_{13/2}$ and $^4I_{15/2}$. The numbers at the right side are the relative energy of the sub-levels with the unit in cm^{-1}.

3.2 Power-dependent Photoluminescence Spectroscopy

The PL intensity is proportional to the Er ion population at the excited state and the radiative life time of that state. It always shows the linear relationship between the PL intensity and pumping power when the pumping is low. However, as increasing the pumping power, the population at the excited state is accumulated, increasing the possibilities of excited state absorption and cooperative upconversion. Therefore, the linearity of power-dependent PL indicate whether the material is suffering upconversion or other nonlinear effect. The power-dependent PL study of ECS nanowires is shown in Figure 3.5. The as-grown ECS nanowires were pumped by 800 nm laser with spot size of 100 μm. The pumping power was increased up to 800 mW by a continuous variable neutral

32

density filter. The integrated PL intensity as a function of pumping power density is plotted in log-log scale in Figure 3.5. The guiding lines are the linear fittings of both bands. The PL intensities of both 1.53 μm and 0.98 μm emission have linear relationship with the pumping power in over three orders of magnitude. When the pumping power density is above 1 kW/cm^2, the 1.53 μm emission shows a sub-linear deviation from the linear fitting (black solid line) due to the population accumulation at excited states which causes the excited state absorption and the cooperative upconversion.
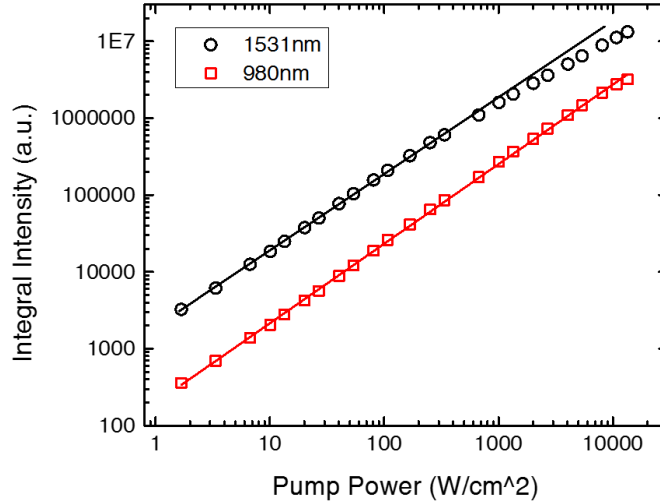
Figure 3.5 Power dependent PL emission at 1531 nm (black circles) and 980 nm (red squares) bands. The solid lines are the linear fittings.
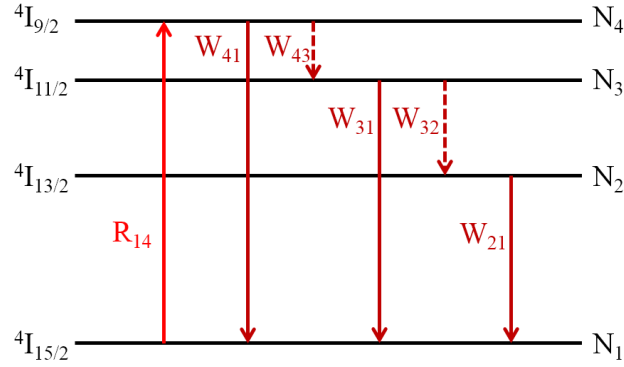
Figure 3.6 Energy level diagram showing the transitions in 4-level system.

The rate equations of 4-level system are studied to further understand the linear and non-linear behavior in the power-dependent PL. The energy-level diagram of 4-level system is shown in Figure 3.6. Level 1 is the fundamental state ($^4I_{15/2}$) and levels 2, 3, 4 refer to the excited states $^4I_{13/2}$, $^4I_{11/2}$, $^4I_{9/2}$ respectively. 800 nm laser excites the Er ions from level 1 to level 4 with the pumping rate of R_{14}, which is equal to the product of the pumping power density and the absorption cross section of transition 1→4. There are two dominant decay processes from level 4 to the lower levels: nonradiative process W_{43} and radiative process W_{41} (emission wavelength 0.8 μm). The radiative decays from level 4 to level 3 and level 2 are neglected. Similarly the decay from level 3 is dominant by the nonradiative process W_{32} and radiative process W_{31} (emission wavelength 0.98 μm). For the decay from both level 3 and level 4, the nonradiative decay is typically much larger than the radiative decay (W_{43}>>W_{41}, W_{32}>>W_{31}). The decay from level 2 to ground level 1 (rate W_{21}) is also essentially radiative with emission wavelength of 1.53 μm ($W_{21} = W_{21}^R + W_{21}^{NR} \approx W_{21}^R$). The ion populations in level 1, 2, 3, 4 are N_1, N_2, N_3, N_4 respectively. The total ion density is $N = N_1 + N_2 + N_3 + N_4$. Then the rate equations can be listed as below:

$$\frac{dN_1}{dt} = -R_{14}N_1 + W_{41}N_4 + W_{31}N_3 + W_{21}N_2 \tag{3.1}$$

$$\frac{dN_2}{dt} = -W_{21}N_2 + W_{32}N_3 \tag{3.2}$$

$$\frac{dN_3}{dt} = -W_{32}N_3 - W_{31}N_3 + W_{43}N_4 \tag{3.3}$$

$$\frac{dN_4}{dt} = R_{14}N_1 - W_{41}N_4 - W_{43}N_4 \tag{3.3}$$

To simplify the calculation, the excited state absorption of the 800 nm pumping from level 2 to higher level is not considered in the rate equations. Under equilibrium condition, all the time differential terms are equal to zero. The lifetimes of the excited level 2, 3, 4 are $\tau_2 = 1/W_{21}$, $\tau_3 = 1/(W_{31} + W_{32}) \approx 1/W_{32}$, $\tau_4 = 1/(W_{41} + W_{43}) \approx 1/W_{43}$. Typically level 2 is more stable than the higher levels, that is $\tau_2 \gg \tau_3, \tau_4$ [4, 41, 77, 78]. For ECS nanowires, the lifetime of level 2 is typically 0.1-0.5 ms (detailed measurement can be found in Chapter 3.4). Then the populations in level 2 and level 3 can be obtained:

$$N_2 = \tau_2(W_{43}\tau_4)(W_{32}\tau_3)\frac{R_{14}N}{1 + R_{14}\tau} \tag{3.5}$$

$$N_3 = \tau_3(W_{43}\tau_4)\frac{R_{14}N}{1 + R_{14}\tau} \tag{3.6}$$

where $\tau = (W_{43}\tau_4)(W_{32}\tau_3)\tau_2 + (W_{43}\tau_4)\tau_3 + \tau_4 \approx \tau_2 + \tau_3 + \tau_4 \approx \tau_2$.

The emission intensities from level 2 to level 1 (1.53 μm) and from level 3 to level 1 (0.98 μm) are proportional to the population on level 2 and 3:

$$I_{21} = \frac{hc}{\lambda} \cdot W_{21}^R N_2 \tag{3.7}$$

$$I_{31} = \frac{hc}{\lambda} \cdot W_{31}^R N_3 \tag{3.8}$$

where W_{21}^R and W_{31}^R are the radiative transition rate from level 2 and level 3 to level 1.

Notice that the populations on both level 2 and 3 are proportional to the pumping rate R_{14} with a non-linear term $1 + R_{14}\tau$. For the power-dependent measurement shown in Figure 3.5, $R_{14}\tau$ is roughly equal to 0.1 at the maximum pumping which is 10^4 W/cm^2. As a result, the non-linear term is close to 1 under the low pumping condition, which makes the linear relationship of emission intensity and pumping power in a wide range.

Besides the non-linear term $1 + R_{14}\tau$, the ESA of 800 nm pumping laser is another important factor of the sub-linear behavior at high pumping power. Because the pumping wavelength matches with the transition from $^4I_{13/2}$ to $^2H_{11/2}$, as shown in Figure 3.2, the ions at level 2 can be further pumped to the $^2H_{11/2}$ state and then decay to level 4 and 3. The ESA is a second-order process since the transition rate is quadratic to the pumping power. Therefore, with high pumping power, the population of level 2 is significantly reduced while the population of level 3 is not, resulting in the sub-linear deviation only in the power-dependent PL of the 1.53 μm emission.

3.3 Temperature-dependent Photoluminescence Spectroscopy

In this section, the thermal stability of ECS nanowires is studied. Figure 3.7 shows the temperature-dependent PL intensity at 1.53 μm from 77 K (liquid nitrogen) to 295 K (room temperature). The as-grown ECS nanowires were put in a cryostat (Janis, ST-500) for temperature controlling and were pumped with 800 nm laser at a constant power. From the temperature-dependent PL in Figure 3.7, the quenching of the emission intensity is only 20% from 77 K to 295 K, demonstrating the good thermal stability of the ECS nanowires. It is reported that the thermal quenching is more than 95% in some Er-doped materials

especially in the Er-doped semiconductor materials [64, 79, 80], Such large quenching is due to the Auger effect which transfers energy from Er ions to the carriers [64, 79]. In the Er-compounds with high crystal quality, the temperature quenching effect is not significant [33, 34]. The good thermal stability of the ECS nanowires allows the stable performance as the amplifiers or lasers in a wide temperature range.
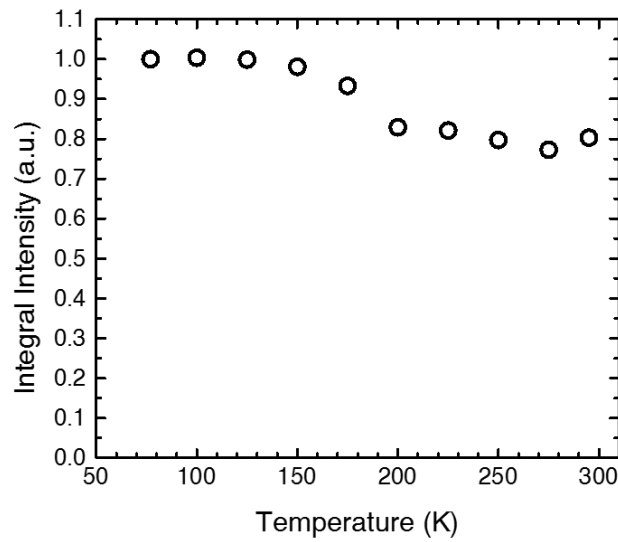
Figure 3.7 Temperature-dependent PL from 77 K to 295 K.

3.4 Emission Linewidth of the ECS Nanowires

The emission linewidth of erbium material is associated with two effects: homogenous broadening and inhomogeneous broadening. The homogeneous broadening is generated from the lattice vibration which is related to temperature. The inhomogeneous broadening is caused by the spatial variation of the Stark splitting. Since the energies of the split sub-levels are determined by the E-field surrounding the Er ions, any change in

the crystal structure will result in the variation of the sub-level energies. Therefore, the inhomogeneous broadening is strongly related to the crystal quality of the erbium materials. For those amorphous materials such as Er-doped glasses, the emission linewidth is dominant by the inhomogeneous broadening which is typically larger than 10 nm, making the emission lines of the sub-levels not distinguishable [14, 16, 41, 65]. For the Er-doped single-crystalline materials and the Er-compounds, the emission linewidth is dominant by the homogeneous broadening. The inhomogeneous broadening of those crystalline materials is mainly from the defects, dislocations and any crystalline imperfection [23, 33, 34, 81]. As a result, the PL emission linewidth is a good indication of the crystal quality of our ECS nanowire.

Figure 3.8(a) shows the temperature-dependent PL spectra of a single ECS nanowire from 77 K to 295 K. The emission lines are clearly separated even at room temperature. The linewidth of the 1.531 μm peak as a function of temperature is plotted in Figure 3.8(b). The linewidth is only 2 nm at room temperature. It reduces to 0.7 nm at 77 K due to the reduction of homogeneous broadening. Compared to the linewidth of other crystalline erbium compounds reported in literature [31, 33, 34, 81], the PL linewidth of ECS nanowires is much smaller at both room temperature and low temperatures, demonstrating the high crystalline quality of our ECS nanowires.
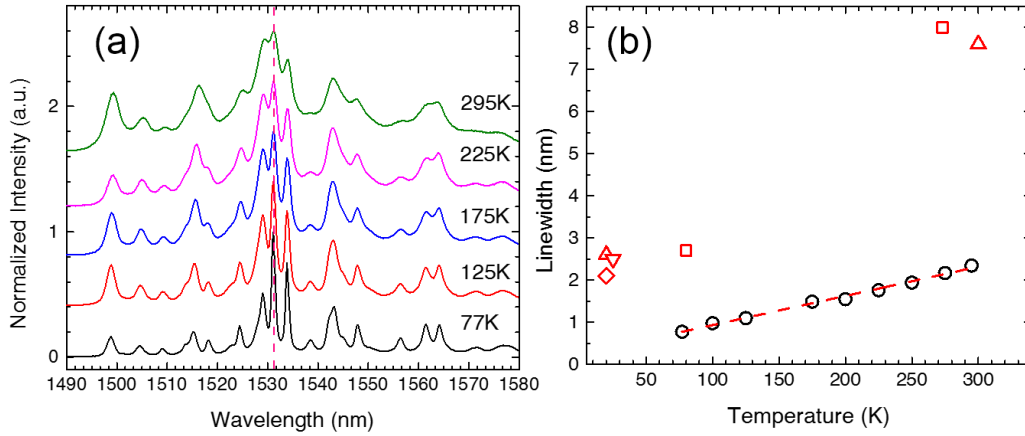
Figure 3.8(a) High resolution PL spectra from 77 K to 295 K. (b) Linewidth of 1531 nm peak at different temperatures (black circle). Red line: linear fitting of the temperature-dependent linewidth. Red symbols: PL linewidths of the Er compounds reported in literature [31, 33, 34, 81].

The gain and gain bandwidth is always a trade-off in Er materials. For the non-crystalline materials, the gain is low because the Er ions distribute in a wide range of the energy levels. For the crystalline materials, the population of the excited Er ions are concentrated in certain sub-levels with small distribution of the energy. Therefore, the peak gain of crystalline material is higher than the amorphous material. However, associated with the emission linewidth, the gain bandwidth of the crystalline Er material is narrower. Therefore, the single-crystal ECS nanowires have higher gain but narrower bandwidth, offering the potential applications in miniature laser sources and narrow-band amplifiers.

3.5 Photoluminescence Lifetime of the ECS Nanowires

When the Er^{3+} ions are excited from the fundamental state $^4I_{15/2}$ to the excited states $^4I_{13/2}$, $^4I_{11/2}$, $^4I_{9/2}$…, the ions at higher states quickly decay to the metastable state $^4I_{13/2}$, which has relatively longer lifetime. As a results, for the amplification purpose, the population

inversion of the $^4I_{13/2}\rightarrow{}^4I_{15/2}$ transition depends on the lifetime of the metastable state $^4I_{13/2}$. The fluorescence or PL lifetime of the metastable state can be written as two parts: radiative lifetime τ_{rad} and nonradiative lifetime τ_{NR}, through Equation 3.9:

$$\frac{1}{\tau} = \frac{1}{\tau_{rad}} + \frac{1}{\tau_{NR}} \tag{3.9}$$

where $\tau_{rad} = 1/W_{21}^R$, $\tau_{NR} = 1/W_{21}^{NR}$. W_{21}^R and W_{21}^{NR} are the radiative and non-radiative transition rates respectively.

One major non-radiative transition is homogeneous upconversion [44, 82], which is caused by the interaction between the ions at the metastable state $^4I_{13/2}$. A donor ion transfers its energy to an acceptor ion, making one ion go back to ground state $^4I_{15/2}$ and the other ion be excited to the higher state $^4I_{9/2}$. The excited ion quickly decays back to $^4I_{13/2}$ so finally there is only one ion at the metastable state. The homogeneous upconversion rate strongly relies on the distance between the Er ions. When the Er concentration is low, the Er ions are far away from each other, lowering the energy transfer rate between the ions. In the low Er-concentration materials, the PL lifetime is dominant by the radiative lifetime, which is typically 10 ms [83]. However, the gain in those materials is also low. As increasing the Er concentration, the rapid energy transferring occurs between the neighboring ions in short distance, which dramatically reduces the PL lifetime. The increase of the non-radiative transition rate and the decrease of PL lifetime is called concentration quenching. The PL lifetime τ and the Er concentration ρ typically follows with the equation below [18, 82, 84]:

$$\tau = \frac{\tau_0}{1 + (\rho/Q)^p} \tag{3.10}$$

where τ_0 is the ideal lifetime when concentration is zero, Q is called quenching concentration and p is the exponential index. For the typical Er-doped glasses, τ_0 is 6-14 ms, Q is $10^{19} - 10^{20}$ cm^{-3}, and p is $1 - 2$ [82, 85]. The optimized Er concentration of such materials is $10^{19} - 10^{20}$ cm^{-3}. When the Er concentration is further higher, the Er ions are uniformly distributed in the host materials and the erbium clusters with locally high Er concentration are formed. Such Er clusters significantly raise the concentration effect, resulting the rapidly decay of the lifetime. According to Equation 3.9, the PL lifetime is less than 0.01 ms when the Er concentration is above 10^{22} cm^{-3}, which is even comparable to the lifetime of state $^4I_{11/2}$. Therefore, the Er concentration of the doped materials are limited at 10^{20} cm^{-3} which confines the optical gain in such materials. However, for single-crystal ECS nanowires, the erbium ions are exactly located in their positions in the lattice, reducing the possibility to form the cluster. Therefore, the concentration quenching effect can be minimized in ECS nanowires.

Figure 3.9 shows how the PL lifetime is measured. The ECS nanowires were pumped with pulsed laser (Spectra-Physics SDL-824, 1000 Hz) with wavelength at 667 nm which matches with the transition $^4I_{15/2} \rightarrow ^4F_{9/2}$. 8% of the laser beam was split to a high speed silicon detector (Thorlabs, DET10A) as the reference signal. The pumping power is small enough to avoid the excited state absorption and the cooperative upconversion effects. The PL emission was collected by an objective and guided to the photomultiplier tube (PMT) detector (Hamamatsu, H10330A). To select the 1.53 µm emission band, a 1064 nm long-pass filter is applied before the PMT detector. Both reference and PL signals were connected to the multichannel scalar (Stanford Research System, SR430) for the time-

resolved photon counting. Since the lifetime is in microsecond to millisecond scale, the electric wire decay time can be neglected.
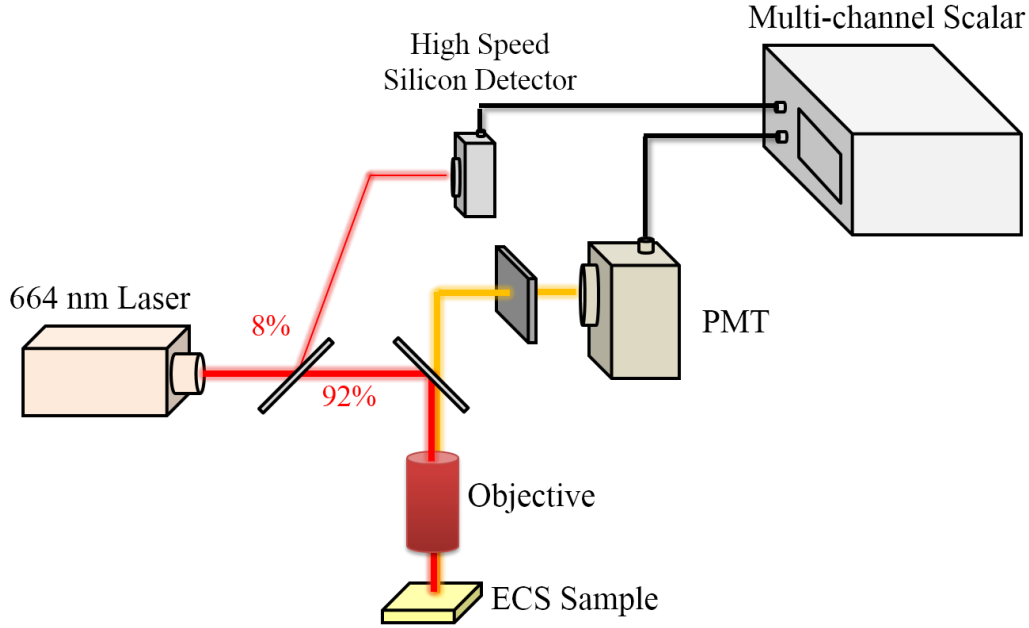
Figure 3.9 Schematic of the PL lifetime measurement system.

The PL lifetime of the ECS nanowires is 0.54 ms, which is lower than the lifetime of the Er-doped materials with Er concentration around 10^{20} cm^{-3}, as shown in Table 3.1. It is reasonable since the Er concentration of ECS is at least 2 order of magnitude higher. But comparing to the lifetime of the erbium compounds with Er concentration at the level of 10^{22} cm^{-3}, the lifetime of ECS is much longer. This is attributed to the high crystal quality of ECS nanowires with no clustering of the Er ions, which causes the concentration quenching.

Table 3.1 PL lifetime of ECS nanowires and other erbium materials from literature [16, 32, 65, 81, 82, 86-88].

ref	Material (or host)	Crystalline type	Er concentration (cm^{-3})	PL lifetime (ms)
This work	ECS	Single crystalline	1.62×10^{22}	0.54
[82]	Silica	Amorphous	1.4×10^{20}	3.2
[16]	Sodium-silicate	Amorphous	2×10^{20}	7.2
[65]	Phosphate	Amorphous	1×10^{20}	8.4
[86]	Al_2O_3	Amorphous	2×10^{20}	8.6
[87]	EYS	Polycrystalline	1×10^{21}	2
[88]	EYbS	Polycrystalline	1.4×10^{21}	5
[81]	ES	Single crystalline	2×10^{22}	0.04
[87]	EYS	Polycrystalline	1.9×10^{22}	0.015
[32]	Er_2O_3	Polycrystalline	2.7×10^{22}	0.062

To further demonstrate the influence of the crystal quality to the PL lifetime, we compared the lifetime of two ECS samples grown at different temperature. As seen from the XRD analysis in Figure 3.10(b), the XRD lines of the high-temperature sample are clear and narrow, while the XRD lines of the low-temperature sample are broad and with a high background, indicating the good crystal quality of the high-temperature sample and bad crystal quality of the low-temperature sample. The time-resolved PL in Figure 3.10(a) clearly shows a longer lifetime in the high-temperature sample. The crystalline defects rise the non-radiative transition rate and the possibly clustering of the erbium ions further increases the concentration quenching effect. Thus, the low quality sample has shorting PL lifetime.
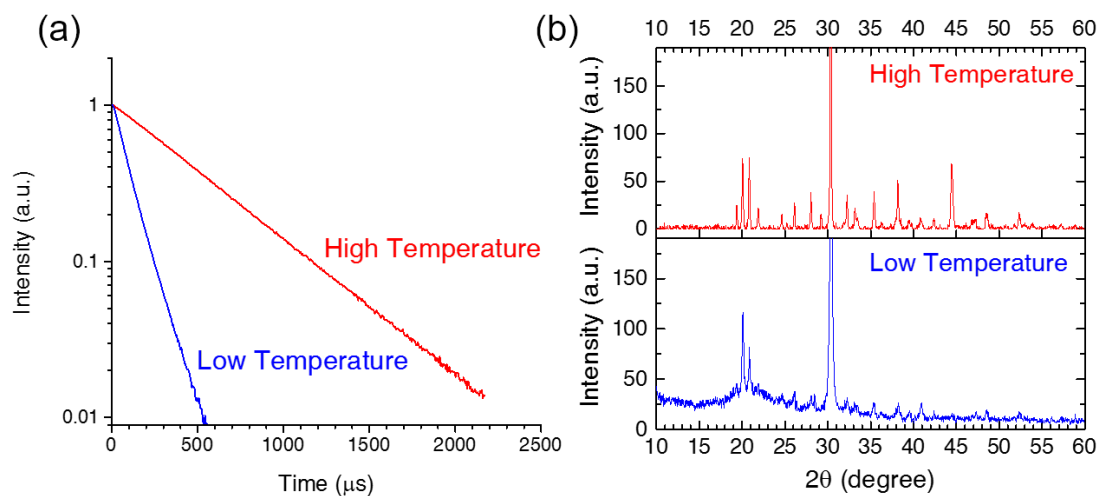
Figure 3.10 (a) Lifetime and (b) XRD of the ECS nanowire grown at low temperature and high temperature.

CHAPTER 4

NET OPTICAL GAIN IN SINGLE ECS NANOWIRE

Since the success of the Er-doped fiber amplifiers and lasers in the last two decades [1, 2], the Er-doped materials have been extensively studied [3-8, 15, 19]. One important goal of research is to obtain high gain in Er materials to realize miniaturized laser sources and amplifiers for the integrated photonic devices. Increasing the doping density is one efficient way to enhance the gain in Er-doped materials. However, according to the discussion in Chapter 3.5, when the Er-concentration is higher than 10^{20} cm^{-3}, the concentration quenching effect will significantly reduce the PL lifetime as well as the optical gain. The optimized Er-concentration in the Er-doped materials is between $10^{20} – 10^{21}$ cm^{-3}, with net gain in single digit dB per centimeter [14, 15, 20, 86]. In order to reduce the concentration quenching effect in the high Er-concentration materials, the single-crystalline and polycrystalline Er-compounds such as erbium oxide [32, 38, 89] and erbium silicate [33, 34, 68, 81, 90] are developed. Because the Er ions in Er-compounds are uniformly incorporated in the crystalline structure, the Er clusters which cause the strong quenching effect can be minimized. However, due to the difficulty in the growth of high quality Er-compounds, currently there is no report of the high net gain in such Er-compounds.

ECS contains Er-concentration over 10^{22} cm^{-3}. In the previous chapters, we demonstrated that the ECS nanowires are high-quality single-crystalline structure with long PL lifetime. Therefore, the ECS nanowires are potentially the high gain material. In this chapter, the methods to study the signal enhancement and absorption coefficient in single nanowire are developed. More than 30 dB/cm net gain is demonstrated in a single ECS

nanowire. By simulating a three-level system, the upconversion rate and the population inversion in the nanowire are studied, demonstrating a higher peak gain in the ECS nanowire.

4.1 Introduction to Internal Net Gain in Erbium Waveguide

The internal net gain is defined as the amplification of the signal intensity per unit length of propagation inside an amplifier. The internal net gain is an intrinsic property of the amplifier without taking into account the coupling efficiency between the amplifier and the external waveguides, which is not always constant. Therefore, the internal net gain is a good indication of the amplification capability of the amplifier.
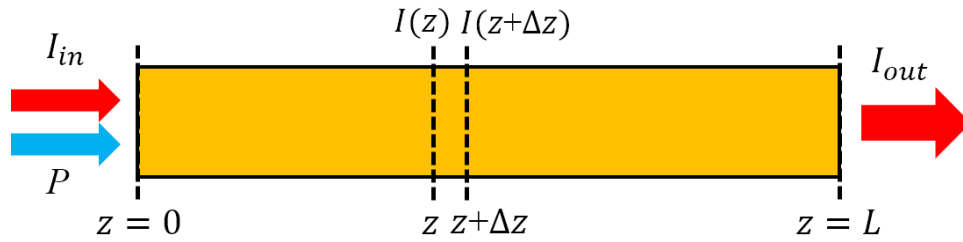
Figure 4.1 Schematic of the signal amplification in erbium waveguide.

The internal net gain can be determined by the following processes. As shown in Figure 4.1, the Er waveguide amplifier is injected with an input signal I_{in} and the pumping P from one end. The signal output I_{out} is collected from the other end. Inside the amplifier, the signal intensity follows with:

$$I(z + \Delta z) = I(z)e^{(\Gamma g(z) - \alpha_p)dz} \tag{4.1}$$

Γ is the confinement factor of the waveguide. α_p is the propagation loss due to the leaking and scattering in the waveguide. $g(z)$ is the material gain at location z, which is equal to:

$$g(z) = \sigma_{em}N_2(z) - \sigma_{abs}N_1(z) \tag{4.2}$$

σ_{em} and σ_{abs} are the emission and absorption cross sections respectively at the input wavelength. N_2 and N_1 are the population of erbium ions at the excited state and ground state respectively. The emission and absorption cross sections are roughly equal at 1.531 μm [12, 14]. Therefore, the population is inverted, when $N_2 - N_1 > 0$, giving the positive material gain. The population inversion does not indicate the output signal is amplified due to the propagation loss inside the amplifier and the coupling loss between the external waveguide and the amplifier. However, for the material characterization, the material gain is still an important demonstration of the amplification potential of erbium materials, especially for the high Er-density materials which have difficulties in the population inversion due to the concentration effect.

The output signal intensity can be written as:

$$I_{out}(P) = CI_{in}e^{\int(\Gamma g(z) - \alpha_p)dz} = CI_{in}e^{g_{int}(P)L} \tag{4.3}$$

where C is the total coupling efficiency into and out of the waveguide. g_{int} is the internal net gain, defined as

$$g_{int}(P) = \frac{1}{L}\int \Gamma(\sigma_{em}N_2(z,P) - \sigma_{abs}N_1(z,P))dz - \alpha_p$$

$$= \frac{1}{L}\int \Gamma((\sigma_{em} + \sigma_{abs})N_2(z,P) - \sigma_{abs}N1)dz - \alpha_p \tag{4.4}$$

$$= \Gamma(\sigma_{em} + \sigma_{abs})\overline{N_2}(P) - \Gamma\sigma_{abs}N1 - \alpha_p$$

$N \equiv N_1 + N_2$ is the total erbium concentration. $\overline{N_2}(P)$ is the average population along the waveguide, as a function of the pumping power P. The internal net gain consists of three

parts: amplification by the pumping ($\Gamma(\sigma_{em} + \sigma_{abs})\overline{N_2}(P)$), material absorption ($\Gamma\sigma_{abs}N$) and propagation loss ($\alpha_p$). The first part is known as signal enhancement (SE), defined as the ratio of the output signal intensity with to without pumping.

$$SE = \frac{I_{out}(P)}{I_{out}(0)} = e^{(g_{int}(P) - g_{int}(0))L}$$

$$= e^{\Gamma(\sigma_{em} + \sigma_{abs})\overline{N_2}(P)L}$$

(4.5)

Without the pumping, the population at the excited state (N_2) is equal to zero. We assume the small signal condition that the input signal is small enough to avoid the population accumulation at excited state. SE can be easily measured by the amplification of the output signal from pumping-off to pumping-on. Therefore, SE is also called on-off gain. The average SE per unit length can be written as:

$$SE = \frac{1}{L} \times ln\left(\frac{I_{out}(P)}{I_{out}(0)}\right) = \Gamma(\sigma_{em} + \sigma_{abs})\overline{N_2}(P)$$

(4.6)

From Equation 4.4 and 4.6, the internal net gain can be determined through:

$$g_{int} = SE - \Gamma\sigma_{abs}N - \alpha_p$$

(4.7)

For a good waveguide the propagation loss is typically lower than 1 dB/cm [86] which is ignorable when the internal gain is large. Therefor the internal net gain is only related to the SE and the absorption. The following sections will present the measurement of the SE in a single ECS nanowire and the absorption cross section σ_{abs} of ECS nanowire. Finally the net optical gain in a single ECS nanowire is demonstrated.

4.2 Signal Enhancement in Single ECS Nanowire

The signal enhancement is measured by pump-probe method, as shown in Figure 4.2. The probe signal was generated by a tunable laser in $1528 - 1540$ nm. The laser power was controlled in small-signal condition as described in Chapter 4.1. A continuous-wave 980 nm laser diode was used as the pumping source. According to the analysis in Chapter 1.5, 980 nm excitation is the best pumping source due to the least excited state absorption, which allows the maximum population inversion at the state $^4I_{13/2}$. Both pump and probe lasers were combined through the wavelength-division multiplexing (WDM) and coupled into a tapered fiber for signal injection. A single ECS nanowire was placed on the silicon substrate coated with Au film for maximizing the confinement. The signal was coupled into the nanowire through a tapered fiber. The amplified signal was coupled out through another tapered fiber which was connected to the spectrometer. The tapered fibers were fabricated by heat-and-pull approach. The tip size in 1-2 μm matches the diameter of the nanowire. In order to maximize the coupling efficiency between the tapered fibers and the nanowire, the tapered fibers directly contact the nanowire ends with a small angle to the substrate, as shown in Figure 4.3(a). Limited by the diameter of the fiber before the tapered range (125 μm) and the tapering profile, this angle is roughly 5-10°. The total coupling loss is $10 - 15$ dB. The detail information of the fiber-nanowire coupling system can be found in Appendix A.
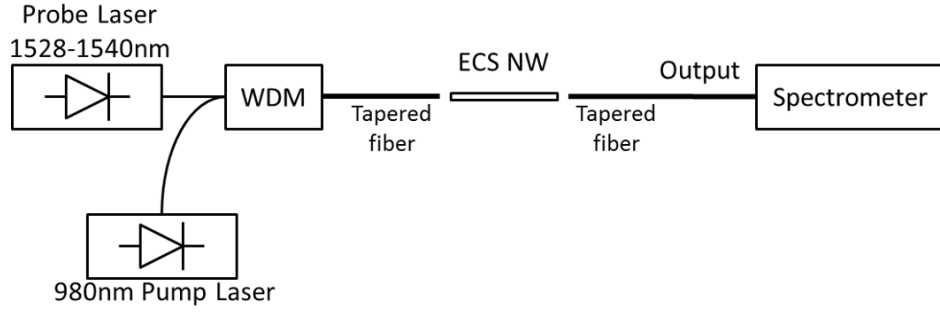
Figure 4.2 Schematic of the pump-probe measurement setup.
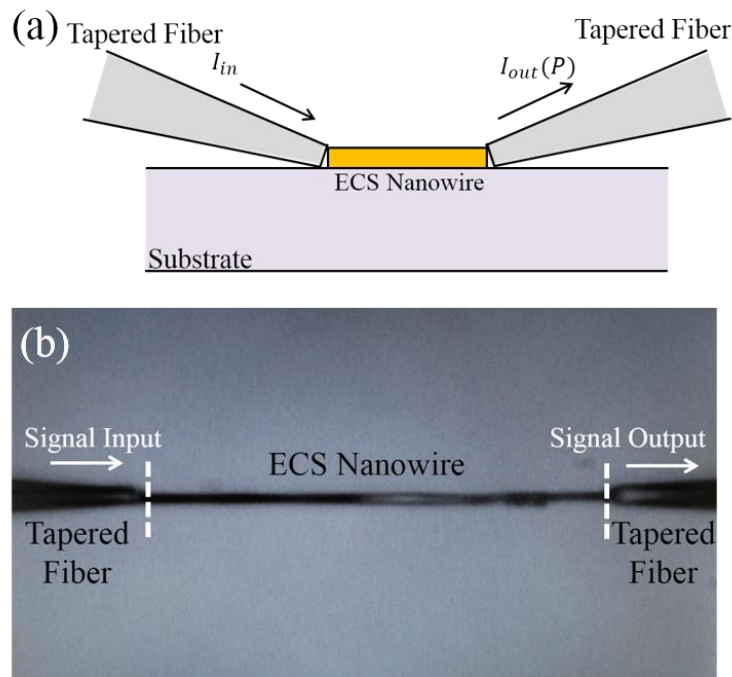
Figure 4.3 (a) Side view of the fiber-nanowire-fiber coupling configuration. (b) Top view image of the fiber-nanowire-fiber coupling.

In the measurement, 7 dB SE was demonstrated in a 109 μm-long ECS nanowire at 1531 nm, the PL peak wavelength. The average SE per unit length is 644 dB/cm. The SE as a function of pumping power is plotted in Figure 4.4(a). The pumping power is measured at the tip of the tapered fiber. It can be seen that the SE is not fully saturated due to the limitation of the 980 nm pumping power. Therefore, the potential SE in this ECS nanowire

50

should be higher than 644 dB/cm. The detail discussion of the peak gain and population inversion along this nanowire will be presented in Chapter 4.5.

Figure 4.4(b) shows the SE at different wavelengths under the maximum pumping. The peak SE is at 1531 nm, which is equal to the peak wavelength of the PL spectra. The shape of the SE spectrum also has good agreement with the emission spectrum shown as the inset of Figure 4.4(a).
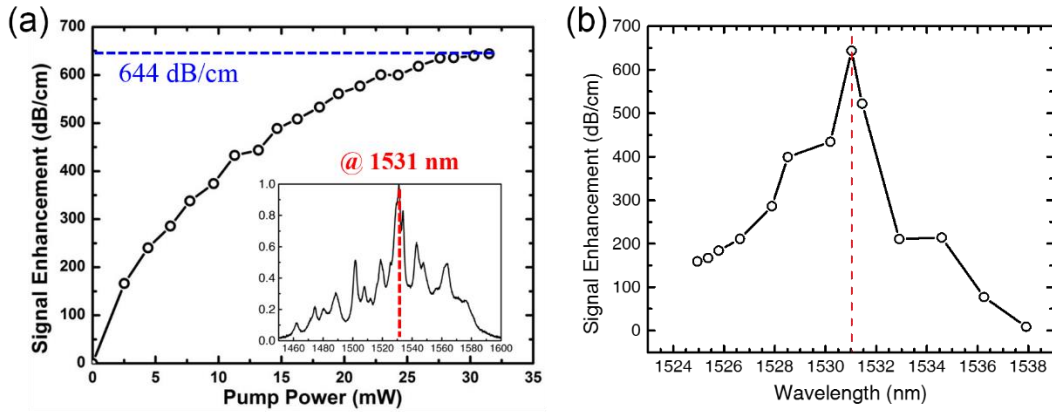
Figure 4.4 (a) SE per unit length versus the pumping power at 1531 nm. Inset is the emission spectrum of ECS nanowire. The main peak wavelength is 1531 nm. (b) SE under the maximum pumping (31.5 mW) at different wavelengths. The dashed line shows the peak SE at 1531 nm.

Table 4.1 lists the SE of ECS nanowire and other Er materials. It is reasonable that the ECS has over one order of magnitude higher SE than the other Er materials since the Er-concentration in ECS is much higher. This is a good indication that the potential gain in ECS nanowires is much higher, although it is not necessary that the net gain of ECS can be achieved because the absorption coefficient is still unknown.

Table 4.1 SE of ECS nanowires and other erbium materials [15, 36, 66, 67].

Ref.	Material (or host)	Crystalline type	Er concentration (cm^{-3})	Signal Enhancement (dB/cm)
This work	ECS	Single crystalline	1.62×10^{22}	644
[15]	Phosphate	Amorphous	5.3×10^{20}	14
[66]	Al_2O_3	Polycrystalline	2.7×10^{20}	14
[36]	EYS	Polycrystalline	1.7×10^{20}	10
[67]	Silicon-rich-SiO_2	Polycrystalline	1×10^{20}	15

4.3 Absorption Cross Section Measurement of Single ECS Nanowire

Absorption cross section is the ability of an Er ion to absorb the photons, which is equal to

$$\sigma_{abs} = \alpha/N \tag{4.8}$$

α is the absorption coefficient of the material and N is the Er concentration. The absorption

coefficient is typically determined from the absorption spectrum, but the difficulty has been

met in single nanowire. Several approaches to measure the absorption coefficient were

attempted. The first method is to measure the transmission spectrum using the

configuration similar to Figure 4.3(a). However, the coupling loss between the fibers and

nanowire varies with the wavelength, introducing a huge error to the absorption spectrum.

The second attempt is to measure the absorption spectra from a thick layer of the ECS

nanowire ensemble by the integrating sphere. This is similar to the absorption measurement

on a thin film. However, only the relative absorption spectra can be obtained due to the

unknown effective thickness of the nanowire layer. The other methods based on scanning

the length of the waveguide such as variable stripe length method [91] are not applicable

to the ECS nanowire waveguide, since those methods require a large variation of the

waveguide length (1-10 mm) but the ECS wires are too short (around 100 μm).

After various considerations, we designed an indirect method to determine the absorption coefficient at the desired wavelength. As shown in Figure 4.5, an ECS nanowire is placed at the edge of a quartz substrate with half of the nanowire hanging outside the substrate. The suspending section surrounded by the air maximizes the confinement factor and minimizes the propagation loss. 1.531 μm pumping laser is delivered to the nanowire through the suspending end with a commercial lensed fiber (OZ Optics, DTS00800). Due to the absorption, the intensity of the pumping laser, p, decays along the nanowire waveguide. The decay function is

$$p = p_0 e^{-(\Gamma\alpha + \alpha_p)x} \tag{4.9}$$

where p_0 is the power of the pumping laser coupled into the suspending end, α is the absorption coefficient at 1.531 μm, Γ is the confinement factor and α_p is the propagation loss. Since the propagation loss is typically smaller than 1 dB/cm [86], it can be neglected compared to absorption which is the hundreds dB/cm. The green emission is a second-order upconversion effect including the cooperative upconversion and excited state absorption as shown in Figure 4.6. The intensity of the green upconversion has the following relation with the power of 1.531 μm laser,

$$I_{green} \propto p^m \approx p_0^m e^{-m\Gamma\alpha x} \tag{4.10}$$

For the green upconversion which is a second-order effect, the power factor m is smaller than 3 [81, 89]. Therefore, the absorption coefficient can be derived from the decay rate of the green upconversion, as $\alpha = \alpha_{green}/(m\Gamma)$.

53
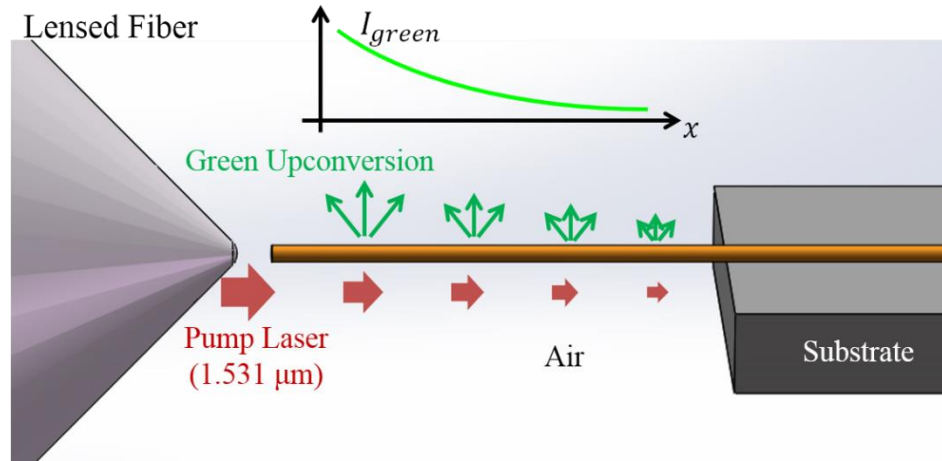
Figure 4.5 Configuration of the absorption measurement on single ECS nanowire.
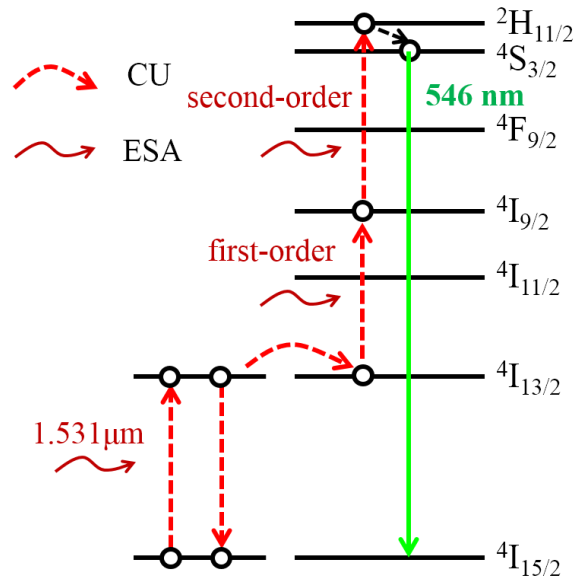
Figure 4.6 Energy level diagram showing the second-order upconversion and the green emission.

The measurement was performed under a high-magnification microscope. As shown in Figure 4.7(a), an ECS nanowire with diameter of 900 nm was placed at the edge of a quartz substrate. The left segment of nanowire of 40 μm in length was suspending outside the substrate. 1.531 μm pump laser was injected to the nanowire though a lensed

fiber, with power of 0.1 mW measured at the tip of the lensed fiber. The spatial distribution of the green upconversion was imaged by a CCD camera, as shown in Figure 4.7(b). The gamma correction of the CCD camera was set as 1, ensuring the intensity in the recorded image is proportional to the emission intensity [92]. The intensity of the green upconversion along the nanowire is plotted in Figure 4.7(c). Clear exponential decay of the upconversion can be observed at the suspending section of the nanowire. The fitted decay rate is 1345 dB/cm. Because of the small diameter of the nanowire and the small index difference between the ECS nanowire and the quartz substrate (n_{ECS}<1.7, n_{quartz}=1.55), there is no guided propagation on the right side of the nanowire. The pump signal as well as the upconversion quickly decay to zero, enabling a one-way propagation.

The upconversion power factor m was obtained by the power-dependence of the green upconversion by 1.531 μm pumping, which is shown in Figure 4.8. The measurement is performed on a short piece of ECS nanowire attached on tapered fiber which delivers the pump laser. Theoretically, the power factor is 3 when the pumping power is low since the green emission is the second-order upconversion effect. However in order to observe the green emission, enough Er ions must be pumped to the excited states, which decreases the power factor. The power factor is fitted as $m = 2.19$ at the pumping power 0.1 mW, which is roughly equal to the injection power in the decay measurement. Therefore, according to Equation 4.8, the absorption cross section is equal to $\sigma = \alpha/N = \alpha_{green}/(m\Gamma N)$.
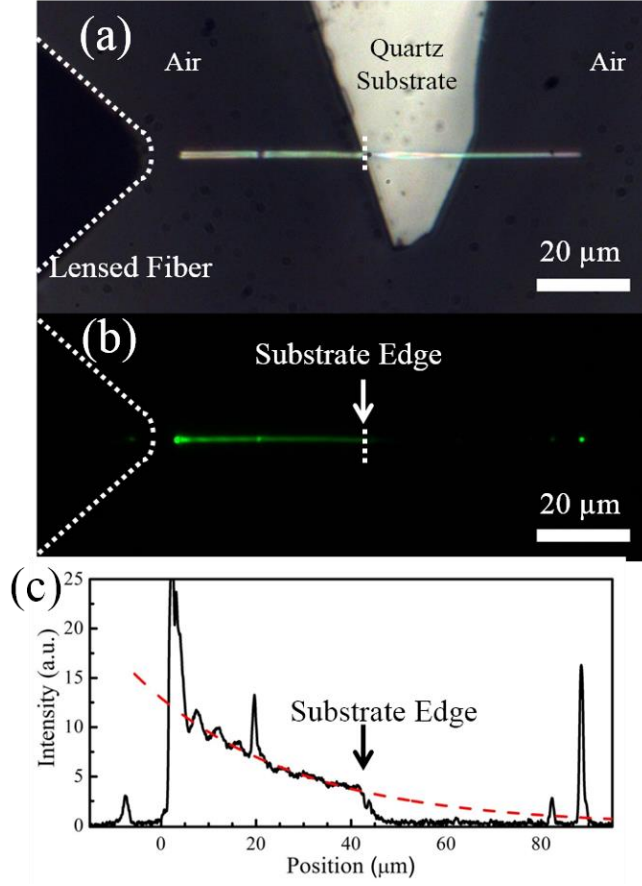
Figure 4.7 (a) Microscope top view of the ECS nanowire waveguide. (b) Image of the green upconversion from the ECS nanowire. (c) The integrated intensity of the green emission along the waveguide direction (solid black curve) and the exponential decay fitting of the suspending section (red dashed curve)

The gain confinement factor [93] in a 900 nm-diameter nanowire is $\Gamma = 1.04$ according to COMSOL simulation [94]. The Er concentration of the ECS is $1.62 \times 10^{22} cm^{-3}$. Thus, the absorption cross section is calculated as $\sigma_{abs} = 8.4 \times 10^{-21} cm^{-2}$, which is similar to the reported values of other Er materials listed in Table 4.2.
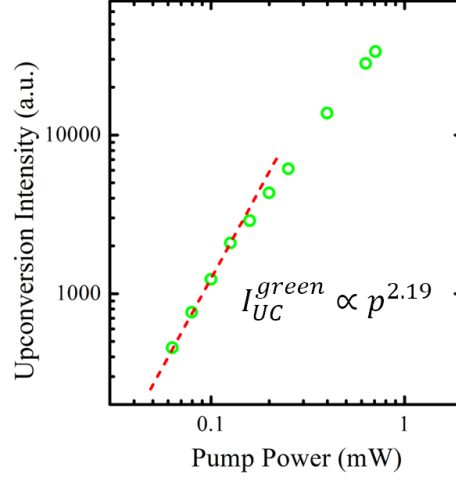
Figure 4.8 Power dependence of the green upconversion intensity with 1531 nm laser pumping.

Table 4.2 Absorption cross sections of ECS nanowires and other erbium materials from literature [14, 15, 37, 66, 95].

Ref.	Material (or host)	Crystalline type	Er concentration (cm^{-3})	Absorption cross section (cm-2)
This work	ECS	Single crystalline	1.62×10^{22}	8.4×10^{-21}
[15]	Phosphate	Amorphous	5.3×10^{20}	2.2×10^{-21}
[14]	Silicate	Amorphous	$3.9\text{-}6 \times 10^{20}$	5.8×10^{-21}
[95]	$GeO_2\text{-}SiO_2$	Amorphous	0.1×10^{20}	7.9×10^{-21}
[66]	Al_2O_3	Amorphous	2.7×10^{20}	5.8×10^{-21}
[37]	Er/Yb/Y silicate	Polycrystalline	2×10^{20}	9.0×10^{-21}

4.4 Net Gain in Single ECS Nanowire

In Chapter 4.2 and 4.3, we measured SE and absorption cross section from a single ECS nanowire. According to Equation 4.7, the net modal gain would be $g_{modal} = SE - \Gamma\sigma_{abs}N = 30 \; dB/cm$, much larger than the ever reported net gain in other Er material platforms, which is listed in Table 4.3.

Table 4.3 List of the reported net gain from literature [15, 20, 36, 37, 66, 96].

Ref.	Material (or host)	Crystalline type	Er concentration (cm^{-3})	Gain (dB/cm)
This work	ECS	Single crystalline	1.62×10^{22}	30
[15]	Phosphate	Amorphous	5.3×10^{20}	4.1
[20]	Phosphate	Amorphous	3.7×10^{20}	2.1
[66]	Al_2O_3	Amorphous	2.7×10^{20}	2.3
[96]	Silicon-rich-SiO2	Amorphous	1.7×10^{20}	2.7
[37]	Er/Yb/Y silicate	Polycrystalline	2×10^{20}	1.25
[36]	EYS	Polycrystalline	1.7×10^{20}	0.5

Two aspects are attributed to the reason of the large net gain in ECS nanowires. First is the large Er concentration, which is $1.62 \times 10^{22} cm^{-3}$, at least two orders of magnitude higher than the Er-doped materials. The high Er concentration provides the potential of large inverted population at the excited state, which enables the high gain. The second aspect is the long PL lifetime. Due to the concentration quenching effect, the lifetime of the Er-doped materials quickly decays when the Er concentration is higher than $10^{21} cm^{-3}$ [82], making the population inversion very difficult. This is one reason that why the net gain in the Er compounds with Er concentration higher than $10^{22} cm^{-3}$ has not been reported yet. As the discussion in Chapter 3.5, the high crystal quality of ECS nanowires reduces the concentration quenching effect, resulting the highest lifetime in the Er materials with similar Er concentration [16, 65, 86-88].

4.5 Population Inversion and Cooperative Upconversion Analysis

To study the power-dependent net gain and population inversion of the ECS nanowire waveguide, a three-level model including the cooperative upconversion is used to simulate the signal enhancement in single ECS nanowire. As shown in Figure 4.9, three states $^4I_{15/2}$, $^4I_{13/2}$, $^4I_{11/2}$ are involved in this process. The population at these three states are N_1, N_2, N_3 respectively. 980 nm laser pump excites the Er^{3+} ions from the ground state $^4I_{15/2}$ to the second excited state $^4I_{11/2}$ with pumping rate of $R_{13} = \phi_p \sigma_p N_1$, where ϕ_p is the pumping flux and σ_p is the absorption cross section at 980 nm. The Er ions at $^4I_{11/2}$ quickly decays to $^4I_{13/2}$ with transition rate of $W_{32} = N_3/\tau_3$. The lifetime τ_3 is roughly 10 μs [4, 41], much shorter than the lifetime of state $^4I_{13/2}$ (540 μs) . Thus, the Er ions can accumulate at the metastable state $^4I_{13/2}$, making the population inversion possible. There are several transitions from $^4I_{13/2}$ to $^4I_{15/2}$. One is the spontaneous decay, including radiative and non-radiative processes. The decay rate is $\beta_{sp} = N_2/\tau_2$, where $\tau_2 = 0.54\ ms$ is the lifetime of the metastable state. Another transition is the stimulated emission, with transition rate $\beta_{st} = \phi_s(\sigma_{em} N_2 - \sigma_{abs} N_1)$. ϕ_s is the photon flux of the 1.531 μm probe signal in the waveguide. σ_{em} and σ_{abs} are the emission and absorption cross sections between $^4I_{13/2}$ and $^4I_{15/2}$. Since the probe signal wavelength at 1.531 μm matches with the transition between the two lowest levels of the Stark splitting in $^4I_{13/2}$ and $^4I_{15/2}$ (see the discussion in Chapter 3.1), according to McCumber theory, the emission cross section and absorption cross section are almost equal at this wavelength [12, 14, 41, 95, 97], which is $0.84 \times 10^{-20}cm^{-2}$. The first-order cooperative upconversion is considered in this three-level model. The energy transferring between two ions at the metastable state $^4I_{13/2}$ makes one ion be excited to the higher state, the other ion decay to the ground state. Due to the short

lifetime of the higher state, the excited ion quickly decays to ${}^4I_{11/2}$. Since two ions are involved, the up- and down- conversion rates are quadratic to the population N_2, which is equal to $W_{CUC}N_2^2$. W_{CUC} is the cooperative upconversion coefficient. According to the discussion in Chapter 1.5.1, the excited state absorption can be neglected since the 980 nm pumping does match the absorption from ${}^4I_{13/2}$ to any higher state.
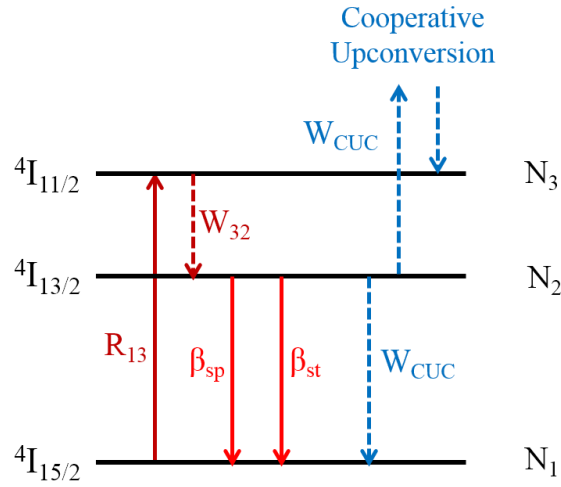
Figure 4.9 Energy level diagram showing the transitions in 3-level model.

The rate equations of the three-level system are listed below,

$$\frac{dN_1}{dt} = -\phi_p \sigma_p N_1 + \phi_s (\sigma_{em} N_2 - \sigma_{abs} N_1) + \frac{N_2}{\tau_2} + W_{CUC}N_2^2 \qquad (4.11)$$

$$\frac{dN_2}{dt} = -\phi_s (\sigma_{em} N_2 - \sigma_{abs} N_1) - \frac{N_2}{\tau_2} + \frac{N_3}{\tau_3} - 2W_{CUC}N_2^2 \qquad (4.12)$$

$$\frac{dN_3}{dt} = \phi_p \sigma_p N_1 - \frac{N_3}{\tau_3} + W_{CUC}N_2^2 \qquad (4.13)$$

$$N_1 + N_2 + N_3 = N \qquad (4.14)$$

At steady state condition, the time differential terms dN_i/dt are zero. From Equation 4.13 and 4.14, one can obtain

$$N_1 = \frac{N - N_2 - W_{CUC}\tau_3 N_2^2}{\phi_p \sigma_p \tau_3 + 1} \tag{4.15}$$

By Equation 4.15 and 4.11, the population N_2 can be solved as

$$N_2 = \frac{-B + \sqrt{B^2 - 4AC}}{2A} \tag{4.16}$$

where

$$A = \frac{\phi_p \sigma_p + \phi_s \sigma_{abs}}{\phi_p \sigma_p \tau_3 + 1} W_{CUC}\tau_3 + W_{CU}C \tag{4.17}$$

$$B = \frac{\phi_p \sigma_p + \phi_s \sigma_{abs}}{\phi_p \sigma_p \tau_3 + 1} + \phi_s \sigma_{em} + \frac{1}{\tau_2} \tag{4.18}$$

$$C = -\frac{\phi_p \sigma_p + \phi_s \sigma_{abs}}{\phi_p \sigma_p \tau_3 + 1} \tag{4.19}$$

In the nanowire waveguide, the pumping intensity and probe intensity are not uniform, due to the gain and absorption. The photon fluxes of pump and probe obey the following equations,

$$\phi_p(z + \Delta z) = \phi_p(z)e^{\Gamma_p(\sigma_p N_1(z) - \alpha_w)\Delta z} \tag{4.20}$$

$$\phi_s(z + \Delta z) = \phi_s(z)e^{\Gamma_s(\sigma_{em}N_2(z) - \sigma_{abs}N_1(z) - \alpha_w)\Delta z} \tag{4.21}$$

For ECS nanowire waveguide, the confinement factor is roughly 1 and the propagation loss can be neglected according to the discussion in Chapter 4.2 and 4.3. Therefore, the SE in ECS nanowire can be calculated with the giving pumping flux. In Chapter 4.2 and 4.3, 7 dB SE and 0.33 dB net gain was demonstrated in a 109 µm-long ECS nanowire. The simulation of the SE versus pumping curve in this nanowire is shown in Figure 4.10, while the circles are the experimental data from Figure 4.4(a) and the red curve is the simulation by three-level model.

The cooperative upconversion coefficient (CUC) is fitted in this simulation, as $W_{CUC} = 1.4 \times 10^{-18} cm^3 s^{-1}$. The CUCs reported in literature are listed in Table 4.4. The CUC of ECS nanowire is comparable to the Er materials with Er-concentration around 10^{20} cm^{-3}, but the CUCs of the Er compounds with Er-concentration above 10^{22} cm^{-3} are 2 orders of magnitude higher. This is the reason why the net gain have not been achieved in the high Er-concentration Er compounds such as erbium silicate. The relatively low CUC in ECS nanowire is attributed to the high crystal quality. The possibility of the erbium clustering and crystal imperfection is reduced, significantly decreasing the concentration quenching effect.
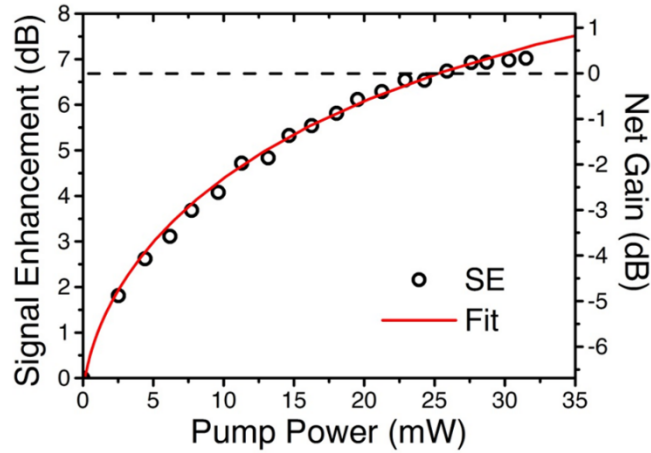
Figure 4.10 Fitting of SE with the 3-level model.

Table 4.4 List of the reported cooperative upconversion coefficient [15, 16, 36, 66, 89, 96, 98].

Ref.	Material (or host)	Crystalline type	Er concentration (cm^{-3})	Upconversion rate $(cm^3 s^{-1})$
This work	ECS	Single crystalline	1.62×10^{22}	1.4×10^{-18}
[15]	Phosphate	Amorphous	5.3×10^{20}	2×10^{-18}
[66]	Al_2O_3	Amorphous	2.7×10^{20}	4.1×10^{-18}
[16]	Sodium-silicate	Amorphous	1.7×10^{20}	3.2×10^{-18}
[36]	EYS	Polycrystalline	1.7×10^{20}	0.8×10^{-18}
[96]	Silicon-rich-SiO_2	Polycrystalline	1.7×10^{20}	2.1×10^{-18}
[98]	Er-Si-O	Polycrystalline	1×10^{22}	3.5×10^{-16}
[89]	Erbium silicate	Polycrystalline	2.7×10^{22}	5×10^{-16}

In the SE measurement, the 980 nm pumping was injected from the input end of the ECS nanowire. Due to the absorption, the pumping flux as well as the population inversion decay along the nanowire. Therefore, the peak gain happens at the input end of the nanowire, which should be higher than the average gain 30 dB/cm. To investigate the peak gain on the nanowire, it is necessary to calculate the spatial distribution of the population inversion. According to Equation 4.2, the material gain is equal to $g = \sigma_{em}N \times \frac{N_2 - \sigma_{abs}/\sigma_{em}N_1}{N}$. Because at the signal wavelength 1.531 μm, the absorption and emission cross sections are roughly equal [12, 14], the degree of population inversion can be defined as $D = (N_2 - N_1)/N$. Then the expression of net gain is simplified as $g = \sigma_{em}ND$. Without the pumping, all Er ions are at the ground state, giving $D = -1$. As the pumping is applied, D increases as well as the material absorbing decreases. The transparent point or the inversion point is at $D = 0$, where the material is transparent to the probe wavelength

without absorption and amplification. With further pumping, D is positive and the net gain is achieved. The material is fully inverted when $D = +1$.

The spatial distribution of the population inversion along the 109 μm ECS nanowire in Chapter 4.2 is simulated, as shown in Figure 4.11. The pumping power is assumed as 31.5 mW, which is the highest power during the experiment. The peak population inversion is 0.15 at the injection end and the population inversion decays along the nanowire to almost zero. Clearly this nanowire was not pumped enough. Although the population inversion cannot reach +1 due to the upconversion effect, the potential average gain of ECS nanowire can be much higher than only 30 dB/cm with higher pumping. This can also be concluded from the fitting of the power-dependent SE in Figure 4.10, that the SE is not saturated with the pump power. Therefore by further increasing the pumping power, higher net gain can be achieved. The currently demonstrated 30 dB/cm net gain is limited by the output power of our 980 nm laser and the pumping efficiency.

In Figure 4.11, the peak population inversion is D=0.15, corresponding to the peak net gain of 92 dB/cm. This is another evidence of the high potential gain in ECS nanowires. We believe that with higher 980 nm pumping power and more uniform pumping profile the ECS nanowire can achieve even higher net gain than the 30 dB/cm.
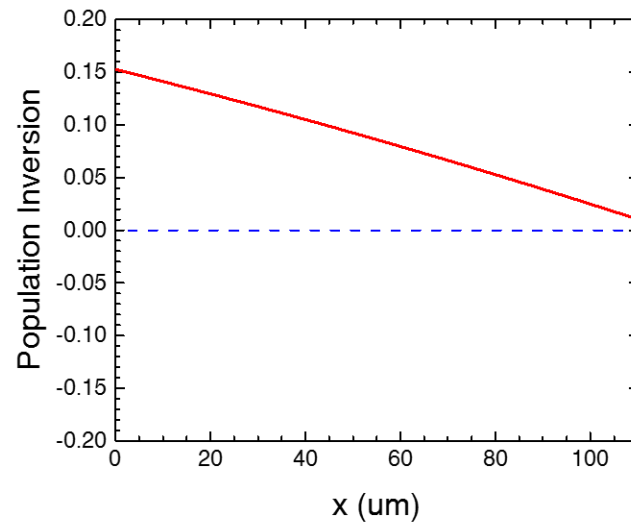
Figure 4.11 Population inversion along the ECS nanowire in the SE measurement with pumping power of 31.5 mW.

CHAPTER 5

DESIGN AND FABRICATION TOWARDS ECS NANOWIRE LASER

The photonic integrated circuit (PIC) is the device which integrates multiple photonic components including light sources, waveguides, modulators, sensors on a single chip [129]. Instead of the electrons in electric integrated circuit, the signals are processed by optical rays in PICs. The potential applications of PICs include photonic sensing, signal processing, imaging, on-chip spectroscopy, optical storage and logic [11]. The silicon-on-insulator (SOI) is one of the preferred platforms for PICs since the silicon processing techniques can be applied for the large scale integration [99]. One obstacle in the development of silicon-based PICs is the fabrication of the compact and silicon-compatible lasers at telecommunication wavelength. Since silicon is an indirect band gap semiconductor, it is hard to fabricate the silicon lasers using the traditional semiconductor laser techniques. The milestone of silicon laser is in 2005. H. Rong et. at. demonstrated the first silicon Raman laser under continuous-wave operation [100]. However, the gain in silicon Raman laser is low so it needs intensive optical pumping. The silicon-compatible lasers with higher power efficiency are still in demand. Recently the development of wafer-bonding technique provides the opportunity to fabricate electrical-driven III-V semiconductor lasers on silicon wafer [99, 101]. The processing includes the release of the III-V epitaxial layer, wafer-transferring and wafer-bonding techniques. The III-V epitaxial layer can be transferred to the silicon substrate for further laser processing. Nevertheless, the cost of the wafer-transferring and coupling efficiency from III-V lasers to silicon waveguides are still the issues.

Since the success of the first erbium-doped fiber lasers (EDFLs) in 1986 [7], the erbium-doped waveguide lasers (EDWLs) have been intensively studied as the low-cost and robust laser sources at 1.55 μm for PICs [12, 13, 102, 103]. However, according to the discussion in Chapter 1.1 and 4.4, the optical gain of erbium-doped materials is limited to several dB per centimeter due to the concentration quenching effect. As a result, long waveguides are required, making the device size larger. To further shrink down the laser size, the high-gain Er materials are in demand. In Chapter 4, the optical gain of ECS nanowires is demonstrated as 30 dB/cm, which is one order of magnitude higher than the reported gain in Er-doped materials. The one-dimensional (1D) nanowires are naturally waveguides which are compatible to on-chip integration. In addition, the ECS nanowires are potentially silicon-compatible because of the nanowires are grown on silicon substrate. Although in current stage the locations and orientations of the as-grown ECS nanowires are random, in principle the position of the nanowires can be controlled by pattern the Au catalyst on the silicon. Therefore, the ECS nanowire is a good candidate for the miniaturized lasers in silicon-based PICs.

Nanowire is a natural laser resonator confined by the end-facet. Lasing have been demonstrated on various semiconductor nanowires such as ZnO, GaN, CdS nanowires [56, 57, 104-107]. However, the optical gain in ECS nanowires is only 30 dB/cm, much lower the gain in semiconductors which is over 10^3 cm^{-1}. The low gain in ECS is not enough to compensate the mirror loss of the end-facets. A simple estimation shows that for a 100 μm-long ECS nanowire, the minimum threshold gain is 1200 dB/cm, which is impossible for ECS nanowires. To reduce the lasing threshold, it is necessary to fabricate a high quality factor (Q factor) resonator on the nanowire. There are several resonator designs for Er-

doped thin film, including distributed feedback grating, distributed Bragg reflector, ring cavity, micro-disk cavity and photonic crystal micro-cavity [38, 108-111]. Considering the 1D nanowire structure and the fabrication difficulties, two designs are discussed in this chapter towards a single ECS nanowire laser, including distributed feedback laser (Chapter 5.1) and 1D photonic crystal micro-cavity laser (Chapter 5.2 & 5.3).

5.1 Design and Fabrication of Distributed Feedback Laser on ECS Nanowire

The distributed feedback (DFB) laser is a laser containing periodic grating structure on the whole active region [112]. The periodic grating, which is called DFB grating, is a perfect reflector at certain wavelengths, forming the optical stop band (band gap). In the stop band, the DFB grating is total reflective. In the DFB laser, a phase shifter is typically inserted in the middle of the grating to create a high-Q mode in the band gap, allowing the single mode operation with ultra-low threshold. So it is possible to achieve lasing on the low gain materials [22, 113, 114].

The DFB laser based on single ECS nanowire is illustrated in Figure 5.1(a). 2N-periods DFB grating with period of Λ is etched on the top of the ECS nanowire. The thickness of the grating is much smaller than the diameter of the ECS nanowire to reduce the scattering loss. A phase shifter with the length equal to the period of the grating is designed in the middle of the DFB grating. When the wave-vector of the propagating mode in the nanowire waveguide matches with the period of the grating, the grating present strong reflectivity to this mode, as Bragg condition,

$$\Lambda = \frac{\lambda}{2n_{eff}} \tag{5.1}$$

where λ is the wavelength and n_{eff} is the effective index of this mode. The optical mode can be well confined in the cavity in the middle of the DFB grating. Q-factor is mainly dependent on the strength of the reflectors, which is sensitive to the length of the DFB gratings.
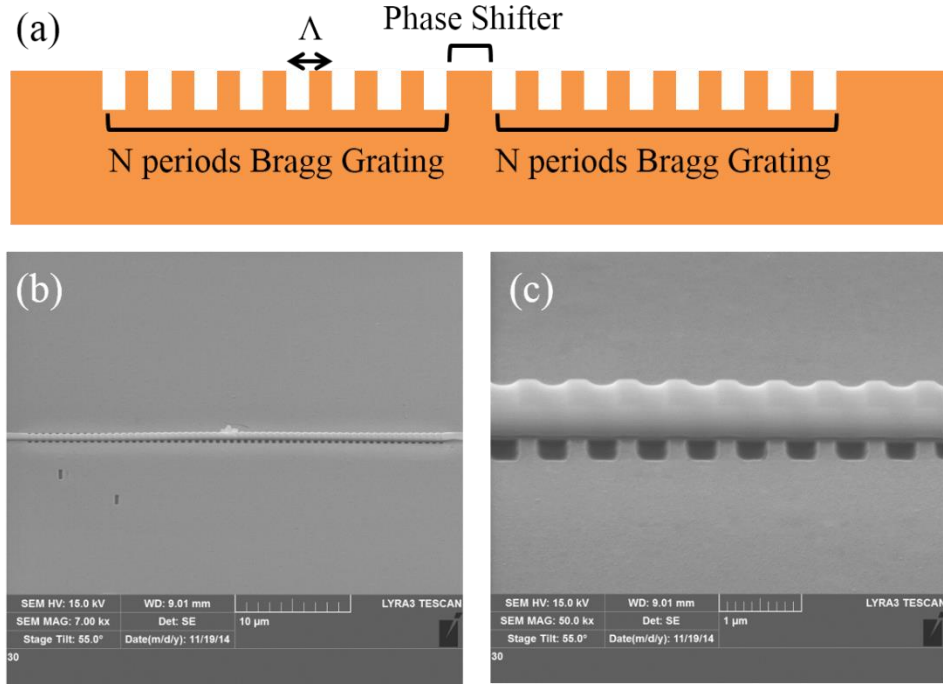
Figure 5.1 (a) Diagram of the DFB grating. (b,c) SEM image of the fabricated DFB grating on ECS nanowire.

The DFB structure is fabricated by focused ion beam (FIB) etching, as illustrated in Figure 5.1(b-c). The focused gallium ion beam physically hits the surface of the ECS nanowire and removes the materials at the etching region. Because the ECS nanowire is silicate material which is not well conductive, electrons can be charged on the surface of ECS nanowire, making the etching profile a sine wave shape rather than the sharp steps.

The side walls of the ECS nanowire are also slightly etched because the charged electrons attract the gallium ions to hit on the side walls.

Although the DFB laser is theoretically a high-Q cavity, practically there are several critical problems, making the ECS nanowire laser difficult.

1) The DFB grating is a weak-confinement structure, requiring a long length to enhance the grating strength. According to the simulation using transfer matrix method [112, 115], in order to achieve $Q>10^4$, the length of the DFB grating is required as $70 - 100$ μm, which is close to the maximum length of the ECS nanowires.

2) The long ECS nanowires are typically in tapered shape. Since the propagation constant of the mode is related to the diameter of the waveguide, it is difficult to design the period of the grating to match the propagation constant along all the grating region. Any mismatch will significantly reduce the Q.

3) Since the DFB grating must be long, the etching error is critical. However, the electron charging effect is serious during the FIB process, making the precise control of the lateral etching profile difficult. Any imperfection on the grating in such long length will completely ruin the laser.

So according to the reasons above, the DFB grating is not a good choice for the design of ECS nanowire laser. The key issue is that each period of the DFB grating is a weak reflector. Only when there is a large number of periods, the grating can be a good reflector. However, the imperfection of the ECS nanowire limits the fabrication region shorter than 50 μm. So we must design stronger reflectors with limited length to achieve the ECS nanowire laser.

70

5.2 Design and Fabrication of 1D Photonic Crystal on ECS Nanowire

Photonic crystal (PhC) refers to the structure with periodic dielectric constant distribution in certain directions. PhC is typically a thin film (2D) or a linear waveguide (1D) inserted with periodic air-holes or dielectric rods [116-125]. Similar to the DFB gratings, the uniform PhC grating represent the total reflective behavior when the wavelength matches with the Bloch mode, which is $\lambda = \Lambda/2n_{eff}$. Due to the large index contrast between the air-holes and the dielectric waveguide, the strength of the PhC as a total reflector is much stronger than the DFB grating. Therefore, it is possible to design an ultra-high Q micro-cavity with 1D PhC [118-122]. The 1D PhC micro-cavity with Q factor over 10^9 was demonstrated on a silicon nanobeam with total length less than 15 μm [122].

In Chapter 5.2.1, the fabrication of periodic 1D PhC on the ECS nanowire is presented. The refractive index of ECS material is first-time determined through the transmission spectroscopy. In Chapter 5.2.2, the 1D PhC micro-cavity with Q factor over 10^5 is designed by 3D finite-difference time-domain (FDTD) simulation. Such high-Q micro-cavity is expected to eventually achieve the ECS nanowire laser.

5.2.1 Fabrication of Uniform 1D PhC

The fabrication of uniform 1D PhC grating on single ECS nanowire is shown in Figure 5.2. An ECS nanowire of 590 nm in side length of cross section was transferred on a silicon wafer for FIB etching. In order to demonstrate the 1D PhC fabrication and determine the refractive index of this ECS material, we first etched a uniform hole array of 14 periods on a single ECS nanowire, as shown in Figure 5.2. The diameter of the air holes

and the period are 240 nm and 700 nm respectively. The total length of the fabricated 1D PhC structure is 9 μm. After the FIB etching, the nanowire was transferred on another silicon wafer with pre-etched trenches of 1 μm in depth, such that the segment with PhC structure is suspended in air with both ends placed on silicon, as shown in Figure 5.3.
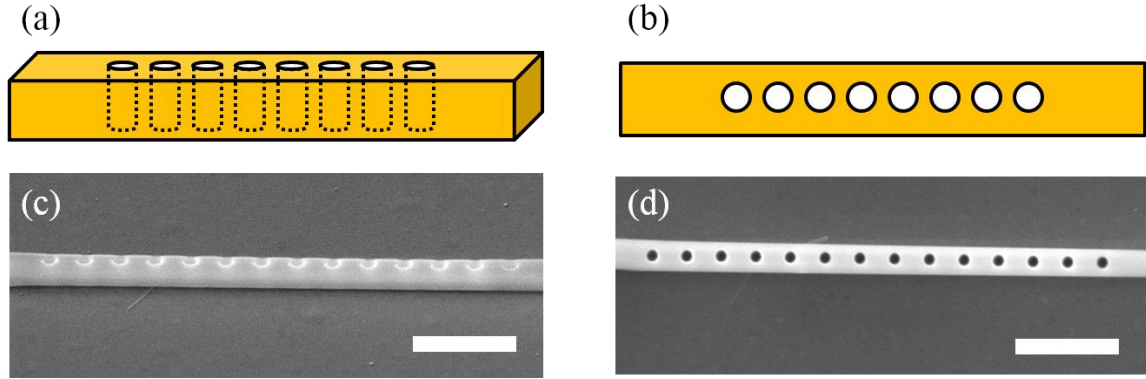
Figure 5.2 (a,b) Illustration of the 1D PhC structure in angled view and top view. (c,d) SEM images of the 14-period PhC grating in single ECS nanowire.
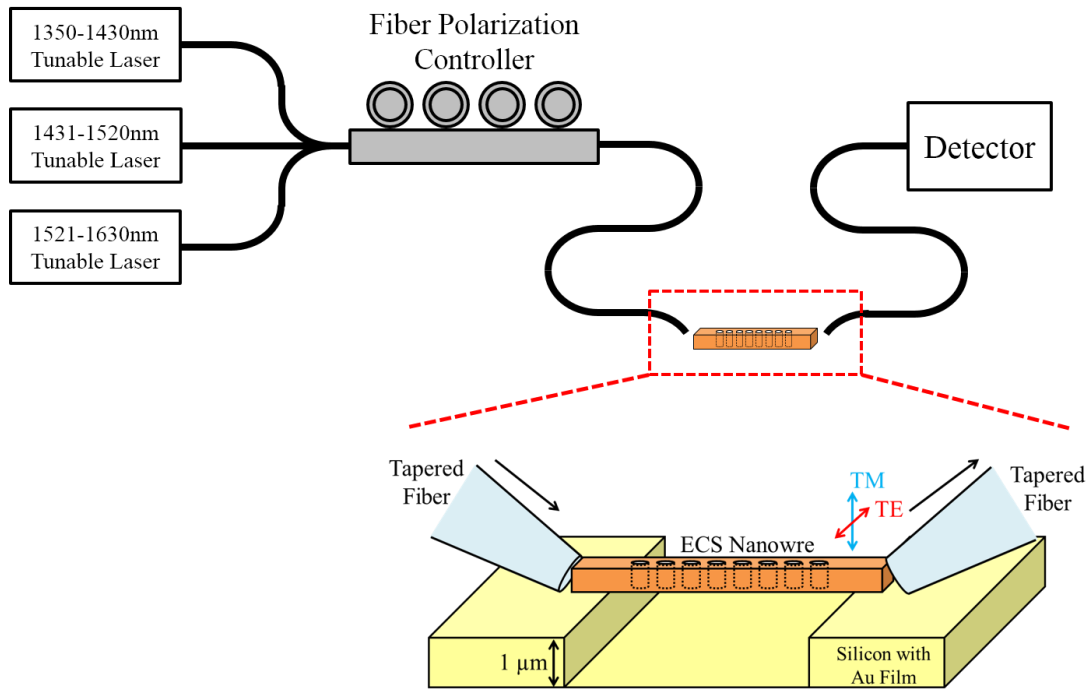
Figure 5.3 Configuration of the transmission spectroscopy setup.

To determine the stop band of this 1D PhC reflector, the transmission spectroscopy was performed, as shown in Figure 5.3. The input source was a bundle of three tunable lasers covering the wavelengths from 1350nm to 1630 nm. The input laser was coupled to the nanowire through a tapered fiber with tip size around 1 μm. The polarization of the input signal was precisely controlled by a motorized fiber polarization controller (Agilent, 11896A). The transmitted signal was connected to the power detector through another tapered fiber. The detail information of the fiber-nanowire coupling system can be found in Appendix A.

The etched ECS nanowire was transferred to a silicon substrate pre-etched with 1 μm-depth trench as shown in Figure 5.4(a, b). The PhC segment of the nanowire was suspended in air while the two ends were placed on the silicon. The suspended PhC region is in the symmetric refractive-index environment, which can maximize the strength of the PhC reflector. The silicon substrate was pre-sputtered with 30 nm Au film before the nanowire transferring for preventing the signal leaking from nanowire to silicon substrate.
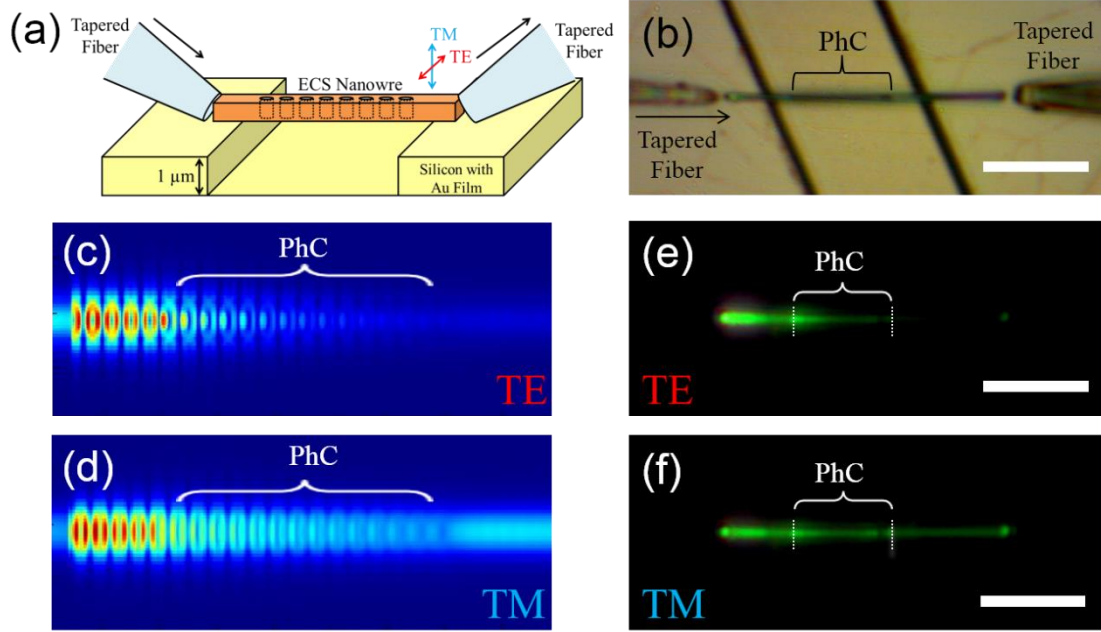
Figure 5.4 (a) Illustration of the fiber-nanowire-fiber coupling system. (b) Photo image of the coupling system from the top view. (c,d) FDTD simulation of the E-field pattern under TE- and TM- polarization injection. (e,f) Real-color image of the upconversion along the nanowire in (b) under TE- and TM- polarization injection at 1531 nm.

The polarization of the input laser was controlled in horizontal (TE) and vertical (TM) polarization, as shown in Figure 5.4(a). The strength of the PhC reflector is sensitive to the polarization of the signal. The reflectivity of the PhC grating reaches the maximum and minimum when the input signal is in TE and TM polarization respectively. As a result, for the wavelength at the center of the stop band, the transmitted signal in TE polarization is much weaker than the signal in TM polarization. The 3D FDTD simulations of the signal distribution along the nanowire in TE and TM polarization are shown in Figure 5.4(c, d) respectively. Clearly in TE polarization the signal decay much quicker than the TM polarization situation.

Experimentally, it is difficult to calibrate the polarization at the output of the tapered fiber because the polarization is always shifting with even a slight change of the fiber curvature. So the TE and TM polarization was determined by the minimum and maximum transmission at the center wavelength of the stop band, as the discussion above. Figure 5.4(e, f) shows the upconversion images under TE and TM injection at 1531 nm which is close to the center wavelength of the stop band. Clearly the green upconversion decays much quicker in TE polarization than in TM polarization, which agrees with the FDTD simulation in Figure 5.4(c, d).

It is important to point out that the green upconversion at the PhC region does not show significant degradation, indicating that the emission efficiency of ECS nanowire is not significantly degraded after the ion beam etching, unlike semiconductors and organic materials which are sensitive to ion damaging and impurity injection. This is critical for the laser fabrication.

The transmission spectra under TE and TM polarization is shown in Figure 5.5. Clear stop-band behavior with more than 12 dB suppression was observed at 1.525 μm for the TE polarization, while the suppression is much lower in the TM polarization. The FDTD simulation of the transmission spectra in TE and TM polarization is shown as the dashed lines in Figure 5.5. The simulated transmission spectra are well matched with the experimental results. The refractive index of ECS material is fitted as n=1.64, which is close to the reported value of erbium silicate thin film [12, 81].
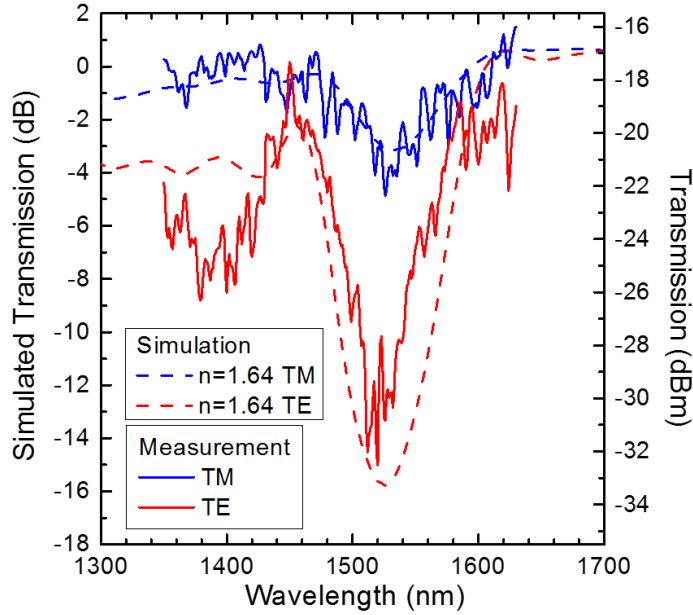
Figure 5.5 Experimental (solid) and simulated transmission spectra unter TE- (red) and TM- (blue) polarization injection. The refractive index of the FDTD simulation is set as n=1.64.

5.2.2 Design of 1D PhC Micro-cavity

Based on the refractive index of the ECS nanowire, we can design the ultra-high Q PhC micro-cavity at the desired wavelength. To understand the design of the 1D PhC micro-cavity, we consider the micro-cavity is confined by two PhC gratings with uniform hole size as the Bragg mirrors (see Figure 5.6). Although the PhC gratings can be treated as the total reflector, there is still considerable scattering loss from cavity to PhC grating due to the mismatch of the impedance between the waveguide mode in cavity and Bloch mode in PhC gratings [121, 126, 127]. One effective way to reduce the scattering loss is tapering both hole size and hole spacing towards the cavity [118-121, 126]. It is

76

demonstrated that the 4 − 7 periods of linear tapering profile can significantly reduce the loss and enhance the Q factor [118-121]. The quadratic tapering profile is reported to have better performance than the linear tapering profile [122, 127]. But for simplifying the calculation, the following PhC micro-cavity design still uses the linear tapering profile. To further minimize the cavity loss, the cavity length is also optimized. It is reported that the optimized cavity length which is the distance between the two PhC gratings should be zero [121, 122].
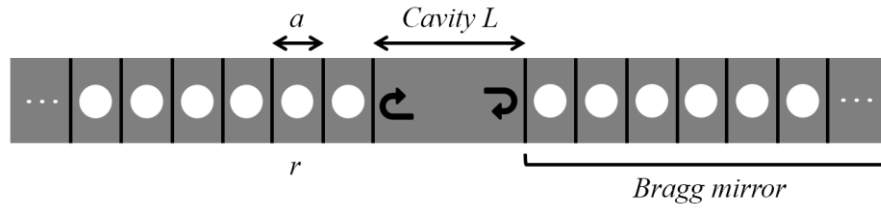
Figure 5.6 Micro-cavity confined by a pair of uniform 1D PhC grating.

Because the refractive index of ECS nanowire (n=1.64) is much lower than the index of silicon (n=3.4), the strength of PhC reflector in ECS nanowire is much lower than in silicon waveguides. To avoid elongating the total length of the PhC grating, the common method to design the high Q cavity in low index materials is using the elliptical holes instead of the circular holes, since the elliptical shape of the air-hole can increase the filling factor of the holes, which enhances the strength of the grating [111, 128].

According to the above discussion, the high Q PhC micro-cavity is designed as shown in Figure 5.7 with the following criteria [118-122]:

1. The micro-cavity is confined by a pair of PhC gratings

2. Each PhC grating contains n_{Bragg} period of grids with uniform period as the Bragg reflector and n_{taper} period of grids with linearly tapered period towards the micro-cavity.

3. The wave vector of the Bloch mode in the most inner period matches with the wave vector of the cavity mode.

4. An elliptical nanohole with fixed aspect ratio is etched in the center of the each grid. The major axis of the elliptical hole is perpendicular to the grating direction.

5. The minor radius of the nanohole is proportional to the width of each grid, which is $r_i = \gamma a_i$, γ is constant. So the size of the nanoholes also tapers towards to the micro-cavity.

6. The cavity length which is the distance between the two most inner grids is $\Delta L = 0$.
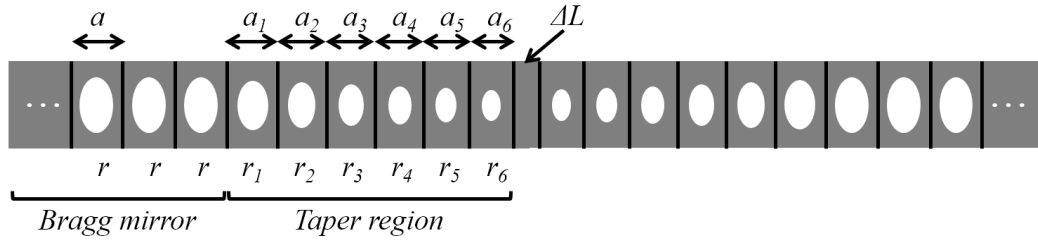
Figure 5.7 Design of the 1D PhC micro-cavity with tapered grating.

The 1D PhC micro-cavity laser is designed according to the above criteria on the ECS nanowire with diameter of 1 μm. The parameters of PhC grating are shown in Table 5.1. The total length of the PhC structure is 24 μm. The 3D FDTD simulation of the fundamental mode is shown in Figure 5.8. The Q factor is 1.2×10^5 at 1.531 μm and the

mode volume is V = 2.08 $(\lambda/n)^3$. The Q factor is one order of magnitude higher than the required Q for the ECS nanowire laser with 30 dB/cm net gain. Therefore, even considering some fabrication imperfection of the PhC structure, it is still possible to achieve lasing on a single ECS nanowire. In addition, the lasing mode in the PhC micro-cavity is mostly confined in the middle region of the PhC. For the laser operation, only a small region (<5μm) needs to be pumped over the transparent threshold. Therefore, it is easier to achieve population inversion as well as net gain in such small cavity than pumping the whole nanowire such as the DFB laser.

Table 5.1 Structure parameters of the designed 1D PhC micro-cavity on an ECS nanowire with diameter of 1 μm. The Q factor of the fundamental mode in this micro-cavity is 1.2×10^5.

Structure Parameters	Value	Structure Parameters	Value
Width	1000 nm	*Height*	1000 nm
a	637 nm	r	185 nm
a_1	621 nm	r_1	180 nm
a_2	605 nm	r_2	175 nm
a_3	589 nm	r_3	171 nm
a_4	573 nm	r_4	166 nm
a_5	557 nm	r_5	162 nm
a_6	541 nm	r_6	157 nm
ΔL	0 nm	*AR*	2
n_{Bragg}	12	n_{taper}	6

79
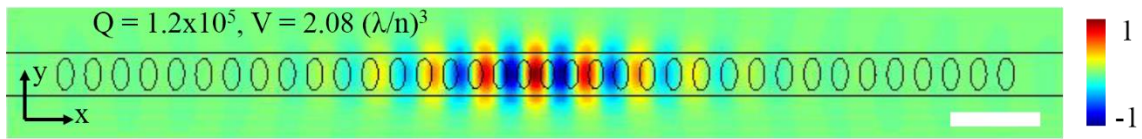
Figure 5.8 E-field (E$_y$) profile of the fundamental mode in the micro-cavity designed in Table 5.1. The scale bar is 2 μm.

The FIB fabrication of the PhC micro-cavity is still under optimization. One fabrication example of the micro-cavity structure is shown in Figure 5.9. We believe the ultra-high Q micro-cavity towards the laser can eventually be fabricated on the ECS nanowires.
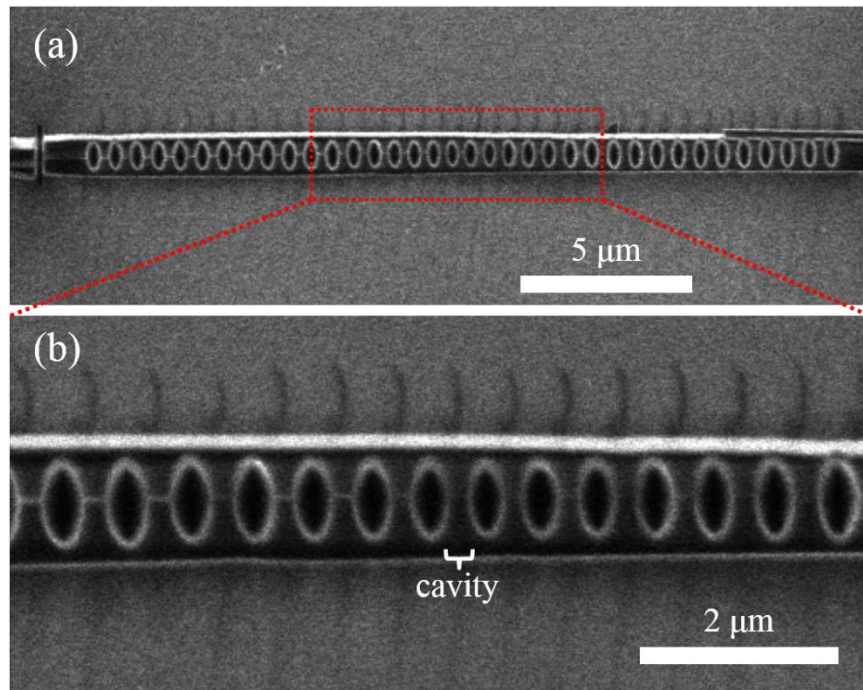
Figure 5.9 SEM images of the fabricated 1D PhC micro-cavity on an ECS nanowire with diameter of 1.1 μm.

5.3 Conclusions

Erbium chloride silicate, a new Er-compound material in 1D nanowire form, has been thoroughly studied in this part. The ECS nanowires are grown on silicon substrate via

CVD approach. The XRD characterization illustrates that the ECS nanowires have orthorhombic crystalline structure with Er concentration of 1.62 x 10^{22} cm^{-3}, which is 100-times higher than the Er-doped materials. Attributed to the VLS growth mechanism, the ECS nanowires are high-quality single crystal with growth direction in [060] which is demonstrated by TEM analysis. Such high crystal quality significantly decreases the possibility of the Er clustering, reducing the concentration quenching effect. The time-resolved PL measurement illustrates the lifetime of ECS nanowires as 0.54 ms, which is much longer than the Er materials with Er concentration over 10^{22} cm^{-3}. The long lifetime of ECS nanowires enables enough population inversion for achieving the optical gain.

The internal net gain of an optical amplifier can be calibrated by the pumping-induced signal enhancement and the zero-pumping absorption in the amplifier. However, neither SE nor absorption is easy to be measured since many traditional testing techniques are not applicable to the nanowires. In this work, the fiber-nanowire-fiber coupling technique is developed for measuring the SE, that 644 dB/cm SE is demonstrated in a single ECS nanowire. Such SE is one order of magnitude higher than reported values in Er-doped materials. The absorption coefficient is obtained from the decay rate of the green upconversion and the power-dependent relationship between the pumping and the green emission. The absorption cross section is calculated as 8.4 x 10^{-21} cm^{-2}, which is at the similar level as the Er-doped materials. By combining the experimental results of SE and absorption, 30 dB/cm net gain is demonstrated in a single ECS nanowire, higher than ever reported gain of Er materials. Even higher peak gain is illustrated by analyzing the spatial distribution of the population inversion on the nanowire.

Besides the gain measurements, other optical properties of the ECS nanowires are analyzed, including high-resolution PL spectroscopy, power- and temperature- dependent PL spectroscopy, and emission linewidth analysis. The detailed energy splitting due to the Stark effect is determined by the high-resolution PL spectrum. The temperature-dependent PL measurement illustrates the thermal stability of the ECS nanowires in a wide temperature range. The temperature-dependent emission linewidth is also studied. The narrow linewidth at both low temperature and room temperature demonstrate the high crystal quality of ECS nanowires.

Because of high optical gain and silicon-based synthesis process, ECS nanowires are expected to be potential laser sources for silicon-based photonic integrated circuits. In this work, simulation and fabrication towards a single ECS nanowire laser are researched. In order to achieve the lasing, the optical mode must be confined in a low-threshold cavity. Therefore, two on-nanowire high-Q structures are proposed: the DFB grating and the 1D PhC micro-cavity. Simulation illustrates that the DFB grating is a weak-confinement structure, thus requiring a long nanowire for lasing. Due to the growth and etching imperfections in such long nanowire, the DFB laser on single ECS nanowire is difficult. Nevertheless, the 1D PhC micro-cavity is demonstrated as a feasible high-Q structure due to its strong confinement. The transmission spectroscopy of the ECS nanowire etched with uniform 1D PhC grating demonstrates the strong grating reflection, low scattering loss, and feasibility of the FIB fabrication. The exact refractive index of ECS is first determined by FDTD simulation of the transmission spectra. Finally, an ultra-high Q PhC micro-cavity is designed based on the optical and structural properties of the ECS nanowire. The total

length of the PhC is smaller than 25 μm, showing the prospect of the ultra-compact and silicon-compatible laser devices for photonic integrated circuits.

CHAPTER 6

DESIGN OF A TWO-COLOR AND COLOR-CONTROLLABLE LASER

6.1 Introduction

Multi-color laser sources are important in many aspects of technology and daily life especially color display [129] and general lighting [130]. One important advantage of multi-color lasers for color display is the larger available color range, or color gamut, compared to the existing display technologies based on incoherent sources, such as cathode ray tubes, cold cathode fluorescent lamps and RGB light emitting diodes (LED). The large spectral linewidth of incoherent light sources degrades the color purity and leads to a small color gamut [131, 132]. As coherent light sources, multi-color lasers render high purity monochromic colors and thus extend the color range significantly. More saturated and vivid colors can be achieved with the extended color gamut. For lighting or illumination applications, multi-color lasers offer much higher power efficiency [133-135] than incoherent LED and fluorescent sources. The recent research [130] shows that the combination of four separate lasers with specifically selected wavelengths can achieve high color rendering ability [129, 136] as white LEDs or fluorescent lamps. The high color rendering indicates that various objects under the multi-color laser illumination reveal the similar colors as when they are under natural light illumination such as sunshine. Therefore, the laser illumination is a practical and power saving technique.

While the importance of multi-color lasers and dynamical color control have been well-recognized for a long time, the realization of such sources in monolithic structures has been challenging due to several technology issues. Different from the multi-mode lasers,

which limit the wavelength separation in the gain bandwidth of a semiconductor [137], the multi-color lasers require the gain materials emitting wide-range wavelengths, such as semiconductor alloys of different alloy compositions [138, 139]. Thus, the integration or monolithic growth of multiple gain materials are necessary. Due to the large lattice mismatch, it is challenge for the epitaxial growth of the semiconductors with different bandgap on one substrate. Another challenge is the laser cavity design. When multiple gain materials are involved in a monolithic integrated structure, the light emitted by the wide-gap materials will be absorbed by the narrow-gap materials. Therefore, lasing can only be achieved in the longer wavelength of the structures. Innovative ideas and designs are needed to achieve multi-color lasing.

In the past decades, various small-size multi-color light sources based on nanowires [140, 141], quantum dots [142-144], and microfluidic droplet dye-lasers [145-147] have been demonstrated. However, in most of these designs, the multi-color lasers were obtained by combining several single-wavelength lasers with additional waveguides to guide and mix the multicolor emissions [141, 145-147], which inevitably increases the dimension of devices and the cost of technology. Recently, spontaneous emission of the colors covering the entire visible range was demonstrated from different sections of a single ZnCdSSe alloy nanowire [148]. In 2012, two-color lasing from a single nanosheet was demonstrated [149]. Multi-color emission and lasing were also demonstrated on a single substrate where different nanowires with different alloy compositions graded along the substrate show different emission colors [138, 139, 150, 151]. However, despite such progresses, multi-color lasing with dynamical color control is still challenging.

In this work, these challenges are resolved by using a novel combination of gain materials and cavity design to demonstrate simultaneous lasing at green and red colors from a single CdSSe alloy nanowire. The CdSSe alloy nanowire has purposely engineered alloy composition variation along the axial direction of the nanowire [152]. The continuously tuned alloy composition along the nanowire allows the bandgap variation in a wide range, which makes the lasing at two distinct colors possible. In addition, the high quality of semiconductor crystal along all the alloy nanowire can be achieved due to the gradual composition change. By looping the wide-gap end of the nanowire, two weakly coupled cavities are created. Then, the green and red lasing modes are separated in two cavities respectively. The absorption of the short wavelength light in the narrow-gap section is minimized, which enables modes at both colors to lase simultaneously. Therefore, the fundamental challenges of material and cavity structure are solved at the same time. The two-color lasing with wavelength separation of 107 nm was demonstrated, which is much larger than the gain spectra of typical semiconductor materials [153-157]. Since the two-color lasing shares the output port, the color of the total laser output can be controlled dynamically between the two fundamental colors by changing the relative pumping power of the two segments, which leads to the laser generation of any color between the two fundamental colors according to the color map of International Commission on Illumination (CIE).

6.2 Composition-graded CdSSe Alloy Nanowires

The composition-graded CdSSe alloy nanowires are grown by Nanophotonics group in State Key Laboratory of Modern Optical Instrumentation at Zhejiang University,

China. The growth of such nanowires is reported in [152]. The alloy nanowires were grown on silicon substrate through a two-step CVD approach. In the first step, only CdS source was placed in the heating zone of the tube furnace for the initial CdS nanowire growth. After 40 minutes, the CdSe source was slowly introduced to the heating zone. Meanwhile, the temperature of the furnace was slowly reduced with a rate of 0.5 °C/min from 830 °C to 800 °C and kept at 800 °C for one hour growth.

The length of the alloy nanowires can be up to 200 μm. The diameter is typically between 200 nm and 300 nm. The cadmium composition of CdS_xSe_{1-x} alloy varies continuously from x=1 to x=0 along the nanowire, corresponding to the emission wavelengths from 505 nm (green) to 710 nm (red). In the sample received from our collaborator, the composition range of most alloy nanowires is a little bit smaller, giving the emission wavelength from 505 nm to 650 nm. Figure 6.1 shows an example of the composition-graded CdSSe alloy nanowire. The real-color PL imaging was performed and illustrated in Figure 6.1(a). The nanowire was pumped by a 405 nm continuous-wave (CW) laser. The emission color continuously varies from green to red along the axial direction of the nanowire. Figure 6.1(b) shows the spatially resolved PL spectra through scanning a localized pumping along the nanowire. The pumping beam is focused to the spot size around 10 − 15 μm. The emission wavelengths continuously varies from 540 nm to 610 nm. Because the large pumping spot size and continuously changing of the composition on the nanowire, at each pumping position, more than a single composition was pumped. Therefore, the PL emission linewidth is more than 30 nm which is wider than the linewidth of a single composition CdSSe alloy (around 10 − 20 nm), and the wavelength range is narrower than we expected.
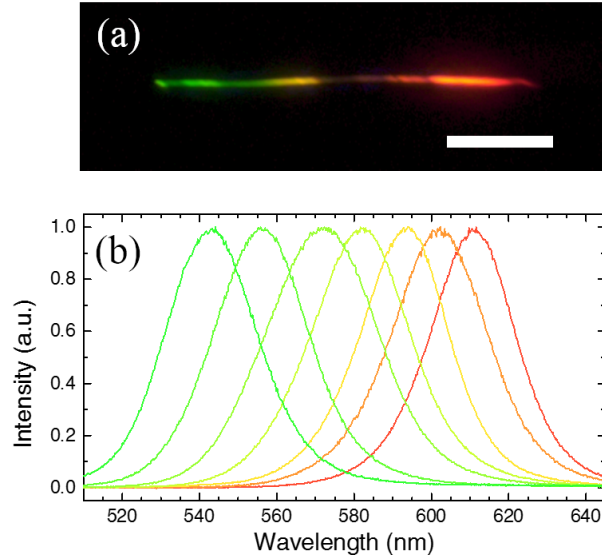
Figure 6.1 (a) Real color PL image of a CdSSe alloy nanowire. Scale bar is 20 μm. (b) PL spectra from this nanowire with localized pumping at 7 points along the nanowire. The pumping spot size is around 10 – 15 μm.

6.3 Looped Alloy Nanowire for Color-controllable Lasing

Although the alloy nanowire contains the gain materials with a wide range of bandgap energy, it is not possible to directly achieve the multi-color lasing in such nanowire without any manipulation. As shown in Figure 6.2(a), because the wide-gap (CdS-rich) segment is transparent to the red light emitted by the CdSe-rich part, red emission can easily reach the threshold and start lasing. However, the short wavelength (green) emission from the CdS-rich section will experience a strong absorption in the narrow-gap (CdSe-rich) section. Thus, green lasing becomes nearly impossible without an extremely long segment. In order to achieve simultaneous lasing at both long and short wavelengths, light emitted from the wide-gap region needs to be well-confined within its own segment. Therefore, an individual cavity is necessary for separating the green

88

emission from the narrow-gap materials. One convenient, but critical method to create distinct cavities in a single nanowire structure is to loop the wide-gap section, which forms a relatively isolated cavity for the green emission as illustrated by Figure 6.2(b). The junction coupling efficiency of such a ring cavity is very high [158-160], providing strong feedback for the green lasing. The lasing mode of green emission is isolated in the ring cavity, which avoids the strong absorption in the straight part with narrow-gap materials. As a result, the green modes oscillating in the ring cavity have enough gain and low loss to achieve lasing. At the same time, the red emission from the narrow-gap section can still propagate in the entire nanowire with a cavity defined by two end-facets.

The unique feature of this looped-cavity design allows the dynamical tuning of the output color. Figure 6.2(c) shows the concept of color-tunable lasing in the looped CdSSe alloy nanowire. The excitation laser output is split into two beams to pump the green looped section and red straight section separately, which allows the control of the relative lasing intensities from each section by changing its corresponding pumping strength. As a result, the overall laser output from the looped nanowire would continuously change color from green to red corresponding to the change in relative mixture of the two fundamental colors.
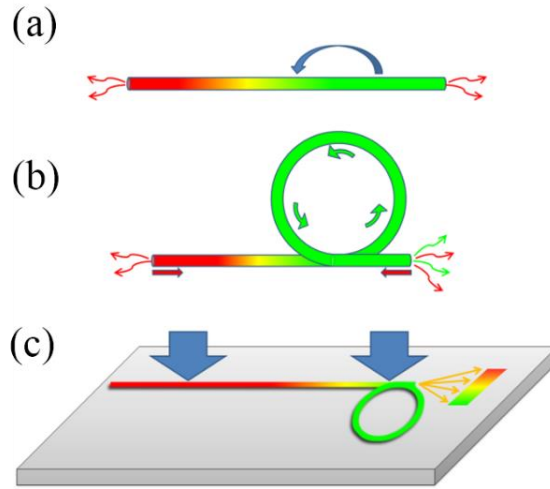
Figure 6.2 (a) Sketch of straight CdSSe alloy nanowire, which supports only red lasing. The color variation along the wire represents the continuously changing composition. (b) Sketch of the looped nanowire, which supports both green and red lasing. (c) Design of the color-tunable laser using this looped nanowire by changing the relative strengths of pumping of the two segments, indicated by the two blue arrows. The total output color at the loop junction can change from red to green continuously.

6.4 Optical Modes in Straight and Looped Nanowire

To further explain the modal confinement and feedback mechanism in looped alloy nanowire, the mode analysis for both straight and looped nanowires were performed using COMSOL software [94]. The mode simulation in a straight wire is shown in Figure 6.3. To simply the simulation, it is assumed that the alloy nanowire consists of two equal length of pure-CdS and pure-CdSe sections. The total length of this nanowire is 10 μm and the width is 250 nm. The refractive indices of CdS and CdSe are 2.60 and 2.56 respectively. A typical example of the mode pattern in the straight nanowire is shown in Figure 6.3(b). The mode is propagating along the length direction of the nanowire. Since the difference

between the refractive indices of CdS and CdSe is small, the E-field of the mode is almost uniformly distributed in the entire nanowire.
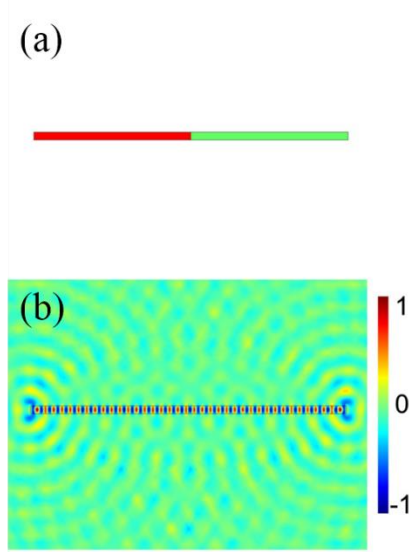
Figure 6.3 (a) Schematic of the straight nanowire structure, where green and red colors indicate the wide-gap (CdS or CdS-rich) and narrow-gap (CdSe or CdSe-rich) sections respectively. (b) E-field pattern of the optical mode in straight nanowire.

Since the CdS section is nearly transparent to the red emission from CdSe section, in order to achieve the red color lasing, the threshold gain in CdSe only needs to compensate the mirror loss from the two ends of the nanowire which is around 1000 cm^{-1} according to the length of the CdSe gain region. Therefore, the red color lasing is possible in the mode shown in Figure 6.3(b). However, the green emission from CdS section meets a huge absorption when it propagates to the CdSe section, which is a narrow-gap material. The lasing condition of the green emission is expressed as Equation 6.1.

$$\frac{1}{L}(L_1 g_{th} - L_2 \alpha_{CdSe}) = \alpha_m \qquad (6.1)$$

L_1, L_2, L are the length of CdS section, the length of CdSe section and total length respectively. g_{th}, α_{CdSe} and α_m are threshold gain, absorption loss in CdSe section and total mirror loss respectively. In order to achieve net average gain on the entire nanowire, the left part in Equation 6.1 must be positive. The maximum gain of CdS under reasonable pumping is typically 2000 cm^{-1}, however, the absorption of the CdSe section is over 20000 cm-1 (the gain and absorption calculation can be found in Chapter 6.5). Therefore, the length of the CdS section must be at least 10 times longer than the CdSe for achieving the green lasing in a straight alloy nanowire. This is impossible in a uniformly composition-graded alloy nanowire. Even the alloy nanowires with much longer CdS section can be grown, the green lasing is extremely inefficient because of the huge absorption. The detail discussion of the average gain in a straight alloy nanowire with uniform composition grading can be found in Chapter 6.5.

In order to achieve efficient lasing at green wavelengths, it is desired to isolate the green mode in the wide-gap (CdS or CdS-rich) section, with minimal leakage into the narrow-gap (CdSe or CdSe-rich) section to minimize absorption. One effective method is to loop the wide-gap end, forming a ring feedback for the green mode. Figure 6.4 shows the simulation of the optical modes in a looped nanowire with a straight narrow-gap (red) section and a looped wide-gap (green) section. The diameter of this nanowire is assumed as 250 nm. The length of the narrow-gap section and the diameter of the looped circle are 4 μm and 8 μm respectively. No gain or absorption is assumed in the cavity, since the purpose is to study the pure cavity modes.
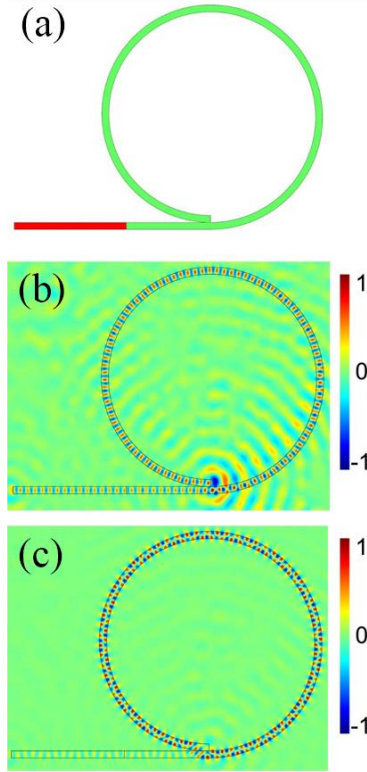
Figure 6.4 (a) Schematic of looped nanowire. Red and green colors indicate the wide-gap and narrow-gap sections respectively. (b,c) E-field pattern of the loop-straight (LS) mode and loop (L) mode respectively.

Figure 6.4(b & c) shows two types of modes: 1) loop-straight (LS) mode: a mode in the entire nanowire including looped and straight section, and 2) loop (L) mode: a mode only in the looped section. Similar to the mode in straight nanowire, the LS mode is mainly confined by the two ends of the nanowire. The mode is relatively uniform in the entire length of the nanowire. There is a weak coupling in the ring cavity so the mode intensity in the ring is slightly stronger than the mode intensity in straight section. Therefore, according to the discussion for the straight nanowire, LS mode can only support the red lasing, since green light suffers huge absorption in the narrow-gap section.

In contrast, L mode is mainly confined in looped section, with minimal leakage to the straight section. Since the gain material in looped section is isolated with the lossy narrow-gap material in the straight section, the green lasing is achievable in L mode. The major loss for the green light is the leaking and scattering loss at the junction of the ring cavity. It is demonstrated that the coupling efficiency at the junction of the looped nanowire ring is very high when the looped end is parallel to the straight end with a short overlap section [158-160]. For the L mode shown in Figure 6.4(c), the simulated Q factor is over 10^4 when neglecting the absorption loss in straight section. In reality, it is difficult to manipulate a perfect junction for the ring cavity. Therefore, the threshold gain of the green lasing is not as low as expected due to the imperfect junction. According to the experimental results, the actual threshold of the green lasing is at the similar level of the threshold of red lasing.

Therefore, the simultaneous green and red lasing is achievable in the looped structure while the green and red lasing are confined in L and LS modes respectively. To further demonstrate the possibility of the simultaneous two-color lasing in this looped nanowire structure, a detail analysis of the average gain in both modes were performed in Chapter 6.5.

It is also interesting to see how the lasing modes emit out from such a structure. In Figure 6.4(b), the red lasing mode emits from both ends of the nanowire, one at the straight section and the other at the junction of the looped cavity. In Figure 6.4(c), the green lasing mode only emits from the end at the looping junction. Although the L mode is weakly coupled to the straight section, due to the strong absorption at the narrow-gap section, the green lasing is impossible to emit from the straight end of the nanowire. Therefore, only

the red lasing can be observed at the straight end of the nanowire, while both red and green

lasing can be observed at the junction of the looped cavity.

6.5 Optical Gain in Straight and Looped Nanowire

In the previous section, we have demonstrated that the straight nanowire can only

support red lasing mode while the looped nanowire can support both green and red lasing

in L and LS modes respectively. The threshold gain in both structures were discussed with

the simplified assumption that the alloy nanowire consists of two sections with wide-gap

material and narrow-gap material respectively. In order to understand the lasing in the

continuously composition-graded alloy nanowire in both straight and looped structures, the

analysis of the optical gain was performed.

When a light at the wavelength λ propagates in the nanowire waveguide, the

amplification of the light intensity follows with

$$\frac{dI}{dl} = \Gamma\, G(\lambda, l)I(l) \tag{6.2}$$

where $I(l)$ is the intensity at the position l on the nanowire, Γ is the confinement factor,

and $G(\lambda, l)$ is the material gain for wavelength λ at position l. Thus, the total amplification

in a round of propagation follows with

$$\frac{I(L)}{I(0)} = \int_0^L \Gamma\, G(\lambda, l)dl \tag{6.3}$$

Since the alloy composition changes along our alloy nanowires, the effective gain is

defined to represent the gain capability in the composition-graded alloy nanowire. The

expression is

95

$$G_{eff}(\lambda) = \frac{1}{L}\int_0^L \Gamma G(\lambda, l)dl \qquad (6.4)$$

L is the total length of the nanowire waveguide. At the lasing condition, the effective gain must overcome the total loss, including the propagation loss and mirror loss.

The gain spectra of CdS_xSe_{1-x} alloy are calculated by the approach in [137]. The parameters of CdS and CdSe for the gain calculation are shown in Table 6.1. Those parameters of CdSSe alloy is obtained through linear interpolation according to Vegard's law. The bowing factor is assumed as zero. A carrier density of $1.5 \times 10^{19} cm^{-3}$ is assumed in the calculation. The gain spectra of pure CdS and pure CdSe materials are shown as the black and red dashed lines in Figure 6.5. The peak gain of CdS and CdSe is above 3000 cm^{-1} and the peak wavelengths are 500 nm and 680 nm respectively. Notice that at the green wavelengths around 500 nm, CdS material provides positive gain but the absorption of CdSe material is over 10^4 cm^{-1}. Meanwhile, at red wavelengths between 650 nm and 700 nm, there are positive gain in CdSe while there is almost no gain and no loss in CdS.

Table 6.1 Parameters for gain spectra calculation [153, 161].

	Effective e⁻ mass	Effective heavy h⁺ mass	Refractive index	Bandgap (eV)	Split-off energy (eV)
CdS	0.21	0.7	2.60	2.44	0.079
CdSe	0.13	0.45	2.56	1.74	0.42

In order to simulate the effective gain of the composition-grated nanowire, we assume the CdS_xSe_{1-x} alloy composition of the nanowire is uniformly graded from pure CdS (x=1) to pure CdSe (x=0). The total length of the alloy nanowire is assumed as 200

μm. According to Equation 6.4, the effective gain spectrum of a straight alloy nanowire is calculated and shown as the orange curve in Figure 6.5. Due to the huge absorption of the narrow-gap materials at green wavelengths, there is no positive gain below 600 nm. The peak wavelength of the effective gain is around 640 nm. Therefore, the green color lasing is not supported in such straight alloy nanowire.
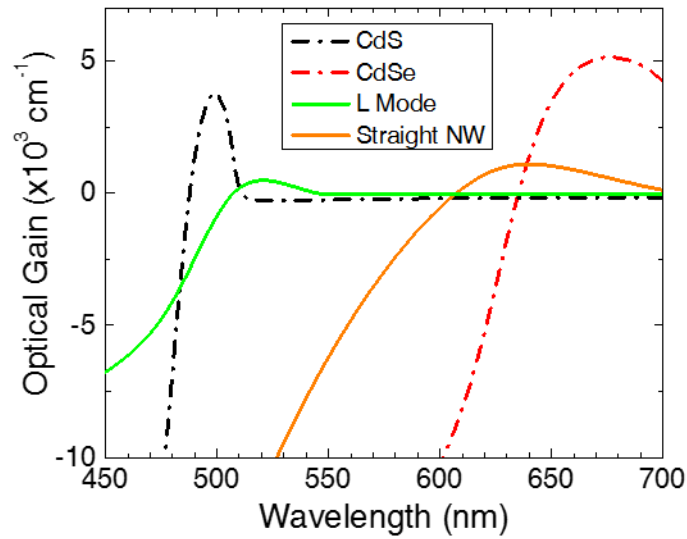
Figure 6.5 Calculated optical gain spectra. Black and red dashed-dot curves are the gain spectra of single-composition CdS and CdSe materials respectively. Orange and green solid curves are the average gain spectra of the straight nanowire and the L mode in looped nanowire structure respective.

When the alloy nanowire is looped at the green end, L mode and LS mode can be formed, as the discussion in Chapter 6.4. The LS mode is similar to the mode in the straight nanowire, that the mode profile is nearly uniform along the nanowire. Thus, the LS mode has similar gain spectra as the straight nanowire, supporting only red color lasing. L mode is concentrated in the looped cavity, thus the effective gain spectrum can be calculated by

integrating the gain in the looped section according to Equation 6.4. As shown in Figure 6.5, the gain spectrum of L mode (green curve) is positive at green wavelengths between 510 nm and 530 nm. This is because the absorptive material at the straight section is isolated from the looped cavity. The peak gain wavelength of L mode is at 520 nm.

Therefore, by this gain analysis, we demonstrated that the L mode and LS mode in the looped alloy nanowire support green and red lasing respectively. If the alloy composition is uniformly graded in the nanowire, the peak gain wavelengths of L and LS modes are 520 nm and 640 nm respectively, with separation of 120 nm.

Theoretically, the maximum wavelength separation in CdSSe alloy is over 200 nm. Such separation can be achieved if the alloy nanowire consists two sections with pure CdS and CdSe material respectively. By looping the CdS section, the green lasing at 505 nm can be achieved in the looped cavity and red lasing at 710 nm can be achieved at the loop-straight cavity. This requires a special bandgap engineering of the alloy nanowire.

CHAPTER 7

TWO-COLOR AND DYNAMICAL COLOR-TUNABLE LASER

In Chapter 6, the design of the looped nanowire and the feasibility of the two-color lasing in a monolithic alloy nanowire were discussed. In this chapter, the experimental demonstration of such two-color laser is presented. The comparison of the lasing modes in an alloy nanowire before the looping and after the looping is shown in Chapter 7.1 and Chapter 7.2. As we expected, only the red color lasing can be observed in the straight alloy nanowire. After looping the green end of the nanowire, simultaneous green and red lasing are demonstrated. In Chapter 7.3, an intentionally release of the looped nanowire further demonstrates the feedback in the looped cavity. Finally, the dynamical tuning of the output lasing color is demonstrated in Chapter 7.4.

7.1 Single-color Lasing in Straight Nanowire

According to the optical mode and gain analysis in Chapter 6.4 and 6.5, the straight alloy nanowire generally only supports the red color lasing. The green lasing is achievable only when the length of the wide-gap section is much longer than the narrow-gap section. Since the CdSSe alloy nanowire used in this work is continuously composition-graded with relatively uniform grading rate, only the red lasing is expected in the straight nanowire.

Optical characterization of the straight CdSSe alloy nanowire is shown in Figure 7.1. A nanowire with length of 200 μm and diameter of 400 nm was placed on a glass substrate, as shown in Figure 7.1(a). By a 405 nm CW laser pumping, the real color PL image in Figure 7.1(b) shows a continuous color changing from red to green. For test the

lasing, a 355 nm YAG laser (9 ns, 10 Hz) was used as the pumping source. The excitation

laser spot is roughly 250 μm in diameter so it uniformly covers the entire nanowire. The

detail information of the measurement setup can be found in Appendix C. The emission

spectra under different pumping power is shown in Figure 7.1(c). Clear lasing peak at 637

nm (red color) can be observed with increasing the pumping power. Due to the low

collection efficiency at the green end, the green emission in the spontaneous spectra is

weaker than the red emission. The integrated intensity of the lasing peak as a function of

the pumping power is plotted in Figure 7.1(d), illustrating a clear lasing threshold with

peak pumping power density at 6.7 kW/cm^2.

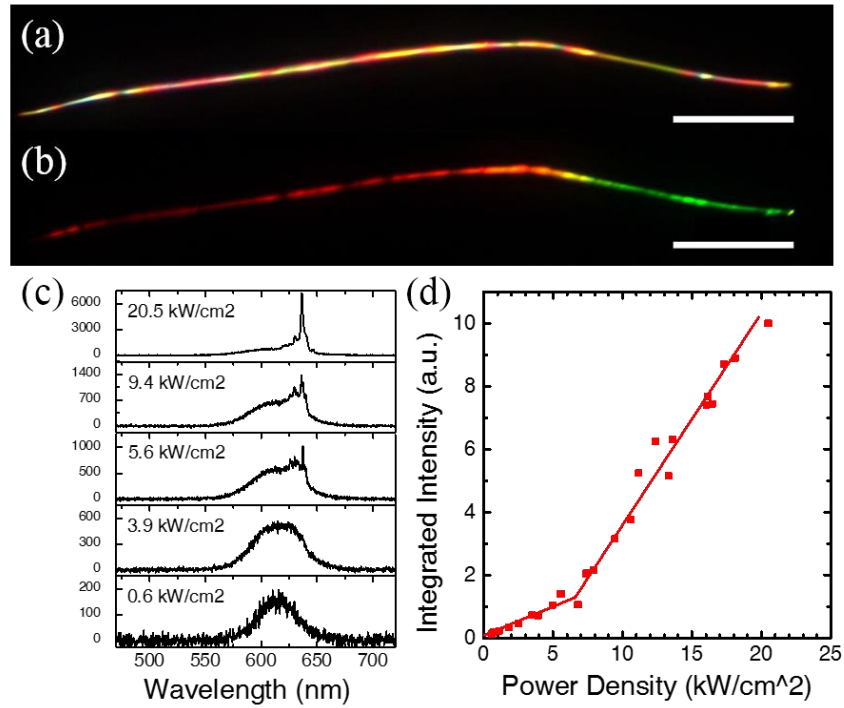Figure 7.1 Single-color lasing in straight alloy nanowire. (a) Dark-field image of the straight alloy nanowire. (b) The real color PL image of the straight nanowire under CW pumping. Scale bars in A and B are 30 μm. (c) Emission spectra under a single excitation pulse with increasing peak power density. (d) The integrated intensity of the lasing peak at 637 nm as a function of the pumping power density.

7.2 Two-color Lasing in Looped Nanowire

By looping the wide-gap (green) end of the alloy nanowire, a separate ring cavity is formed for the green lasing mode. According to the discussion in Chapter 6.4 and 6.5, the simultaneous green and red lasing are prospected in the looped nanowire structure while the junction of the looping gives both green and red lasing output. Figure 7.2 illustrates the two-color lasing result after looping the green end of the same nanowire as in Figure 7.1. A tapered fiber was used to manipulate and loop the green end of the wire into a 15 μm diameter circle, as shown in Figure 7.2(a). The detail information of the micro-manipulating process can be found in Appendix B. Figure 7.2(b) shows the real color image of the dual-color lasing emission under uniform excitation on the entire structure. The yellow bright spot at the junction of the loop (labeled by green arrow) indicates the simultaneous output of the green and red lasing, since the color mixture of green and red lasing appears as yellowish. In addition, there is a red scattering spot (labeled by red arrow) on the straight section of this nanowire. This emission spot is the scattering of a small particle attached on the nanowire. The small particle can be seen from the SEM image in Figure 7.4. Because the green mode is expected to be confined in the ring cavity, the green lasing has minimal leaking at the straight section. Therefore, the particle scattering at the straight section shows a red color, demonstrating the propagation of red lasing mode in the straight section and the confinement of the green lasing mode in the looped section. Contrary to the only red lasing in straight nanowire, the lasing spectra in the looped nanowire in Figure 7.2(c) exhibits significant green and red lasing peaks at 530 nm and 637 nm respectively. The red lasing wavelength is consistent with that before looping.
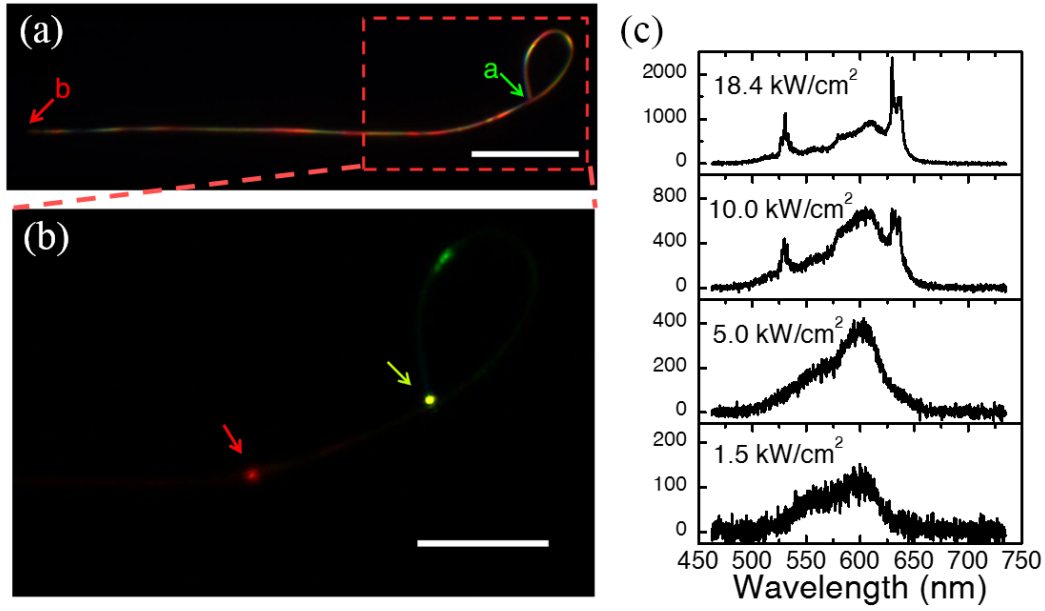
Figure 7.2 Two-color lasing in looped nanowire structure. This nanowire is the same one used in Figure 7.1. (a) Dark-field image of the looped nanowire. Labels *a* and *b* indicate the junction of looping and the narrow-gap end of the nanowire, respectively. Scale bar is 30 μm. (b) Real color image under two-color lasing operation. The image area corresponds to the red dashed box in (a). Scale bar is 15 μm. Green arrow indicates the junction of the loop, corresponding to the position *a* in (a). Red arrow points to a scattering center on the nanowire body. (c) Emission spectra under a single excitation pulse with increasing peak power density.

Figure 7.3(a) illustrates the output intensities of the two lasing peaks as a function of total pumping power density. Clear threshold behavior for both lasing can be observed. The threshold power density of red and green lasing are 6.9 kW/cm^2 and 8.7 kW/cm^2 respectively. The clear threshold is also evidenced by the well-known "S"-shaped curve when the laser intensity is plotted against pumping intensity on log-log scales, as shown in Figure 7.3(b). The slopes of the transition regions (mid sections) for green and red lasing modes are 3.0 and 2.7, respectively. The S-shape curves were fitted by multimode lasing model proposed in [162]. The best fitted total spontaneous emission factors are 0.075 and 0.09 for green and red lasing modes, respectively.
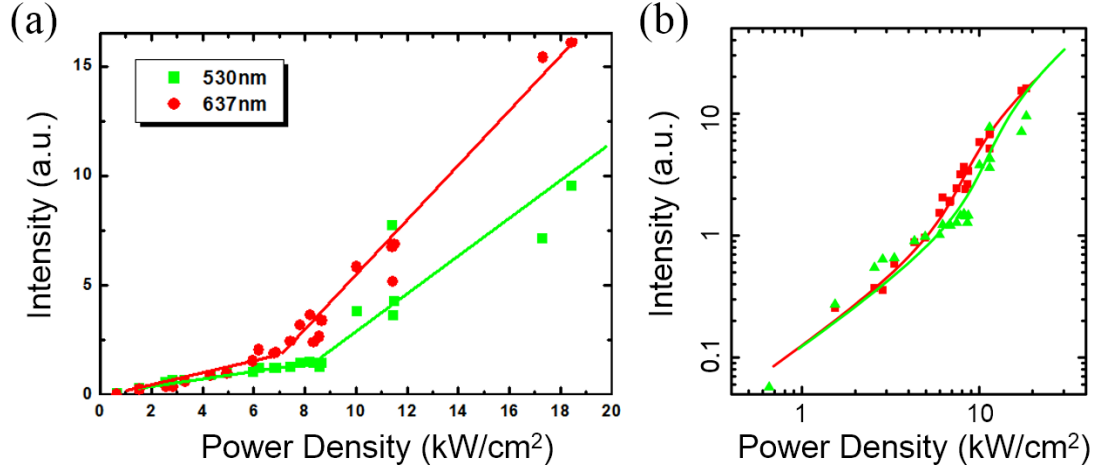
Figure 7.3 The integrated intensity of the lasing peaks at 530 nm (green) and 637 nm (red) as the function of pumping power density. (a) Linear scale plot. The solid guiding lines indicate clear threshold behavior. (b) Log-log scale plot. The solid curves represent the fitting results using multimode lasing model [162].

The wavelength separation of green and red lasing modes is 107 nm, much larger than the gain bandwidth of the typical II-VI semiconductors of a single composition [153-157]. The lasing wavelength separation is determined by the composition distribution on the alloy nanowire. According to the discussion in Chapter 6.5, the peak wavelength of the average gain in the looped section is longer than the emission wavelength of the material at wide-gap end, due to the continuously graded composition in the nanowire. Similarly, the peak wavelength of the average gain of the loop-straight mode is shorter than the emission wavelength of the material at narrow-gap end. Therefore, the lasing wavelength separation is smaller than the emission wavelength separation of the materials at two ends in the continuously composition-graded alloy nanowire. If the nanowire consists of two sections with pure CdS and pure CdSe material, as the structure shown in Figure 6.4(a), the green and red lasing wavelength will be around 505 nm and 710 nm respectively,

resulting the maximum wavelength separation over 200 nm. However, this requires a special bandgap engineering on the alloy nanowire.
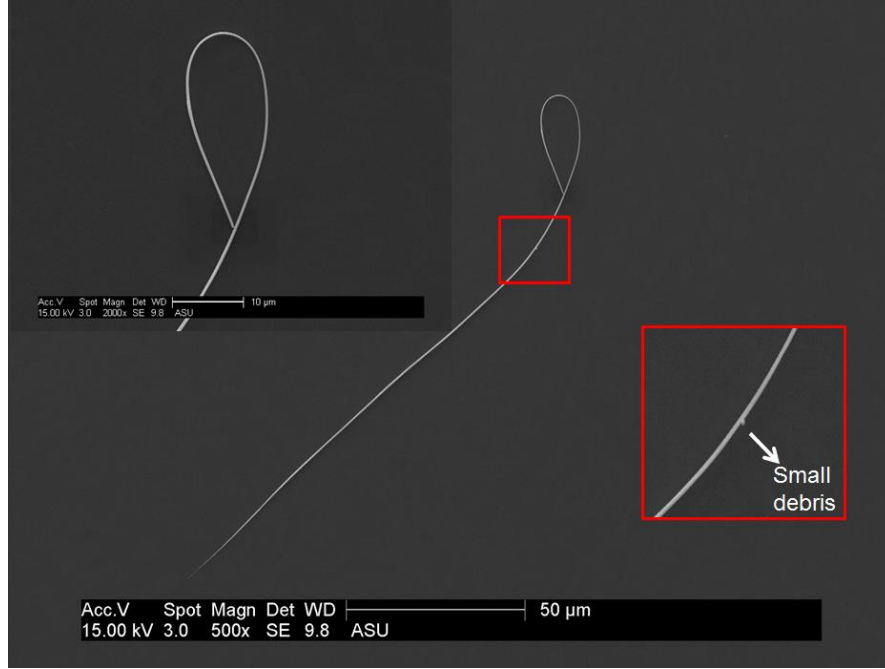
Figure 7.4 SEM image of the looped nanowire which showed two-color lasing. Inset on the top left: zoom-in of the looped part. Lower right inset: zoom-in feature of a small particle attached to the nanowire, which causes the red scattering point in Figure 7.2(b).

A confocal PL measurement was studied for analyzing the lasing output in this looped nanowire, as shown in Figure 7.5. By inserting a pinhole into the confocal image plane of the microscopy system, the emission collection area is limited to a spot less than 5 μm. The detail information of the confocal system is presented in Appendix C The localized collection was performed at the looping junction and the narrow-gap end of the nanowire, which correspond to position *a* and *b* in Figure 7.2(a) respectively. The pumping power is higher than the thresholds of green and red lasing to ensure the simultaneous two-color lasing. The spectrum at the junction shows both green and red lasing peaks, in

contrast with the spectrum at CdSe-rich end which only exhibits the longer wavelength lasing. This result is consistent with the discussion in Chapter 6.4. Because of the spatial filtering effect of the confocal system, the green lasing peaks are more distinguishable than those obtained with a large collection area in Figure 7.2(c). The linewidth of a single lasing peak at 526 nm is 0.9 nm, close to the resolution limitation of the spectrometer.
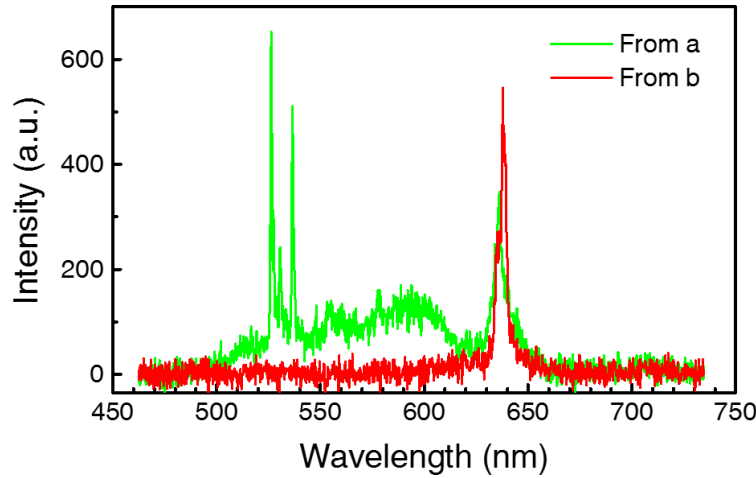
Figure 7.5 Confocal PL measurement at the position *a* and *b* in the looped nanowire shown in Figure 7.2(a). Position *a* and *b* correspond to the looping junction and narrow-gap end of the nanowire respectively. The nanowire is under two-color lasing operation.

7.3 Further Demonstration of Feedback in Looped Cavity

Figure 7.6 presents the two-color lasing from another looped alloy CdSSe nanowire. The total length of this nanowire is 130 μm and the diameter of the looped ring is 16 μm. The PL imaging under low pumping power (Figure 7.6(b)) illustrates the alloy composition distribution along this nanowire. The colors from green to orange correspond to the spontaneous emission from various parts. Because the Se composition in the CdSe-rich

section of this nanowire is lower than the one in Figure 7.2, the PL wavelength span of this wire is somewhat smaller. The blue color in the PL image is the scattered excitation laser light which is not completely.

The laser spectrum in Figure 7.6(d) presents simultaneous two lasing peaks at 546 nm (green) and 582 nm (orange). Because shorter composition span range, the wavelength separation of this looped nanowire is smaller than the one in the previous chapters. Figure 7.6(c) shows the real color image when the pumping power is above the lasing threshold. According to the discussion above, both the long (orange) and short (green) wavelength lasing modes emit at the junction while only orange mode emits at the end-face of the right narrow-gap section. Therefore, an intermediate lasing color between green and orange is observed at the junction point and the output color at the narrow-gap end remains as orange, as shown in Figure 7.6(c).
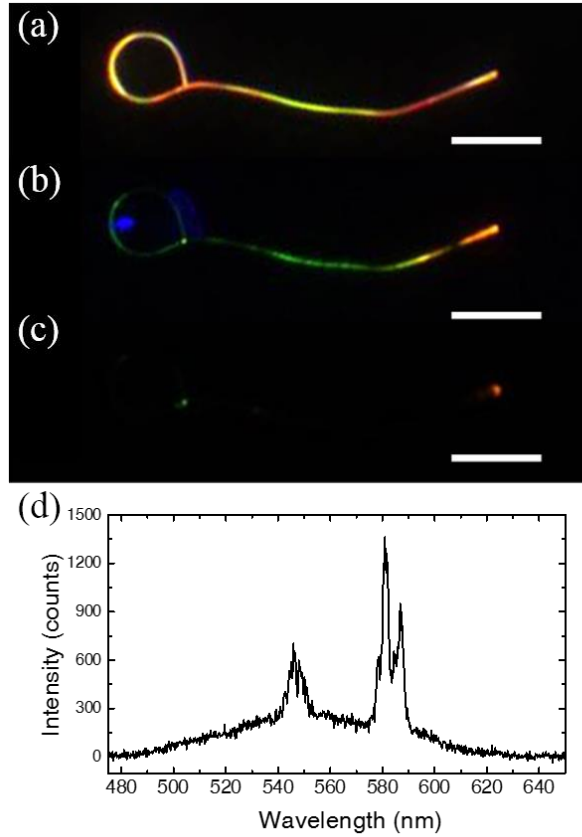
Figure 7.6 Two-color lasing from another looped nanowire. (a) The dark-field image of the looped nanowire. (b) Real-color PL image with CW excitation. The blue color around the circle is the scattering of the pump laser. (c) Real-color image under two-color lasing operation. The two bright spots showing yellow-green and orange colors can be observed at the looping junction and narrow-gap end respectively Scale bars in (a), (b), and (c) are 20 μm. (d) Spectrum of two-color lasing.

In order to further demonstrate the important role of the looped feedback in two-color lasing, we intentionally opened the loop at the junction point of the looped structure as shown in Figure 7.7. Although some of the green emission can be coupled from the wide-gap end to the nanowire body through free space, the coupling efficiency is much lower than fully looped situation in Figure 7.6. As the expectation, the partially looped structure in Fig. 7.7(a) cannot provide enough feedback, resulting the despair of the green lasing peak, as illustrated in Figure 7.6(d). The red lasing modes remain practically the

107

same as before, indicating that the feedback of the loop junction has little influence on the red lasing modes. With the comparison of lasing spectra in looped and loosed structures, it is clear that the feedback in the looped section is the key to achieve green mode lasing, and thus simultaneous two-color lasing.
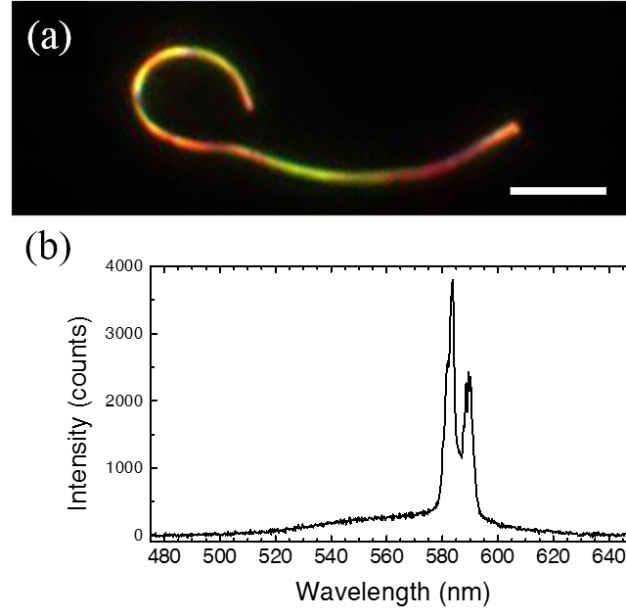
Figure 7.7 (a) Dark-field image of the nanowire in Figure 7.6. The loop was opened slightly so the ring cavity does not exist in this structure. (b) Lasing spectrum.

7.4 Dynamic Tuning of Output Laser Color

One unique property of the looped nanowire design is the common output position for two-color lasing, as the analysis in Chapter 6.4. Unlike the regular RGB lasers which combine the three laser devices [129, 163] and some other multicolor lasers [141, 145], our two-color laser does not require external guiding to mix the multi-color lasing beams. Such unique feature allows us to achieve color-tunable output via pumping the straight and

looped segments separately, as indicated in Figure 6.2(c). A beam splitter was used to split the excitation laser into two beams for pumping the straight section and looped section separately. The detail information of the two-beam pumping setup can be found in Appendix D. The spot shape, pumping position and pumping power of the two excitation beams can be controlled individually and precisely in this two-beam excitation setup.

Figure 7.8(A) shows the dark-field image of a looped nanowire. Two excitation beams are focused to less than 40 μm spot size to the looped and straight sections respectively. By adjusting the intensities of two pumping beams, the output color at the junction was tuned from green (B1) to yellow-green (B2) to yellow (B3) to orange (B4). Figure 7.8(C1-C4) show the lasing spectra corresponding to B1-B4. In C1 and C4, only one of the two excitation beams was used for excitation while the other one is blocked. Therefore only one lasing color is observed at either 530 nm (green) or 588 nm (orange). In C2 and C3, the relative intensity of the green and orange lasing is controlled at 6:4 and 3:7, respectively. The mixed colors are represented as the intermediate colors between green and orange, which are close to yellowish green (B2) and yellow (B3). In Figure 7.8(D), the chromaticity of C1-C4 spectra are marked on CIE 1931 color space by ★, ▲, ● and ■ respectively. The mono-wavelength lasing of C1 and C4 are located at the curved edge of the color space. C2 and C3 can be considered as the linear combination of two equivalent wavelengths, and the corresponding chromaticity are marked on the dashed line in Figure 7.8(D). The calculated colors in Figure 7.8(D) match perfectly with the colors in real color images shown in Figure 7.8(B1-B4), further demonstrating the monochromic property and color tunability of this looped nanowire laser. Additionally, any color on the dashed line can be obtained from this nanowire by precise control of the relative power of

the pumping beams. Such continuously controllable colors are critically important for many applications such as color-by-design for lighting and color display.
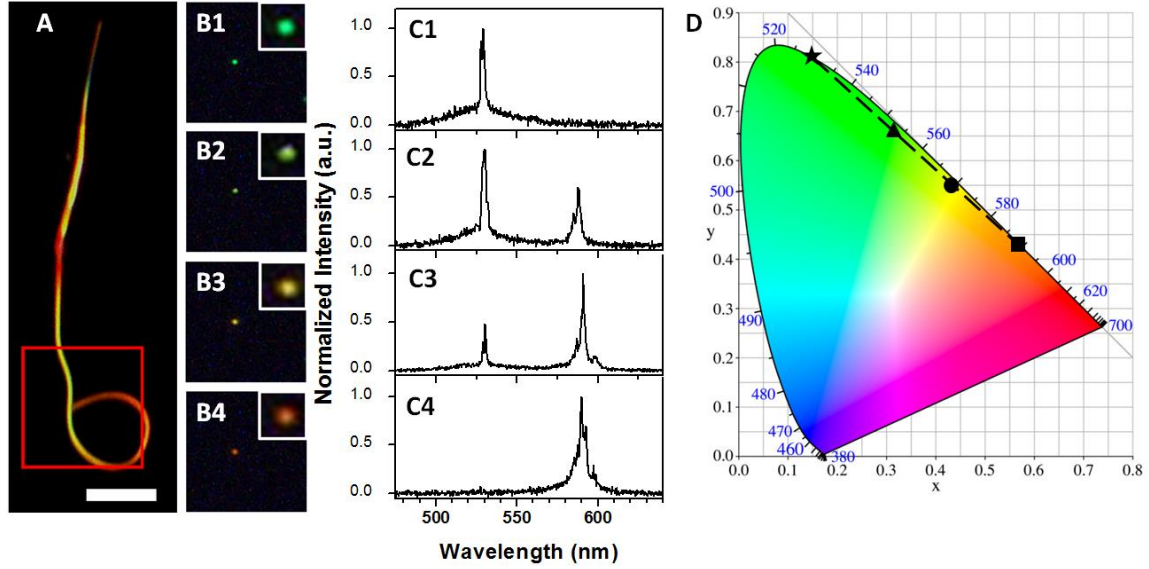
Figure 7.8 Dynamical lasing color tuning in the looped nanowire. (A) Dark field image of the looped nanowire. The scale bar is 10 μm. (B1-B4) Real color images of the lasing under different pumping for the two cavities. The images were taken from the red box in (A). The bright spots correspond the position at the junction of the loop. The insets are the zoom-in images of the junction lasing spots. (C1-C4) Normalized lasing spectra under different controlled pumping intensities, collected simultaneously with the images of C1-C4. (D) The calculated colors from the spectra in C1-C4 plotted on CIE1931 color space. Star (★), triangular (▲), circle (●) and square (■) labels correspond to C1-C4, respectively.

7.5 Conclusions

In Chapter 6 & 7, a novel design of the two-color laser based on composition-graded CdSSe alloy nanowire was demonstrated. The composition of CdSSe alloy continuously varies along the nanowire axis from pure CdS to pure CdSe. Analytical studies of the optical modes and net gain support that by looping the wide-gap end of the

nanowire, the green and red lasing modes can be separated in the looped and straight sections respectively. Therefore, the net gain at both green and red wavelengths is achievable. Experimentally, the simultaneous green and red color lasing was demonstrated with 107 nm wavelength separation, which is much larger than the gain bandwidth of a single-composition semiconductor. In addition, the dynamic control of the combined lasing colors from green to red was demonstrated. Any intermediate color between the two lasing wavelengths is feasible by adjusting the excitation power at the two cavities. The looped nanowire design is the first demonstration showing the simultaneous two-color lasing and tunable lasing colors in an extremely wide wavelength range in a monolithic nanowire. The wide-range flexible lasing colors and the active color tunability in such a small device reveal great potential in the applications to the tunable laser sources in photonic integrated circuits, on-chip laser display and other situation where the dynamical color control is needed.

REFERENCES

[1]   R. Mears, L. Reekie, I. Jauncey, and D. Payne, "Low-noise erbium-doped fibre amplifier operating at 1.54 μm," Electronics Letters **23**, 1026-1028 (1987).

[2]   C. R. Giles, and E. Desurvire, "Modeling erbium-doped fiber amplifiers," Lightwave Technology, Journal of **9**, 271-283 (1991).

[3]   P. F. Wysocki, J. B. Judkins, R. P. Espindola, M. Andrejco, and A. M. Vengsarkar, "Broad-band erbium-doped fiber amplifier flattened beyond 40 nm using long-period grating filter," Photonics Technology Letters, IEEE **9**, 1343-1345 (1997).

[4]   E. Desurvire, C. R. Giles, and J. R. Simpson, "Gain saturation effects in high-speed, multichannel erbium-doped fiber amplifiers at λ= 1.53 μm," Lightwave Technology, Journal of **7**, 2095-2104 (1989).

[5]   E. Desurvire, "Analysis of noise figure spectral distribution in erbium doped fiber amplifiers pumped near 980 and 1480 nm," Applied optics **29**, 3118-3125 (1990).

[6]   C. Giles, J. Simpson, and E. Desurvire, "Transient gain and cross talk in erbium-doped fiber amplifiers," Optics Letters **14**, 880-882 (1989).

[7]   R. Mears, L. Reekie, S. Poole, and D. Payne, "Low-threshold tunable CW and Q-switched fibre laser operating at 1.55 μm," Electronics Letters **22**, 159-160 (1986).

[8]   J. Kafka, D. Hall, and T. Baer, "Mode-locked erbium-doped fiber laser with soliton pulse shaping," Optics letters **14**, 1269-1271 (1989).

[9]   P. F. Wysocki, M. J. Digonnet, B. Kim, and H. J. Shaw, "Characteristics of erbium-doped superfluorescent fiber sources for interferometric sensor applications," Lightwave Technology, Journal of **12**, 550-567 (1994).

[10] A. Schweinsberg, N. Lepeshkin, M. Bigelow, R. Boyd, and S. Jarabo, "Observation of superluminal and slow light propagation in erbium-doped optical fiber," EPL (Europhysics Letters) **73**, 218 (2006).

[11] R. Soref, "The past, present, and future of silicon photonics," Selected Topics in Quantum Electronics, IEEE Journal of **12**, 1678-1687 (2006).

[12] J. D. Bradley, and M. Pollnau, "Erbium‑doped integrated waveguide amplifiers and lasers," Laser & Photonics Reviews **5**, 368-403 (2011).

[13] A. Polman, "Erbium implanted thin film photonic materials," Journal of Applied Physics **82**, 1-39 (1997).

[14] W. Miniscalco, "Erbium-doped glasses for fiber amplifiers at 1500 nm," Lightwave Technology, Journal of **9**, 234-250 (1991).

[15] Y. Yan, A. J. Faber, H. De Waal, P. G. Kik, and A. Polman, "Erbium-doped phosphate glass waveguide on silicon with 4.1 dB/cm gain at 1.535 μm," Applied Physics Letters **71**, 2922-2924 (1997).

[16] E. Snoeks, G. Van den Hoven, A. Polman, B. Hendriksen, M. Diemeer, and F. Priolo, "Cooperative upconversion in erbium-implanted soda-lime silicate glass optical waveguides," JOSA B **12**, 1468-1474 (1995).

[17] J. Shmulovich, Y. Wong, P. Becker, A. Bruce, R. Adar, and A. Wong, "Er3+ glass waveguide amplifier at 1.5 μm on silicon," Electronics Letters **28**, 1181-1182 (1992).

[18] X. Orignac, D. Barbier, X. Du, and R. Almeida, "Fabrication and characterization of sol‑gel planar waveguides doped with rare‑earth ions," Applied physics letters **69**, 895-897 (1996).

[19] W. Huang, R. Syms, E. Yeatman, M. Ahmad, T. Clapp, and S. Ojha, "Fiber-device-fiber gain from a sol-gel erbium-doped waveguide amplifier," Photonics Technology Letters, IEEE **14**, 959-961 (2002).

[20] B. Hwang, S. Jiang, T. Luo, J. Watson, S. Honkanen, Y. Hu, F. Smektala, J. Lucas, and N. Peyghambarian, "Erbium-doped phosphate glass fibre amplifiers with gain per unit length of 2.1 dB/cm," Electronics Letters **35**, 1007-1009 (1999).

[21] M. Dinand, and W. Sohler, "Theoretical modeling of optical amplification in Er-doped Ti: LiNbO 3 waveguides," Quantum Electronics, IEEE Journal of **30**, 1267-1276 (1994).

[22] B. Das, R. Ricken, and W. Sohler, "Integrated optical distributed feedback laser with Ti: Fe: Er: LiNbO 3 waveguide," Applied physics letters **82**, 1515-1517 (2003).

[23] E. Boulma, M. Diaf, J. Jouart, M. Bouffard, J. Doualan, and R. Moncorgé, "Anti-Stokes emissions and determination of Stark sub-level diagram of Er3+ ions in KY3F10," Journal of Physics: Condensed Matter **18**, 6721 (2006).

[24] A. Kahn, H. Kühn, S. Heinrich, K. Petermann, J. D. Bradley, K. Wörhoff, M. Pollnau, Y. Kuzminykh, and G. Huber, "Amplification in epitaxially grown Er:(Gd, Lu) 2 O 3 waveguides for active integrated optical devices," JOSA B **25**, 1850-1853 (2008).

[25] J. Remsa, M. Jelinek, T. Kocourek, J. Oswald, V. Studnička, M. Čerňanský, F. Uherek, and M. Jelínek, "Highly oriented crystalline Er: YAG and Er: YAP layers prepared by PLD and annealing," Applied Surface Science **255**, 5292-5294 (2009).

[26] R. Dahal, C. Ugolini, J. Lin, H. Jiang, and J. Zavada, "Erbium-doped GaN optical amplifiers operating at 1.54 μm," Applied Physics Letters **95**, 111109-111109-111103 (2009).

[27] Z. Zhou, T. Komori, M. Yoshino, M. Morinaga, N. Matsunami, A. Koizumi, and Y. Takeda, "Enhanced 1.54 μm photoluminescence from Er-containing ZnO through nitrogen doping," Applied Physics Letters **86**, 041107-041107-041103 (2005).

[28] P. Favennec, H. L'haridon, M. Salvi, D. Moutonnet, and Y. Le Guillou, "Luminescence of erbium implanted in various semiconductors: IV, III-V and II-VI materials," Electronics Letters **25**, 718-719 (1989).

[29] F. Priolo, G. Franzo, S. Coffa, A. Polman, S. Libertino, R. Barklie, and D. Carey, "The erbium‐impurity interaction and its effects on the 1.54 μm luminescence of Er3+ in crystalline silicon," Journal of applied physics **78**, 3874-3882 (1995).

[30] G. Franzo, S. Coffa, F. Priolo, and C. Spinella, "Mechanism and performance of forward and reverse bias electroluminescence at 1.54 μm from Er-doped Si diodes," Journal of applied physics **81**, 2784-2793 (1997).

[31] S. Saini, K. Chen, X. Duan, J. Michel, L. C. Kimerling, and M. Lipson, "Er2O3 for high-gain waveguide amplifiers," Journal of electronic materials **33**, 809-814 (2004).

[32] M. Miritello, R. L. Savio, A. Piro, G. Franzò, F. Priolo, F. Iacona, and C. Bongiorno, "Optical and structural properties of Er2O3 films grown by magnetron sputtering," Journal of applied physics **100**, 013502 (2006).

[33] J. Zheng, W. Ding, C. Xue, Y. Zuo, B. Cheng, J. Yu, Q. Wang, G. Wang, and H. Guo, "Highly efficient photoluminescence of Er 2 SiO 5 films grown by reactive magnetron sputtering method," Journal of Luminescence **130**, 411-414 (2010).

[34] H.-J. Choi, J. H. Shin, K. Suh, H.-K. Seong, H.-C. Han, and J.-C. Lee, "Self-organized growth of Si/Silica/Er2Si2O7 core-shell nanowire heterostructures and their luminescence," Nano letters **5**, 2432-2437 (2005).

[35] B. Wang, R. Guo, L. Wang, X. Wang, and Z. Zhou, "1.53 μm electroluminescence of Erbium excited by hot carriers in ErRE (RE= Yb, Y) silicates," (2012).

[36] K. Suh, M. Lee, J. S. Chang, H. Lee, N. Park, G. Y. Sung, and J. H. Shin, "Cooperative upconversion and optical gain in ion-beam sputter-deposited Er x Y 2-x SiO 5 waveguides," Optics express **18**, 7724-7731 (2010).

[37] L. Wang, R. Guo, B. Wang, X. Wang, and Z. Zhou, "Hybrid Si 3 N 4-Er/Yb/Y silicate waveguide amplifier with 1.25 dB/cm internal gain," in *Group IV Photonics (GFP), 2012 IEEE 9th International Conference on*(IEEE, 2012), pp. 249-251.

[38] C. Michael, H. Yuen, V. Sabnis, T. Johnson, R. Sewell, R. Smith, A. Jamora, A. Clark, S. Semans, and P. Atanackovic, "Growth, processing, and optical properties of epitaxial Er 2 O 3 on silicon," Optics express **16**, 19649-19666 (2008).

[39] A. Pan, L. Yin, Z. Liu, M. Sun, R. Liu, P. L. Nichols, Y. Wang, and C. Ning, "Single-crystal erbium chloride silicate nanowires as a Si-compatible light emission material in communication wavelength," Optical Materials Express **1**, 1202-1209 (2011).

[40] L. Yin, H. Ning, S. Turkdogan, Z. Liu, P. L. Nichols, and C. Ning, "Long lifetime, high density single-crystal erbium compound nanowires as a high optical gain material," Applied Physics Letters **100**, 241905 (2012).

[41] E. Desurvire, *Erbium-doped fiber amplifiers: principles and applications* (Wiley-Interscience, 2002).

[42] R. I. Laming, S. B. Poole, and E. Tarbox, "Pump excited-state absorption in erbium-doped fibers," Optics letters **13**, 1084-1086 (1988).

[43] F. Auzel, "Upconversion and anti-stokes processes with f and d ions in solids," Chemical reviews **104**, 139-174 (2004).

[44] F. Auzel, "Upconversion processes in coupled ion systems," Journal of Luminescence **45**, 341-345 (1990).

[45] T. Lu, L. Yang, R. V. van Loon, A. Polman, and K. Vahala, "An on-chip Erbium doped three-photon upconversion silica microlaser emitting at green wavelengths," in *Conference on Lasers and Electro-Optics*(Optical Society of America, 2008), p. CTuGG3.

[46] E. Desurvire, J. Sulhoff, J. Zyskind, and J. Simpson, "Study of spectral dependence of gain saturation and effect of inhomogeneous broadening in erbium-doped aluminosilicate fiber amplifiers," Photonics Technology Letters, IEEE **2**, 653-655 (1990).

[47] B. H. Hong, S. C. Bae, C.-W. Lee, S. Jeong, and K. S. Kim, "Ultrathin single-crystalline silver nanowire arrays formed in an ambient solution phase," Science **294**, 348-351 (2001).

[48] B. Wu, A. Heidelberg, and J. J. Boland, "Mechanical properties of ultrahigh-strength gold nanowires," Nature materials **4**, 525-529 (2005).

[49] Y. Li, G. Meng, L. Zhang, and F. Phillipp, "Ordered semiconductor ZnO nanowire arrays and their photoluminescence properties," Applied Physics Letters **76**, 2011-2013 (2000).

[50] X. Duan, and C. M. Lieber, "Laser-assisted catalytic growth of single crystal GaN nanowires," Journal of the American Chemical Society **122**, 188-189 (2000).

[51] Y. Wang, G. Meng, L. Zhang, C. Liang, and J. Zhang, "Catalytic growth of large-scale single-crystal CdS nanowires by physical evaporation and their photoluminescence," Chemistry of materials **14**, 1773-1777 (2002).

[52] Y. Cui, L. J. Lauhon, M. S. Gudiksen, J. Wang, and C. M. Lieber, "Diameter-controlled synthesis of single-crystal silicon nanowires," Applied Physics Letters **78**, 2214-2216 (2001).

[53] K. Saulig-Wenger, D. Cornu, F. Chassagneux, T. Epicier, and P. Miele, "Direct synthesis of amorphous silicon dioxide nanowires and helical self-assembled nanostructures derived therefrom," Journal of Materials Chemistry **13**, 3058-3061 (2003).

[54] H. He, C. Li, and N. Tao, "Conductance of polymer nanowires fabricated by a combined electrodeposition and mechanical break junction method," Applied Physics Letters **78**, 811-813 (2001).

[55] Z. Fan, and J. G. Lu, "Electrical properties of ZnO nanowire field effect transistors characterized with scanning probes," Applied Physics Letters **86**, 032111 (2005).

[56] M. H. Huang, S. Mao, H. Feick, H. Yan, Y. Wu, H. Kind, E. Weber, R. Russo, and P. Yang, "Room-temperature ultraviolet nanowire nanolasers," science **292**, 1897-1899 (2001).

[57] J. C. Johnson, H.-J. Choi, K. P. Knutsen, R. D. Schaller, P. Yang, and R. J. Saykally, "Single gallium nitride nanowire lasers," Nature materials **1**, 106-110 (2002).

[58] J. Law, and J. Thong, "Simple fabrication of a ZnO nanowire photodetector with a fast photoresponse time," Applied Physics Letters **88**, 133114 (2006).

[59] M. Curreli, C. Li, Y. Sun, B. Lei, M. A. Gundersen, M. E. Thompson, and C. Zhou, "Selective functionalization of In2O3 nanowire mat devices for biosensing applications," Journal of the American Chemical Society **127**, 6922-6923 (2005).

[60] Q. Wan, Q. Li, Y. Chen, T.-H. Wang, X. He, J. Li, and C. Lin, "Fabrication and ethanol sensing characteristics of ZnO nanowire gas sensors," Applied Physics Letters **84**, 3654-3656 (2004).

[61] L. Tsakalakos, J. Balch, J. Fronheiser, B. Korevaar, O. Sulima, and J. Rand, "Silicon nanowire solar cells," Applied Physics Letters **91**, 233117 (2007).

[62] R. Wagner, and W. Ellis, "Vapor‐liquid‐solid mechanism of single crystal growth," Applied Physics Letters, 89-90 (1964).

[63] The International Centre for Diffraction Data, http://www.icdd.com/products/.

[64] F. Priolo, G. Franzò, S. Coffa, and A. Carnera, "Excitation and nonradiative deexcitation processes of Er 3+ in crystalline Si," Physical Review B **57**, 4443 (1998).

[65] T. Ohtsuki, N. Peyghambarian, S. Honkanen, and S. I. Najafi, "Gain characteristics of a high concentration Er3+‑doped phosphate glass waveguide," Journal of applied physics **78**, 3617-3621 (1995).

[66] G. Van den Hoven, R. Koper, A. Polman, C. Van Dam, J. Van Uffelen, and M. Smit, "Net optical gain at 1.53 μm in Er‑doped Al2O3 waveguides on silicon," Applied Physics Letters **68**, 1886-1888 (1996).

[67] H.-S. Han, S.-Y. Seo, J. H. Shin, and N. Park, "Coefficient determination related to optical gain in erbium-doped silicon-rich silicon oxide waveguide amplifier," Applied physics letters **81**, 3720-3722 (2002).

[68] M. Miritello, R. Lo Savio, F. Iacona, G. Franzò, A. Irrera, A. M. Piro, C. Bongiorno, and F. Priolo, "Efficient luminescence and energy transfer in erbium silicate thin films," Advanced Materials **19**, 1582-1588 (2007).

[69] C. Ayasse, and H. A. Eick, "Synthesis and crystal structure of triytterbium chloroorthosilicate, Yb3 (SiO4) 2Cl," Inorganic Chemistry **12**, 1140-1143 (1973).

[70] The Cambridge Crystallographic Data Centre, http://www.ccdc.cam.ac.uk/Solutions/FreeSoftware/Pages/FreeMercury.aspx.

[71] Y. Yin, K. Sun, W. Xu, G. Ran, G. Qin, S. Wang, and C. Wang, "1.53 μm photo-and electroluminescence from Er3+ in erbium silicate," Journal of Physics: Condensed Matter **21**, 012204 (2009).

[72] D. Li, and C. Ning, "Electrical injection in longitudinal and coaxial heterostructure nanowires: a comparative study through a three-dimensional simulation," Nano letters **8**, 4234-4237 (2008).

[73] E. Desurvire, and J. R. Simpson, "Evaluation of 4 I 15/2 and 4 I 13/2 Stark-level energies in erbium-doped aluminosilicate glass fibers," Optics letters **15**, 547-549 (1990).

[74] C. C. Robinson, "Multiple sites for Er 3+ in alkali silicate glasses (I). The principal sixfold coordinated site of Er 3+ in silicate glass," Journal of Non-Crystalline Solids **15**, 1-9 (1974).

[75] J. B. Gruber, J. Henderson, M. Muramoto, K. Rajnak, and J. G. Conway, "Energy Levels of Single‑Crystal Erbium Oxide," The Journal of Chemical Physics **45**, 477-482 (1966).

[76] N. Alekseev, V. Gapontsev, M. Zhabotinskii, V. Kravchenko, and I. P. Rudnitskii, "Laser phosphate glasses," Moscow Izdatel Nauka **1** (1980).

[77] C. Layne, and M. Weber, "Multiphonon relaxation of rare-earth ions in beryllium-fluoride glass," Physical Review B **16**, 3259 (1977).

[78] F. ZHENG, X. Shiqing, Z. Shilong, D. Degang, H. Youjie, and W. Huanping, "Spectroscopic investigations on Er 3+/Yb 3+-doped oxyfluoride glass ceramics containing YOF nanocrystals," Journal of Rare Earths **30**, 137-141 (2012).

[79] M. Bresler, O. Gusev, N. Sobolev, E. Terukov, I. Yassievich, B. Zakharchenya, and T. Gregorkevich, "Mechanisms of excitation and thermal quenching of erbium-ion luminescence in crystalline and amorphous silicon," Physics of the Solid State **41**, 770-773 (1999).

[80] A. Neuhalfen, and B. Wessels, "Photoluminescent properties of Er‐doped In1−xGaxP prepared by metalorganic vapor phase epitaxy," Applied physics letters **59**, 2317-2319 (1991).

[81] H. Isshiki, and T. Kimura, "Toward small size waveguide amplifiers based on erbium silicate for silicon photonics," IEICE transactions on electronics **91**, 138-144 (2008).

[82] X. Orignac, D. Barbier, X. M. Du, R. M. Almeida, O. McCarthy, and E. Yeatman, "Sol–gel silica/titania-on-silicon Er/Yb-doped waveguides for optical amplification at 1.5 μm," Optical Materials **12**, 1-18 (1999).

[83] E. Desurvire, and J. R. Simpson, "Amplification of spontaneous emission in erbium-doped single-mode fibers," Lightwave Technology, Journal of **7**, 835-845 (1989).

[84] S. E. Stokowski, R. Saroyan, and M. J. Weber, *Nd-doped laser glass spectroscopic and physical properties* (Lawrence Livermore National Laboratory, University of California Livermore, CA, 1981).

[85] O. Lumholt, T. Rasmussen, and A. Bjarklev, "Modelling of extremely high concentration erbium-doped silica waveguides," Electronics Letters **29**, 495-496 (1993).

[86] J. Bradley, L. Agazzi, D. Geskus, F. Ay, K. Wörhoff, and M. Pollnau, "Gain bandwidth of 80 nm and 2 dB/cm peak gain in Al 2 O 3: Er 3+ optical amplifiers on silicon," JOSA B **27**, 187-196 (2010).

[87] X. Wang, G. Yuan, H. Isshiki, T. Kimura, and Z. Zhou, "Photoluminescence enhancement and high gain amplification of Er x Y 2-x SiO 5 waveguide," Journal of Applied Physics **108**, 013506-013506-013504 (2010).

[88] M. Miritello, P. Cardile, R. Lo Savio, and F. Priolo, "Energy transfer and enhanced 1.54 μm emission in Erbium-Ytterbium disilicate thin films," Optics express **19**, 20761-20772 (2011).

[89] C. P. Michael, "Optical material characterization using microdisk cavities," (California Institute of Technology, 2009).

[90] M. Miritello, R. L. Savio, F. Iacona, G. Franzo, C. Bongiorno, and F. Priolo, "Synthesis and luminescence properties of erbium silicate thin films," Materials Science and Engineering: B **146**, 29-34 (2008).

[91] A. Oster, G. Erbert, and H. Wenzel, "Gain spectra measurements by a variable stripe length method with current injection," Electronics Letters **33**, 864-866 (1997).

[92] http://en.wikipedia.org/wiki/Gamma_correction.

[93] C. Ning, "Semiconductor nanolasers," physica status solidi (b) **247**, 774-788 (2010).

[94] COMSOL, Inc., http://www.comsol.com/.

[95] W. L. Barnes, R. Laming, E. J. Tarbox, and P. Morkel, "Absorption and emission cross section of Er 3+ doped silica fibers," Quantum Electronics, IEEE Journal of **27**, 1004-1010 (1991).

[96] J. S. Chang, I. Y. Kim, G. Y. Sung, and J. H. Shin, "Population inversion and low cooperative upconversion in Er-doped silicon-rich silicon nitride waveguide," Optics express **19**, 8406-8412 (2011).

[97] W. J. Miniscalco, and R. S. Quimby, "General procedure for the analysis of Er 3+ cross sections," Optics letters **16**, 258-260 (1991).

[98] H. Isshiki, T. Ushiyama, and T. Kimura, "Demonstration of ErSiO superlattice crystal waveguide toward optical amplifiers and emitters," physica status solidi (a) **205**, 52-55 (2008).

[99] G. Roelkens, J. Van Campenhout, J. Brouckaert, D. Van Thourhout, R. Baets, P. R. Romeo, P. Regreny, A. Kazmierczak, C. Seassal, and X. Letartre, "III-V/Si photonics by die-to-wafer bonding," Materials Today **10**, 36-43 (2007).

[100] H. Rong, R. Jones, A. Liu, O. Cohen, D. Hak, A. Fang, and M. Paniccia, "A continuous-wave Raman silicon laser," Nature **433**, 725-728 (2005).

[101] D. Liang, G. Roelkens, R. Baets, and J. E. Bowers, "Hybrid integrated platforms for silicon photonics," Materials **3**, 1782-1802 (2010).

[102] N. Daldosso, and L. Pavesi, "Nanosilicon photonics," Laser & Photonics Reviews **3**, 508-534 (2009).

[103] A. Polman, B. Min, J. Kalkman, T. Kippenberg, and K. Vahala, "Ultralow-threshold erbium-implanted toroidal microlaser on silicon," Applied Physics Letters **84**, 1037-1039 (2004).

119

[104] X. Duan, Y. Huang, R. Agarwal, and C. M. Lieber, "Single-nanowire electrically driven lasers," Nature **421**, 241-245 (2003).

[105] P. Yang, H. Yan, S. Mao, R. Russo, J. Johnson, R. Saykally, N. Morris, J. Pham, R. He, and H.-J. Choi, "Controlled growth of ZnO nanowires and their optical properties," Advanced Functional Materials **12**, 323 (2002).

[106] A. B. Greytak, C. J. Barrelet, Y. Li, and C. M. Lieber, "Semiconductor nanowire laser and nanowire waveguide electro-optic modulators," Applied Physics Letters **87**, 151103 (2005).

[107] Y. Ma, and L. Tong, "Optically pumped semiconductor nanowire lasers," Frontiers of Optoelectronics **5**, 239-247 (2012).

[108] L. Bastard, S. Blaize, and J.-E. Broquin, "Glass integrated optics ultranarow linewidth distributed feedback laser matrix for dense wavelength division multiplexing applications," Optical engineering **42**, 2800-2804 (2003).

[109] P. Madasamy, G. N. Conti, P. Poyhonen, Y. Hu, M. M. Morrell, D. F. Geraghty, S. Honkanen, and N. Peyghambarian, "Waveguide distributed Bragg reflector laser arrays in erbium doped glass made by dry Ag film ion exchange," Optical Engineering **41**, 1084-1086 (2002).

[110] J. Bradley, R. Stoffer, L. Agazzi, F. Ay, K. Wörhoff, and M. Pollnau, "Integrated Al 2 O 3: Er 3+ ring lasers on silicon with wide wavelength selectivity," Optics letters **35**, 73-75 (2010).

[111] P. B. Deotare, T. S. Mahony, and V. Bulovic, "Ultracompact Low-Threshold Organic Laser," ACS nano **8**, 11080-11085 (2014).

[112] H. Ghafouri-Shiraz, and B. Lo, *Distributed feedback laser diodes: principles and physical modelling* (John Wiley & Sons, Inc., 1997).

[113] M. D. McGehee, M. A. Díaz-García, F. Hide, R. Gupta, E. K. Miller, D. Moses, and A. J. Heeger, "Semiconducting polymer distributed feedback lasers," Applied Physics Letters **72**, 1536-1538 (1998).

[114] J. Kringlebotn, J.-L. Archambault, L. Reekie, and D. Payne, "Er 3+: Yb 3+-codoped fiber distributed-feedback laser," Optics Letters **19**, 2101-2103 (1994).

[115] T. Makino, and J. Glinski, "Transfer matrix analysis of the amplified spontaneous emission of DFB semiconductor laser amplifiers," Quantum Electronics, IEEE Journal of **24**, 1507-1518 (1988).

[116] Y. Akahane, T. Asano, B.-S. Song, and S. Noda, "High-Q photonic nanocavity in a two-dimensional photonic crystal," Nature **425**, 944-947 (2003).

[117] E. Kuramochi, M. Notomi, S. Mitsugi, A. Shinya, T. Tanabe, and T. Watanabe, "Ultrahigh-Q photonic crystal nanocavities realized by the local width modulation of a line defect," Applied physics letters **88**, 041112-041112-041113 (2006).

[118] C. Sauvan, G. Lecamp, P. Lalanne, and J. Hugonin, "Modal-reflectivity enhancement by geometry tuning in Photonic Crystal microcavities," Optics express **13**, 245-255 (2005).

[119] M. W. McCutcheon, and M. Loncar, "Design of an ultrahigh Quality factor silicon nitride photonic crystal nanocavity for coupling to diamond nanocrystals," arXiv preprint arXiv:0809.5066 (2008).

[120] A. R. Md Zain, N. P. Johnson, M. Sorel, and R. M. De La Rue, "Ultra high quality factor one dimensional photonic crystal/photonic wire micro-cavities in silicon-on-insulator (SOI)," Optics express **16**, 12084-12089 (2008).

[121] P. B. Deotare, M. W. McCutcheon, I. W. Frank, M. Khan, and M. Lončar, "High quality factor photonic crystal nanobeam cavities," Applied Physics Letters **94**, 121106 (2009).

[122] Q. Quan, and M. Loncar, "Deterministic design of wavelength scale, ultra-high Q photonic crystal nanobeam cavities," Optics express **19**, 18529-18542 (2011).

[123] B.-S. Song, S. Noda, T. Asano, and Y. Akahane, "Ultra-high-Q photonic double-heterostructure nanocavity," Nature materials **4**, 207-210 (2005).

[124] Y. Akahane, T. Asano, B.-S. Song, and S. Noda, "Fine-tuned high-Q photonic-crystal nanocavity," Optics Express **13**, 1202-1214 (2005).

[125] K. Srinivasan, and O. Painter, "Momentum space design of high-Q photonic crystal optical cavities," Optics Express **10**, 670-684 (2002).

[126] H.-C. Liu, and A. Yariv, "Designing coupled-resonator optical waveguides based on high-Q tapered grating-defect resonators," Optics express **20**, 9249-9263 (2012).

[127] Q. Quan, P. B. Deotare, and M. Loncar, "Photonic crystal nanobeam cavity strongly coupled to the feeding waveguide," Applied Physics Letters **96**, 203102-203102-203103 (2010).

[128] Q. Quan, I. B. Burgess, S. K. Tang, D. L. Floyd, and M. Loncar, "High-Q, low index-contrast polymeric photonic crystal nanobeam cavities," Optics express **19**, 22191-22197 (2011).

[129] G. Hollemann, B. Braun, F. Dorsch, P. Hennig, P. Heist, U. Krause, U. Kutschki, and H. A. Voelckel, "RGB lasers for laser projection displays," in *Electronic Imaging*(International Society for Optics and Photonics, 2000), pp. 140-151.

[130] A. Neumann, J. J. Wierer, W. Davis, Y. Ohno, S. R. Brueck, and J. Y. Tsao, "Four-color laser white illuminant demonstrating high color-rendering quality," Optics express **19**, A982-A990 (2011).

[131] Y. Sun, N. C. Giebink, H. Kanno, B. Ma, M. E. Thompson, and S. R. Forrest, "Management of singlet and triplet excitons for efficient white organic light-emitting devices," Nature **440**, 908-912 (2006).

[132] Y. Fukuda, T. Watanabe, T. Wakimoto, S. Miyaguchi, and M. Tsuchida, "An organic LED display exhibiting pure RGB colors," Synthetic Metals **111**, 1-6 (2000).

[133] P. Claisse, and G. Taylor, "Internal quantum efficiency of laser diodes," Electronics Letters **28**, 1991-1992 (1992).

[134] J. W. Raring, M. C. Schmidt, C. Poblenz, Y.-C. Chang, M. J. Mondry, B. Li, J. Iveland, B. Walters, M. R. Krames, and R. Craig, "High-efficiency blue and true-green-emitting laser diodes based on non-c-plane oriented GaN substrates," Applied physics express **3**, 112101 (2010).

[135] M. Zhou, B. Yan, G. Bao, Y. Zhang, C. Gawith, D. Wang, Y. Qi, and Y. Bi, "52% optical-to-optical conversion efficiency in a compact 1.5 W 532 nm second harmonic generation laser with intracavity periodically-poled MgO: LiNbO3," Laser physics **20**, 1568-1571 (2010).

[136] D. Hargis, and A. Earman, "Lasers replace conventional technology in display designs," Laser focus world **34**, 145-149 (1998).

[137] W. W. Chow, S. W. Koch, and M. Sargent III, *Semiconductor-laser physics* (Springer-Verlag New York, Inc., 1994).

[138] A. Pan, R. Liu, M. Sun, and C.-Z. Ning, "Quaternary alloy semiconductor nanobelts with bandgap spanning the entire visible spectrum," Journal of the American Chemical Society **131**, 9502-9503 (2009).

[139] A. Pan, W. Zhou, E. S. Leong, R. Liu, A. H. Chin, B. Zou, and C. Ning, "Continuous alloy-composition spatial grading and superbroad wavelength-tunable nanowire lasers on a single chip," Nano letters **9**, 784-788 (2009).

[140] Y. Huang, X. Duan, and C. M. Lieber, "Nanowires for integrated multicolor nanophotonics," Small **1**, 142-147 (2005).

[141] Y. Ding, Q. Yang, X. Guo, S. Wang, F. Gu, J. Fu, Q. Wan, J. Cheng, and L. Tong, "Nanowires/microfiber hybrid structure multicolor laser," Optics express **17**, 21813-21818 (2009).

[142] N. A. Naderi, F. Grillot, K. Yang, J. B. Wright, A. Gin, and L. F. Lester, "Two-color multi-section quantum dot distributed feedback laser," Optics express **18**, 27028-27035 (2010).

[143] E. Jang, S. Jun, H. Jang, J. Lim, B. Kim, and Y. Kim, "White‐Light‐Emitting Diodes with Quantum Dot Color Converters for Display Backlights," Advanced Materials **22**, 3076-3080 (2010).

[144] P. O. Anikeeva, J. E. Halpert, M. G. Bawendi, and V. Bulovic, "Quantum dot light-emitting devices with electroluminescence tunable over the entire visible spectrum," Nano letters **9**, 2532-2536 (2009).

[145] S. K. Tang, Z. Li, A. R. Abate, J. J. Agresti, D. A. Weitz, D. Psaltis, and G. M. Whitesides, "A multi-color fast-switching microfluidic droplet dye laser," Lab on a Chip **9**, 2767-2771 (2009).

[146] G. Aubry, Q. Kou, J. Soto-Velasco, C. Wang, S. Meance, J. He, and A. Haghiri-Gosnet, "A multicolor microfluidic droplet dye laser with single mode emission," Applied Physics Letters **98**, 111111 (2011).

[147] J. Alexander, "A switchable digital microfluidic droplet dye-laser," Lab on a Chip **11**, 3716-3719 (2011).

[148] Z. Yang, J. Xu, P. Wang, X. Zhuang, A. Pan, and L. Tong, "On-nanowire spatial band gap design for white light emission," Nano letters **11**, 5085-5089 (2011).

[149] F. Fan, Z. Liu, L. Yin, P. Nichols, H. Ning, S. Turkdogan, and C. Ning, "Simultaneous two-color lasing in a single CdSSe heterostructure nanosheet," Semiconductor Science and Technology **28**, 065005 (2013).

[150] A. Pan, R. Liu, M. Sun, and C.-Z. Ning, "Spatial composition grading of quaternary ZnCdSSe alloy nanowires with tunable light emission between 350 and 710 nm on a single substrate," ACS nano **4**, 671-680 (2010).

[151] R. K. Willardson, and A. C. Beer, *Semiconductors & semimetals* (Academic Press, 1977).

[152] F. Gu, Z. Yang, H. Yu, J. Xu, P. Wang, L. Tong, and A. Pan, "Spatial bandgap engineering along single alloy nanowires," Journal of the American Chemical Society **133**, 2037-2039 (2011).

[153] F. Logue, P. Rees, J. Heffernan, C. Jordan, J. Donegan, J. Hegarty, F. Hiei, S. Taniguchi, T. Hino, and K. Nakano, "Optical gain in (Zn, Cd) Se–Zn (S, Se) quantum wells," JOSA B **15**, 1295-1304 (1998).

[154] A. Girndt, F. Jahnke, A. Knorr, S. Koch, and W. Chow, "Multi‑Band Bloch Equations and Gain Spectra of Highly Excited II‑VI Semiconductor Quantum Wells," physica status solidi (b) **202**, 725-739 (1997).

[155] Y. Yamada, Y. Masumoto, and T. Taguchi, "Formation of optical gain due to exciton localization in Cd x Zn 1− x S-ZnS strained-layer quantum wells," Physica B: Condensed Matter **191**, 83-89 (1993).

[156] C. Klingshirn, H. Kalt, M. Umlauff, W. Petri, F. Majumder, S. Bogdanov, W. Langbein, M. Grün, M. Hetterich, and K. Geyzers, "Stimulated emission of II–VI epitaxial layers," Journal of crystal growth **138**, 786-790 (1994).

[157] P. Motisuke, C. Argüello, and R. Luzzi, "Effect of excited electron states lifetime on gain spectra of EHL in CdS," Solid State Communications **23**, 617-620 (1977).

[158] P. J. Pauzauskie, D. J. Sirbuly, and P. Yang, "Semiconductor nanowire ring resonator laser," Physical review letters **96**, 143903 (2006).

[159] K. Huang, S. Yang, and L. Tong, "Modeling of evanescent coupling between two parallel optical nanowires," Applied optics **46**, 1429-1434 (2007).

[160] R.-M. Ma, X.-L. Wei, L. Dai, S.-F. Liu, T. Chen, S. Yue, Z. Li, Q. Chen, and G. Qin, "Light Coupling and Modulation in Coupled Nanowire Ring− Fabry-Pérot Cavity," Nano letters **9**, 2697-2703 (2009).

[161] B. Jensen, and A. Torabi, "Refractive index of hexagonal II–VI compounds CdSe, CdS, and CdSe x S 1− x," JOSA B **3**, 857-863 (1986).

[162] L. W. Casperson, "Threshold characteristics of multimode laser oscillators," Journal of Applied Physics **46**, 5194-5201 (1975).

[163] F. Brunner, E. Innerhofer, S. V. Marchese, T. Südmeyer, R. Paschotta, T. Usami, H. Ito, S. Kurimura, K. Kitamura, and G. Arisholm, "Powerful red-green-blue laser source pumped with a mode-locked thin disk laser," Optics letters **29**, 1921-1923 (2004).

APPENDIX A

FIBER-NANOWIRE COUPLING SYSTEM

For signal enhancement measurement in Chapter 4.2 and transmission spectroscopy in Chapter 5.2, the coupling of laser signal into or out of the nanowire waveguide is necessary. One common tool to couple the laser light into optical waveguides is the lensed fibers. The diameter of the tapered fiber uniformly tapers from 125 µm to several microns at the tip. Most commercial lensed fibers contain a manufactured tip with a sharp tapering from 125 µm diameter to several microns. The taper shape is well designed as a lens, so the output light from the lensed fiber can be focused to a spot of 1 − 2 µm. The working distance, which is the distance between the waist of the focusing spot and the tip of the fiber, is typically 10 − 20 µm. Thus, it is possible to couple the signal to the waveguides with submicron cross-sections, as shown in Figure A.1(a). However, it is difficult to do the coupling from the lensed fiber to a nanowire on substrate, since in most of the cases the end facets of the nanowire cannot stick out from the substrate. Due to the large tip size and large taper angle of the commercial lensed fiber, there has to be a long distance between the fiber and the nanowire, resulting the extremely low coupling efficiency, as shown in Figure A.1(b).
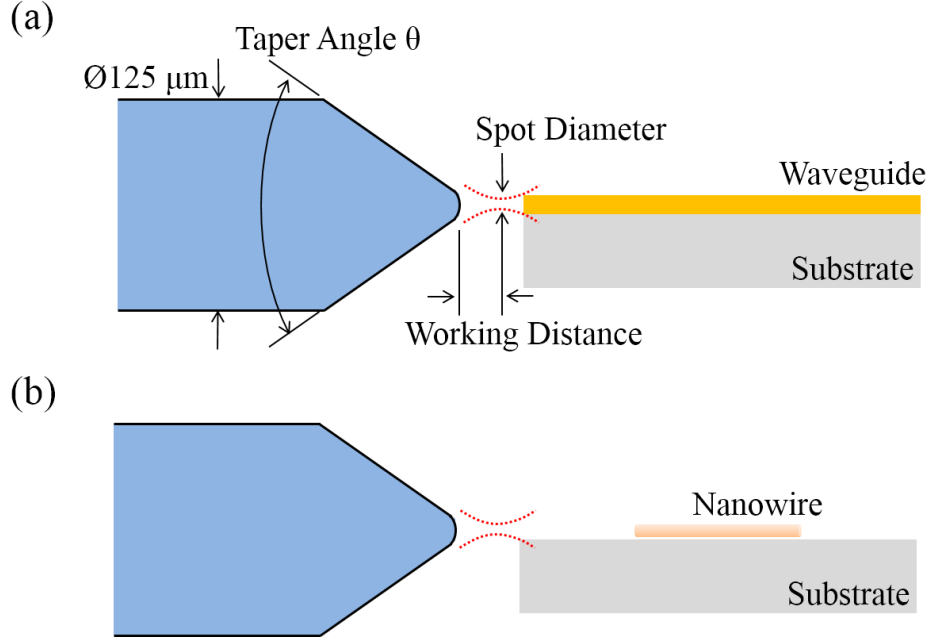
Figure A.1 (a) Coupling between the commercial lensed fiber and optical waveguide. The diameter of the lensed fiber is 125 μm. The included angle θ of the fiber is around 90°. The spot diameter is 2 μm and the working distance is 10 – 20 μm. (b) An example of the coupling between commercial lensed fiber and nanowire. Due to the large taper size, the distance between the fiber tip and the nanowire has to be much large than the working distance.

In order to enable the high efficient coupling between fiber and nanowire, we manufactured the tapered fibers with much smaller tip, as illustrated in Figure A.2. The tapered fiber is fabricated by heating-and-pulling method. The center region of a striped SMF-28 fiber is heated by a flame to the melting point. By pulling the melt fiber at a speed around 1 mm/s, the fiber breaks in the middle and two tapered fibers with long tapered region are formed. The tapered region is over 1 mm with taper rate around 100 μm/mm. The tip size is smaller than 2 μm and the included angle of the taper is around 6°, as shown in Figure A.2(b). It is possible to place such tapered fiber on top of the substrate with a very small angle. Therefore, the fiber-nanowire coupling can be achieved by directly contacting the fiber tip with the nanowire, as the illustration in Figure 4.3(b).
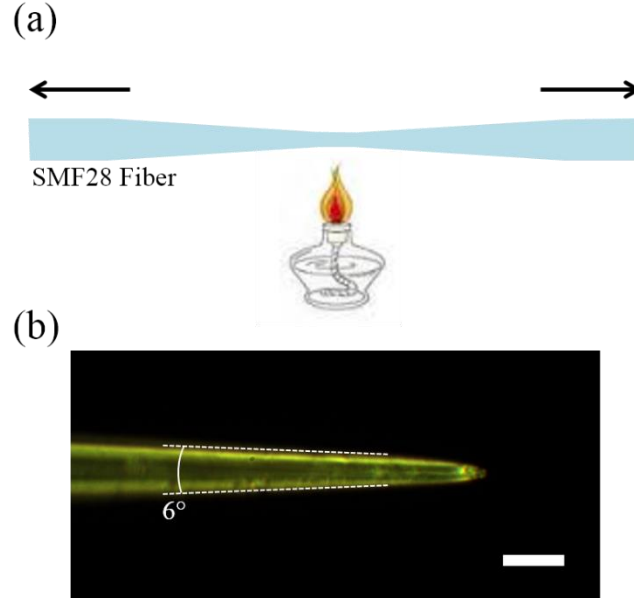
Figure A.2 (a) Heating-and-pulling fabrication of the tapered fiber. (b) Image of the tapered fiber. The included angle of the taper is 6°. The tip size is smaller than 2 μm. Scale bar is 20 μm.

A photo image of the coupling system is shown in Figure A.3(a). For the alignment, the tapered fibers are mounted on the 3D stages (XYZ) with an angle $10° - 20°$ to the horizontal and the nanowire sample is mounted on a 4D stage (XYZ & φ). All the alignment is performed under a microscope (Mitutoyo, FS70) equipped with long working distance objectives. Figure A.3(b) shows an example of the fiber-nanowire coupling. The tip of the tapered fiber directly contacts with the end facet of the nanowire. Because the size of the tapered fiber is $1 - 2$ μm, matching with the nanowire diameter, the high coupling efficiency is possible. The coupling loss between tapered fiber and nanowire is around 5 dB at 1.6 μm.
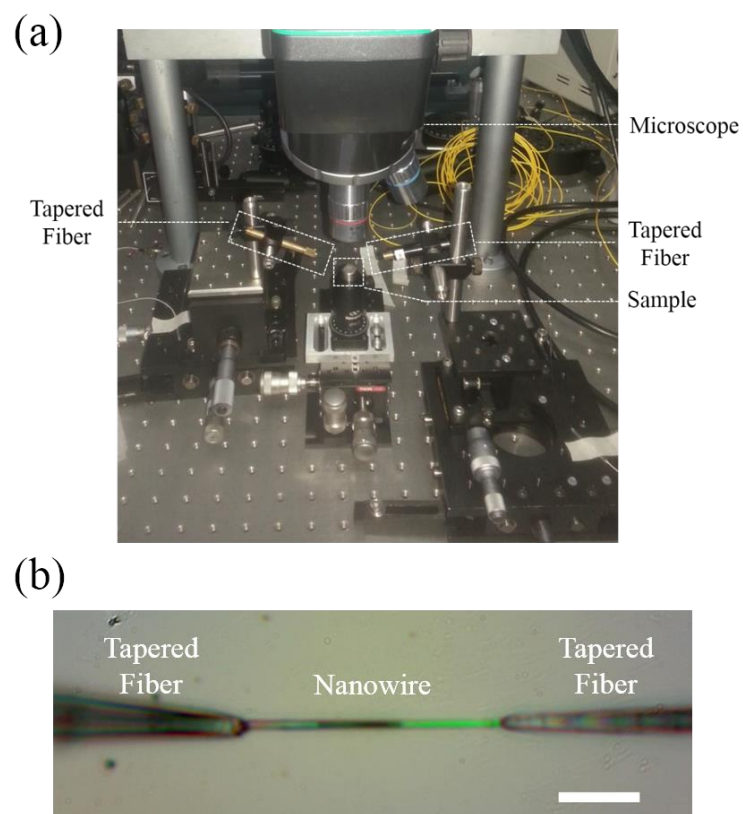
Figure A.3 (a) Setup of Fiber-nanowire coupling system. (b) Top view image of the microscope image of the fiber-nanowire-fiber coupling.

APPENDIX B

NANOWIRE MANIPULATION SETUP

In Chapter 7, we studied the simultaneous two-color lasing in looped nanowire structure. The nanowire manipulation, such as transferring the nanowire between the substrates and looping the nanowire to a circle, is performed using a tapered fiber. The tapered fiber is fabricated with the same technique shown in Figure A.2. The best tip size of the tapered fiber is around 1 μm. If the tip is too big, there is not enough contact between the tip and the nanowire when they are in touched on the substrate. If the tip is too small, the nanowire is easy to be broken by the shape tip. The manipulation setup is illustrated in Figure A.4(a). The tapered fiber is mounted on a 3D stage (XYZ) with an angle of 30° to the horizontal. The nanowire sample is mounted on a 4D stage (XYZ & θ). The manipulation is under a dark-filed/bright-field microscope (Olympus, BX51) equipped with long working distance objectives.

The nanowire manipulation is shown in Figure A.4(b). The tapered fiber is lowered to the substrate and directly contacts with the nanowire. The tapered fiber is vertical to the axial direction of the nanowire at the contacting region. By pushing the tapered fiber, the nanowire can be curved and looped at the desired shape.

Due to the charging in the tapered fiber, when the tapered fiber contacts with a long section of the nanowire in parallel, there is a chance to attach the nanowire to the micro fiber by the electric force. Then, the nanowire can be picked up by lifting the tapered fiber and transferred to the other substrate, as illustrated in Figure A.4(c).

131

(a)

Microscope

Sample
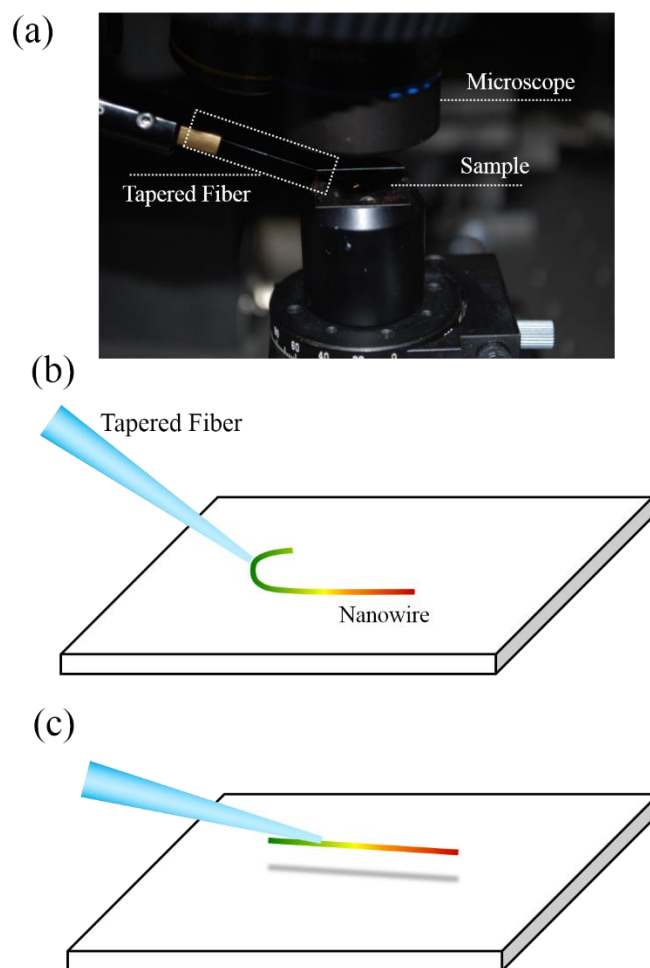
Tapered Fiber

(b)

Tapered Fiber

Nanowire

(c)

Figure A.4 (a) Nanowire manipulation setup. (b) Approach to curve and loop the nanowire by tapered fiber. (c) Approach to pick up the nanowire by tapered fiber.

APPENDIX C

PHOTOLUMINESCENCE AND LASING TESTING SETUP

In Chapter 7.1 and 7.2, a micro-PL setup as shown in Figure A.5 was used to excite and collect the single-color and two-color lasing spectra from the straight and looped alloy nanowires respectively. A Q-switched 355 nm YAG laser (Spectra-Physics, Quanta-ray) was used as the pumping source. The pulse width of the pumping laser is 9 ns and the repetition rate is 10 Hz. The pumping laser was focused by a lens and incident to the nanowire sample with an angle of 60° to the normal direction. The pumping spot can be tuned by defocusing the lens. In the experiment in Figure 7.1 and 7.2, the spot size was 200 μm for covering the entire alloy nanowire. The lasing emission was collected by a long working distance objective and split to two beams by a beam splitter. One beam was collected by the spectrometer (Jobin Yvon, Triax 320) equipped with a silicon CCD detector for the spectroscopy and the other beam was guided to the camera. Thus, the spectra and lasing images can be collected simultaneously.
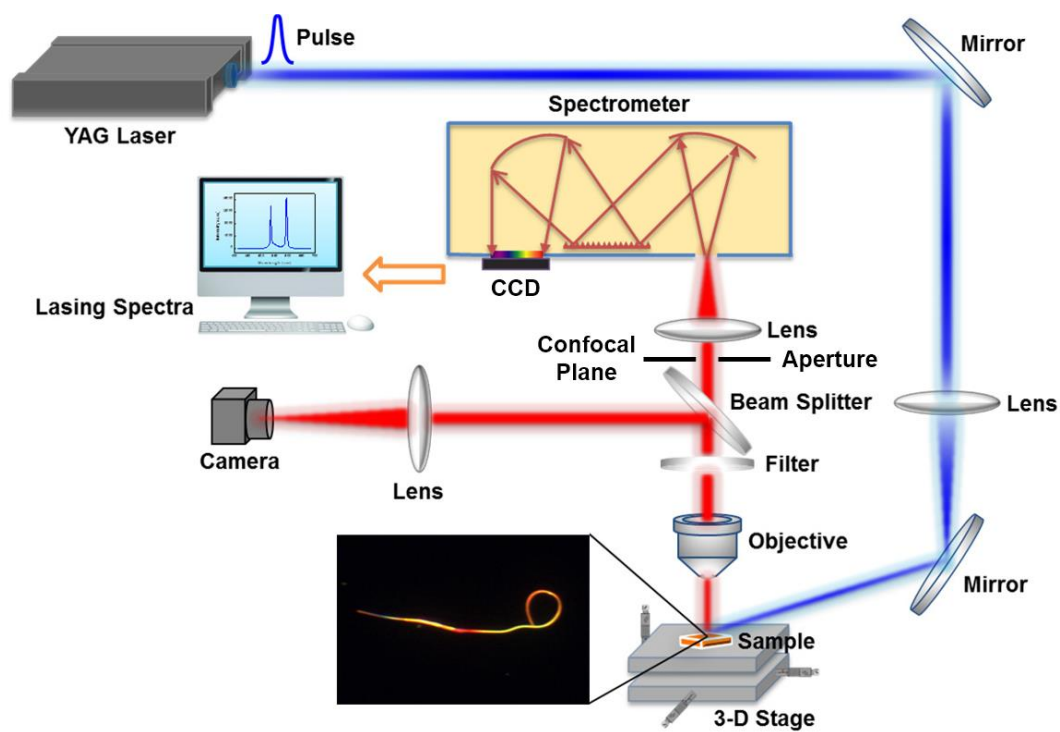
Figure A.5 Micro-PL setup with confocal collection.

An aperture was inserted at the confocal plane of the objective for the localized collection. For the normal spectroscopy in Figure 7.1 and 7.2, the aperture was fully opened for the large area collection. The effective collection spot is around 100 μm in diameter. For the localized collection in Figure 7.5, the aperture was closed to the size of 0.3 mm. The effective collection spot is around 5 μm.

APPENDIX D

MULTI-BEAM EXCITATION SETUP

In order to tune the output lasing color of the looped alloy nanowire, the looped section and the straight section should be excited with two individual beams. We developed a two-beam excitation setup for splitting the excitation laser to two beams and controlling the pumping power and excitation position of the two beams individually, as illustrated in Figure A.6. The pumping laser is split to two beams by a beam splitter. The two beams are converged by another beam splitter and be focused on the nanowire sample by the focusing lens. The excitation positions of the two beams can be controlled by the two mirrors at the split beam routes respectively. Two set of half-wave plate & polarizer systems are inserted in the two split beam routes for tuning the pumping power of two excitation beams respectively. Therefore, both the pumping position and pumping power of the two beams can be individually and precisely controlled. The excitation spot size is controlled by the focusing lens. The aspect ratio of the elliptical pumping beams can be adjusted by the distance between the two cylindrical lenses. All excitation properties can be adjusted in this two-beam excitation setup. Therefore, the output color of the looped alloy nanowire can be continuously tuned. The setup can also be extended to more excitation beams by splitting the beam with more beam splitters.
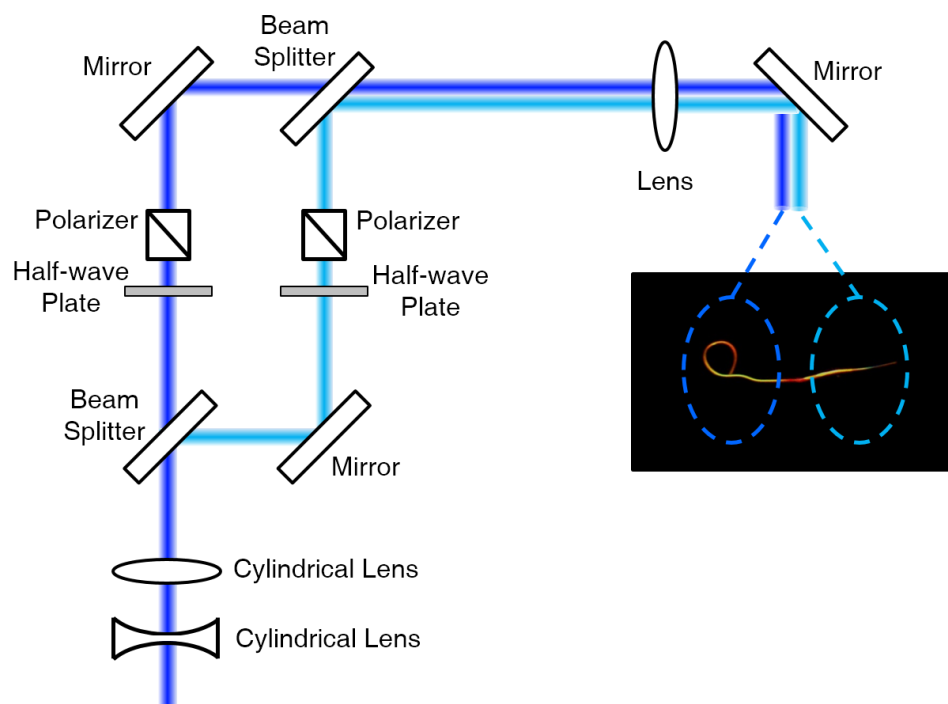
Figure A.6 Illustration of multi-beam excitation setup. The excitation beam is split by a beam splitter and converged by another beam splitter. After the focusing lens, the two beams can be focused to two excitation spots, shown as the dark blue and light blue dashed circles respectively.